

Searching for SUSY in events with Jets and Missing Transverse Energy using α_T with the CMS Detector at the LHC

Zoe Hatherell

A thesis submitted in fulfilment of the requirements
for the degree of Doctor of Philosophy
to Imperial College London
December 2011

Contents

Acknowledgements	2
Contents	2
1 Introduction	5
2 Theoretical Overview	6
2.1 The Standard Model	6
2.1.1 Gauge Theory of Interactions	8
2.1.2 EWSB and the Higgs Mechanism	16
2.2 Motivation for Physics Beyond the Standard Model	17
2.2.1 The Hierarchy Problem	18
2.2.2 Cold Dark Matter	19
2.2.3 Unification of Coupling Constants	20
2.3 Supersymmetry	20
2.3.1 R-Parity	22
2.3.2 MSSM	23
2.3.3 Supersymmetry Breaking	24
2.3.4 Minimal Supergravity and the Constrained MSSM	25
2.3.5 Production Mechanisms in pp collisions	27
3 The Compact Muon Solenoid Experiment at the LHC	30
3.1 The Large Hadron Collider	30
3.2 The Compact Muon Solenoid	33
3.2.1 Coordinate System	36
3.2.2 Superconducting Magnet	36
3.2.3 Tracker	37
3.2.4 ECAL	38
3.2.5 HCAL	40
3.2.6 Muon System	42
3.2.7 Trigger	44

4 Event Reconstruction	47
4.1 Beamspot	48
4.2 Tracks	48
4.3 Vertex	50
4.4 Jets	50
4.4.1 The anti- k_T jet clustering method	51
4.4.2 Jet Energy Scale Corrections	53
4.5 Missing Energy	55
4.5.1 \cancel{E}_T Corrections	56
4.5.2 Using Jets for Missing Energy - \cancel{H}_T	57
4.6 Muon	58
4.7 Photons	59
4.8 Electrons	60
5 Searching for SUSY with α_T	62
5.1 Inclusive SUSY Search	62
5.2 α_T in a di-jet system	64
5.3 α_T in a n-jet system	65
5.4 Defining the ratio R_{α_T}	67
5.5 Extending α_T for single-lepton searches	67
5.6 Reliance of α_T on jet object definition	68
6 Searching for Supersymmetry with α_T in all-hadronic events	70
6.1 Samples	71
6.1.1 Monte Carlo Simulation	71
6.1.2 Data Sample	72
6.2 Analysis Framework	73
6.3 Trigger	73
6.4 Object Definitions	76
6.4.1 Good Event Definition	76
6.4.2 Jets	76
6.4.3 H_T and \cancel{H}_T	76
6.4.4 Muons	77
6.4.5 Electrons	77
6.4.6 Photons	78
6.5 Pre-Selection	79
6.6 Final Signal Selection	80
6.7 An H_T Shape Analysis	80
6.8 Hadronic Signal Region Results	81
6.8.1 Data to Monte-Carlo Comparisons	81
6.8.2 R_{α_T} on H_T	83
6.8.3 Composition of Selected $t\bar{t}$ + jets and W + jets Background Events	86

6.9	Estimation of $t\bar{t}$ and $W + \text{Jets}$ Backgrounds with a high p_T control sample using $W \rightarrow \mu\nu$ events	87
6.9.1	μ Control Sample Selection	87
6.9.2	Prediction Calculation	89
6.9.3	μ Control Sample Systematic Uncertainty	93
6.9.4	Signal Contamination in μ Control Sample	96
6.10	Estimation of $Z \rightarrow \nu\bar{\nu} + \text{jets}$ background using photon + jets events	97
6.10.1	Z Background Prediction Calculation	99
6.10.2	γ Control Sample Systematic Uncertainty	99
6.10.3	Cross-Prediction between Control Samples	100
6.11	Signal Region Systematic Uncertainties	101
6.12	Statistical Interpretation	103
6.12.1	Hadronic Signal Selection Likelihood	103
6.12.2	Expression of b^i using R_{α_T} evolution in H_T	103
6.12.3	Electroweak Control Sample Likelihoods	104
6.12.4	Presence of Signal	105
6.12.5	Total Likelihood	106
6.13	Testing the SM-only hypothesis	106
6.14	Excluding Signal Models	109
6.14.1	Constructing a Test Statistic	109
6.14.2	The CL_S Method	110
6.14.3	Setting an Exclusion Limit in the CMSSM Plane	111
7	Conclusions	113
A		114
Bibliography		116

Chapter 1

Introduction

Describe storyline of Thesis.

Chapter 2

Theoretical Overview

At the heart of particle physics is a quest to discover the fundamental building blocks of the universe, and how they interact with one another. Experimentally this is done by delving into smaller and smaller distance scales using particle colliders with greater energies and analysing the interactions that result. This relationship between small distances and high energies is at the heart of the field, as each increase of energy scale allows the investigation of the structure of matter at a smaller length scale. Throughout the history knowledge has been advanced through a combination of theoretical postulation using mathematical tools, and experimental searches. Particle physicists seek together to build a full description of the dynamics of the fundamental particles, and while they have discovered much, the picture is not complete yet. The description of current understanding is collectively known as the Standard Model (SM), and is a rigorously tested and widely accepted theory. However, whilst there are no disagreements, there are some gaps which hint at physics beyond, fuelling a new generation of experimentalists seeking answers to what lies at the next energy frontier.

2.1 The Standard Model

The Standard Model (SM) is the name given to the theories that successfully describes the known elementary particles and their fundamental interactions with respect to the strong, weak and electromagnetic forces.

Within it there two main types of fundamental particle, which in order to

distinguish we must first address the concept of spin.

Spin

Spin is the name given to a property of elementary particles, corresponding to a type of angular momentum, although this differs from classical angular momentum. This is an intrinsic property and thus has a specific value for each particle type. It can be thought for massive particles as the angular momentum about the central point, but it is known that massless particles such as the photon carry spin also, so this analogy breaks down. The values of the spin quantum number s which describe the magnitude can take any half integer value $s = 0, \frac{1}{2}, 1, \frac{3}{2}$, etc. In addition to magnitude we describe a particle as having spin *up* (positive) when the spin is in the direction of the z-axis, and spin *down* (negative) if the spin is against the direction of the z-axis.

The definition of spin gives a second key property, known as chirality. When the spin direction is in the direction of momentum of the particle, it is described as left-handed, and when it is against as right-handed. The chirality of a particle is integral to the way it behaves, as we will see in the treatment of the weak force. In the massless limit the chirality is analogous to the concept of helicity, although it is worth noting that for a massive particle helicity depends on the reference frame of observation, whereas chirality describes an inherent property that determines how the particle will behave.

All fundamental particles are divided into the spin-1/2 *fermions* which are the building blocks for matter, and the force-mediating *bosons* which must carry integer spin, usually spin-1. One consequence of this is the wave function of a bosonic system is symmetric under the swap of two of its particles, whilst that of a fermionic system is anti-symmetric. A consequence of this, as can be seen in Equation 2.1 is the well-known Pauli Exclusion Principle, that two fermions may not exist in the same state.

$$\psi_f(x_a, x_b) = -\psi_f(x_b, x_a), \therefore \psi_f(x_a, x_a) = 0 \quad (2.1)$$

The fermions which make up all visible matter can be described in three families, or “generations”, each of which is further divided into two sets, the

quarks and the leptons. There are three charged leptons with one unit of electric charge, electron (e), muon (μ) and tau (τ), and three associated massless or incredibly light neutral leptons called neutrinos, named after the charged lepton in their generation, ν_e, ν_μ, ν_τ respectively. This indicates the introduction of a new concept, “flavour”, of which there are three, one for each generation.

The quarks show an analogous structure, divided into two types in three generations. The up (u), charm (c) and top (t) quarks carry $+2/3e$ while the down (d), strange (s) and bottom (b) quarks carry $-1/3e$ and each of the 6 quarks corresponds to its own flavour.

The generation structure is shown in Equation 2.2. The particles in the second and third generation exhibit the same properties as the corresponding first generation particles, except for the mass which increases with ascending generations. The first generation is therefore stable and all ordinary matter is constructed from it, whilst the second and third once produced are liable to decay into particles of the first generation. In addition to each particle detailed here there exists a corresponding antiparticle due to a symmetry in charge and quantum numbers. Each fermion can be described as a spinor field ψ which describes a pair of complex fields, the left-handed (ψ_L) and right-handed (ψ_R) representations.

$$\begin{bmatrix} \nu_e & u \\ e & d \end{bmatrix}, \begin{bmatrix} \nu_\mu & c \\ \mu & s \end{bmatrix}, \begin{bmatrix} \nu_\tau & t \\ \tau & b \end{bmatrix} \quad (2.2)$$

The particles which mediate the forces are bosons, the photon γ for the electromagnetic force, the 8 gluons g_i for the strong force and the W^\pm and Z bosons that carry the weak (nuclear) force, all of which are spin-1 particles. The photon and gluons are massless, whilst the weak vector bosons have non-negligible mass. The final particle of the SM is the Higgs Boson of spin-0, as yet undiscovered in experiment but expected from the theory, as we will see later.

2.1.1 Gauge Theory of Interactions

The theories that make up the SM are formulated mathematically using Quantum Field Theory (QFT), in which particles are thought of as excitations of fields, and the dynamics of a given system are summarised in what is known as Lagrangian

formalism. In this the Lagrangian L is the difference between kinetic energy T and potential energy V , $L = T - V$. In QFT it is usual to describe a system by the Lagrangian Field Density \mathcal{L} , where L is obtained from \mathcal{L} by integrating over the spatial component d^3x .

In order to reflect the symmetries observed in nature, the dynamics of a system and therefore the Lagrangian Density \mathcal{L} , must be invariant under some set of transformations,

$$\psi \rightarrow e^{-i\alpha} \psi \quad (2.3)$$

where ψ represents a spinor field. If α has no reliance on the space-time coordinate, we say this is a global symmetry. In order to describe the fundamental interactions it is necessary to use the special case where the transformations are *local*, where α has a dependence on the space-time coordinate. The Standard Model describes such symmetries, a case we call gauge invariance, and is a special case of field theory known as Gauge Theory, where the transformations have the form,

$$\psi(x) \rightarrow e^{-i\alpha(x)} \psi(x) \quad (2.4)$$

It is clear that \mathcal{L} will not remain unchanged by such a transformation, as the dependence of α on x means that the coordinate derivative ∂_μ introduces extra terms. In order to leave the Lagrangian unchanged a vector field is introduced A_μ that transforms under another local transformation to keep \mathcal{L} constant:

$$A_\mu \rightarrow A_\mu + \frac{1}{g} \partial_\mu \alpha(x) \quad (2.5)$$

Thus we can rewrite \mathcal{L} introducing the *covariant derivative*,

$$\mathcal{D}_\mu = \partial_\mu - igA_\mu. \quad (2.6)$$

This interaction between the spinor field and the vector field through this covariant derivative indicate the interactions of matter particles though the force carrying bosons. From Noether's Theorem, it is known that as a consequence of a symmetry in a dynamical system there is an associated physically conserved quantity[1]. Just as the classical conservation laws pertaining to momentum

and energy are given by the space-time translational symmetries in Classical Mechanics, for the electromagnetic force symmetries in Quantum Mechanics the electric charge is conserved. Analogously, there ought to be conserved “charges” for the strong and weak forces also, corresponding to quantum numbers from their Lagrangian Densities.

The set of possible transformations is described in the language of Group Theory, and thus we describe the SM as a non-Abelian Yang-Mills type gauge field theory based on the symmetry group $SU(3)_C \times SU(2)_L \times U(1)_Y$. As this group is a product the three individual elements are free to each have its own coupling constant, and these may differ. The strong interactions described by Quantum Chromodynamics (QCD) are represented by $SU(3)_C$, labelled C to indicate the conserved charge “Colour”. The electromagnetic and weak interactions are represented together due to Electroweak Unification, which we shall explore in detail later, by the group $SU(2)_L \times U(1)_Y$ where L stands for left, indicating the parity violation of the weak interaction and Y the conserved charge “hypercharge”. As of yet, the fourth fundamental force Gravity is not included in the Standard Model, but this is seen as of little consequence as gravitational forces have comparatively little effect on fundamental particles at current experimental energy scales.

Quantum ElectroDynamics

The fundamental electromagnetic force is studied in quantum field theory as Quantum Electrodynamics (QED), the oldest and simplest of the theories brought together to form the SM. The symmetry group of QED is $U(1)$ and this gives an associated conserved quantity, the electric charge Q. The electromagnetic force is carried by the massless boson, the photon, and affects only the charged fermions. The symmetry allows no self interaction of the photon. The fermion field ψ_q with charge q and mass m_q with symmetries under the group of transformations $e^{-i\alpha(\mathbf{x})}$ gives rise to the Lagrangian in Equation 2.7.

$$\mathcal{L}_{QED} = \bar{\psi}_q(\mathbf{x})(i\gamma^\mu \mathcal{D}_{QED} - m_q)\psi_q(\mathbf{x}) - \frac{1}{4}F_{\mu\nu}F^{\mu\nu} \quad (2.7)$$

The kinetic term depends on the Field Strength Tensor F,

$$F_{\mu\nu}(\mathbf{x}) = \partial_\mu A_\nu(\mathbf{x}) - \partial_\nu A_\mu(\mathbf{x}) \quad (2.8)$$

which incorporates the introduction of a gauge field A_μ which is transformed along with ψ in the following way:

$$A_\mu(\mathbf{x}) \rightarrow A_\mu(\mathbf{x}) + \partial_\mu \alpha(\mathbf{x}) \quad (2.9)$$

The covariant derivative, $\not{D}_{QED,\mu}$ is defined as in Equation 2.10 so as to maintain an invariance to local U(1) charge symmetry.

$$\mathcal{D}_{QED} = \partial_\mu + iqA_\mu \quad (2.10)$$

where q is described as the generator of the symmetry group and is analogous to electric charge. The strength of coupling of each force is described by the coupling constant, in this case governed by the constant e, the charge of an electron: $\alpha = \frac{e^2}{4\pi}$. This is more commonly known as the *fine structure constant* and has been measured experimentally to a high degree of accuracy to have a value $\alpha = 1/137$ [2]. The coupling constants of the standard model are not fixed at all energy scales, rather they vary, and this is called the “running” of the coupling constants. This will become important when incorporating the other forces.

QCD

Quantum Chromodynamics (QCD) is the relevant quantum field theory that describes the dynamics of the strong force. The strong force of symmetry group $SU(3)_C$ has 8 massless gauge bosons known as the gluons, and a conserved quantity called colour charge, which has three types called q_i , where $i = 1, 2, 3$. The name “colour” is not meant to imply a connection to visual colour, merely an analogy between the three types and the primary colours red, blue and green. Only particles which carry colour charge are affected - the quarks have colour, while leptons do not. Unlike the photon in electromagnetism, the gluons that mediate the force carry the charge also, leading to the self-interactions that govern the behaviour of QCD.

A quark carries one “colour” q_i , taking one of the three possible values, and an analogous antiquark carries one “anti-colour”. On the other hand, gluons carry both a colour and an anti-colour. Separation of two charges gives rise to a potential energy, which increases linearly as the charges are moved further apart. As a consequence, it would take an infinite amount of energy to separate

two quarks, and thus they are not found free in nature, but only bound within colourless composite particles, an effect we call *confinement*. There are two allowed stable bound states, the three-quark hadrons such as the proton $p \sim uud$ and the neutron $n \sim udd$, and quark-anti-quark mesons such as the pions π^0, π^\pm . This explains why colour charge is not observed in nature, as beyond a fundamental level it is required to be zero.

The local $SU(3)_C$ invariance of QCD is defined by the transformations in Equation 2.11, where g_s is the strong coupling constant, λ_α are the Gell Mann matrices, and the θ^α describe the transformation angles.

$$q(\mathbf{x}) \rightarrow e^{i\frac{g_s}{2}\theta^\alpha(\mathbf{x})\lambda_\alpha} q(\mathbf{x}) \quad \text{with } \alpha = 1, \dots, 8 \quad (2.11)$$

As with QED, the gauge fields of the gluons A_μ^α also transform as in Equation 2.12 to maintain local invariance.

$$A_\mu^\alpha(\mathbf{x}) \rightarrow A_\mu^\alpha(\mathbf{x}) = \frac{1}{g_s} \partial_\mu \theta^\alpha(\mathbf{x}) + f_{\alpha\beta\gamma} \theta^\beta(\mathbf{x}) A_\mu^\gamma(\mathbf{x}) \quad (2.12)$$

The Lagrangian for a quark carrying colour α is then described in Equation 2.13

$$\mathcal{L}_{QCD} = \sum_q \bar{q}(i\gamma^\mu \not{D}_{QCD} - m_q)q - \frac{1}{4}G_{\mu\nu}^\alpha G_\alpha^{\mu\nu} \quad (2.13)$$

where the covariant derivative in this case is

$$\not{D}_{QCD} = \partial_\mu - i\frac{g_s}{2}\lambda_\alpha A^\alpha \mu(stc) \quad (2.14)$$

The gluon field tensor $G_{\mu\nu}^\alpha$, analogous to the photon field tensor we had seen in QED is defined in Equation 2.15. Unlike that of the photon, it can be seen that in the kinetic term of \mathcal{L} this gives rise to three and four gluon terms thus describing the self-interaction of the gluons.

$$G_{\mu\nu}^\alpha(\mathbf{x}) = \partial_\mu A_\nu^\alpha(\mathbf{x}) - \partial_\nu A_\mu^\alpha(\mathbf{x}) + g_s f_{\alpha\beta\gamma} A_\mu^\beta(\mathbf{x}) A_\nu^\gamma(\mathbf{x}) \quad (2.15)$$

To describe the behaviour of the strength with decreasing distance, we define an analogous coupling constant for the strong force to that in QED, which we call $\alpha_S = g_s^2/4\pi$. Whilst its QED equivalent runs weaker as the distance

between charges increases, as we have discussed the strong force has the opposite relationship, reflected in the running of the coupling constants with increasing energy scale, which when extrapolated could highlight an energy scale where the two are equal. When we discuss quarks in particle physics although they are free, this is as a result of the “asymptotic freedom” where when viewed at very large energies the distances are infinitely small, and the quarks behave freely.

The Parton Model

In order to understand the physics at hadron-colliders, Feynman introduced the Parton Model, a description of the way the partons (quarks and gluons) inside a hadron behave. The behaviour depends on the energy at which the collision occurs. Each of the quarks in a hadron is joined to the other two by continually exchanging gluons and changing colour in such a way that the bound state remains colour neutral. However, as the distance between a pair of quarks is extended the colour field is put under stress until the gluon splits in two, and in between them is a quark-anti-quark pair is created. The three quarks which define the hadron are known as the *valence quarks* and those that appear in these pairs are known as the sea quarks. Gluons can be created too through the annihilation of such a pair of sea quarks, and these processes go on continually within hadrons.

When colliding at low energies, the system behaves as three separate valence quarks with a certain fraction of momentum each, but at higher energies the sea quarks must be taken into account also, as they can possess a significant fraction of energy. Thus physics at hadron colliders is more difficult than lepton colliders, as it is not trivial to understand the two particles that interact, or the energy that they collide at. Thus it is necessary to know the probability that a given parton has a certain fraction of the energy pf the hadron, described by a Parton Distribution Function (PDF). Calculating PDFs for high energy hadron collisions cannot be calculated theoretically, as inclusion of all potential combinations of sea quarks is not possible due to the non-perturbative nature of QCD caused by the large coupling constant α_S . Thus these are measured experimentally by collaborations such as CTEQ.

The Weak Force and Electroweak Unification

The weak interaction, responsible for radioactive decay, makes up the final piece of the puzzle. So named because of its comparatively low strength compared to the electromagnetic and strong forces, it was theorised as being mediated by massive force bosons W^\pm and Z long before they were discovered experimentally. A lagrangian theory for the weak force must take into account the characteristics of weak interactions. The group symmetry is $SU(2)$ giving rise to a conserved quantity known as weak isospin, I which has a component I_3 that points in the direction of the z axis. The left-handed fermions form isospin doublets with $I_3 = \pm 1/2$ whilst the right handed neutrinos are isospin singlets where $I_3 = 0$.

There are two types of current observed in interactions, the charged current and the neutral current[3]. The charged current, associated with the W Bosons, involves only left handed fermions and right handed anti-fermions, and couples to each fermionic doublet (except that of the top and bottom quark, as $m_t > m_W$), where the two elements differ by one unit of charge. It is capable of changing the flavour of an interaction. The weak eigenstates of the down-type quarks are mixtures of the mass eigenstates, called d', s', and b', the mixing of which is governed by a 3x3 matrix to characterise the flavour changing element. In addition there are neutral current interactions associated with the Z boson, which is flavour conserving, and couples to a fermion anti-fermion pair. In the way the neutral current interactions of the weak free closely resemble that of the photon, affected only by its preference for left handed fermions, whilst QED is chirality blind.

Building an individual Lagrangian to describe the picture of weak interactions was not as simple as in the strong and electromagnetic sectors, with each proposed model suffering problems, as described in detail in Ref. [4]. Finally it was realised that despite their apparent differences the weak and electromagnetic forces were low-energy manifestations of the same force, and a composite theory was proposed [5]. This is called Electroweak Unification, and for this the Nobel Prize was awarded to Glashow, Salam and Weinberg in 1979 [6].

The gauge group of the unified theory is $SU(2)_L \times U(1)_Y$, where $U(1)_Y$ is a different copy of the symmetry seen in electromagnetism, the $U(1)_{em}$ group. In this picture the conserved quantity is Y, the weak hypercharge, and the conserved quantity for the $SU(2)$ symmetry is the weak isospin, T_3 . The previous quantity

conserved under $U(1)_{em}$ Q can be defined as a linear combination of the two $Q = T_3 + \frac{Y}{2}$. The $SU(2)_L$ suffix is not taken from the conserved quantity, T_3 , but from its most important property, its action on only Left Handed (LH) fermions. Fermions that are Right Handed (RH) have a weak isospin $T_3 = 0$ and do not interact via the weak force, whereas LH fermions have $T_3 = \pm\frac{1}{2}$ and interact via three gauge bosons. The W^\pm bosons have each an isospin of unit 1, with a sign defined by the name, and they govern an interaction from a particle of $T_3 = +\frac{1}{2}$ into one of $T_3 = -\frac{1}{2}$ and vice versa, according to conservation laws. The third boson given by the $SU(2)$ group alone is the W^0 boson of $T_3 = 0$, which allows interactions where the weak isospin stays the same. This is not a physically observed particle, as the electroweak unification leads to mixing between this and the boson given by the $U(1)_Y$ group to produce the photon and the Z^0 particle.

The Lagrangian formalism for a fermion field $\psi = \psi_L + \psi_R$ must be invariant under the transformations of both $U(1)_Y$ and $SU(2)_L$. The $U(1)_Y$ transformation of ψ and its gauge field B_μ are shown in Equation 2.16, and the $SU(2)_L$ transformations of ψ and the three gauge fields W_μ^ν in Equation 2.18.

$$\psi(\mathbf{x}) \rightarrow e^{i\frac{g'}{2}Y\alpha(\mathbf{x})}\psi(\mathbf{x})B_\mu(\mathbf{x}) \rightarrow B_\mu(\mathbf{x}) - \frac{1}{g'}\partial_\mu\alpha(\mathbf{x}) \quad (2.16)$$

$$\psi(\mathbf{x}) \rightarrow e^{igI\sigma_\nu\beta^\nu(\mathbf{x})}\psi(\mathbf{x}) \quad (2.17)$$

$$W_\mu^\nu(\mathbf{x}) \rightarrow W_\mu^\nu(\mathbf{x}) - \frac{1}{g}\partial_\mu\beta^\nu(\mathbf{x}) + \epsilon_{\exists\delta\theta}\beta^\delta(\mathbf{x})W_\mu^\theta(\mathbf{x}) \quad (2.18)$$

Using these formalisms the Lagrangian for the Electroweak Sector takes the form in Equation 2.19, where the covariant derivative is as defined in Equation 2.20.

$$\mathcal{L}_{EW} = \sum_{fermions} \bar{\psi}i\gamma^\mu D(\mu\psi - \frac{1}{4}\sum_{\theta=1,2,3} W_{\theta,\mu\nu}W_\theta^{\mu\nu} - \frac{1}{4}B_{\mu\nu}B^{\mu\nu} \quad (2.19)$$

$$\mathcal{D}_\mu = \partial_\mu - igI\sigma_\nu W_\mu^\nu(\mathbf{x}) - i\frac{g'}{2}YB_\mu(\mathbf{x}) \quad (2.20)$$

The gauge fields give rise to field strength tensors as before in QED and QCD, $B_{\mu\nu}$ and $W_{\mu\nu}^\theta$ defined in Equation 2.22.

$$B_{\mu\nu}(\mathbf{x}) = \partial_\mu B_\nu(\mathbf{x}) - \partial_\nu B_\mu(\mathbf{x}) \quad (2.21)$$

$$W_{\mu\nu}^\theta(\mathbf{x}) = \partial_\mu W_\nu^\theta(\mathbf{x}) - \partial_\nu W_\mu^\theta(\mathbf{x}) + g\epsilon_{\nu\delta\theta}W_\mu^{/\text{delta}}(\mathbf{x})W_\nu^\theta(\mathbf{x}) \quad (2.22)$$

Linear superpositions of the W_μ^1 and W_μ^2 give rise to the W^\pm boson fields, leaving the W^3 and B fields to give rise to the required fields A_μ and Z_μ with an orthogonal combination dependent on the weak mixing angle, the Weinberg angle $\tan \theta_W = g'/g$. However, whilst the W and Z bosons have mass, there are no terms in the existing \mathcal{L} that can explain that, nor if there were would it allow the photon to remain massless whilst repeating the symmetries.

2.1.2 EWSB and the Higgs Mechanism

In order to give mass to the W and Z bosons whilst retaining the necessary local gauge invariance, we say that $SU(2)_L \times U(1)_Y$ must be spontaneously broken into $U(1)_{em}$, the group of symmetries representing the electromagnetic sector. The simplest way to introduce such a breaking is known as the Higgs Mechanism, and corresponds to the addition of a scalar field. The Lagrangian for such an addition has the form $\mathcal{L}_h = (D^\mu\phi)^\dagger(D_\mu\phi) - V(\phi)$. Ensuring the change to the Lagrangian is invariant, there is a covariant derivative term and an additional potential. The potential introduced has the form

$$V(\phi) = \mu^2\phi^\dagger\phi + \lambda(\phi^\dagger\phi)^2 \quad (2.23)$$

Choosing a potential where μ^2 is positive leads to a minimum at $\phi = 0$, which does not solve our problem. However, if the parameter μ^2 is chosen to be less than zero, it results in a potential colloquially known as a “mexican hat” potential, shown in Figure 2.1. The minimum does not lie at $\phi = 0$, but in 3D space in a circle around ϕ , so there are an infinite number of minima hence introducing a degeneracy. There is a non-vanishing ground state, and as a particular state is chosen, the symmetry is broken. Interactions with the field lead to masses for the W and Z bosons. This leads to the existence of a massive scalar particle, known as the Higgs Boson, to date the only particle of the SM yet to be observed. The coupling strength of a particle to the Higgs field is thought therefore to govern its mass.

The distinction between the two forces caused by this symmetry breaking

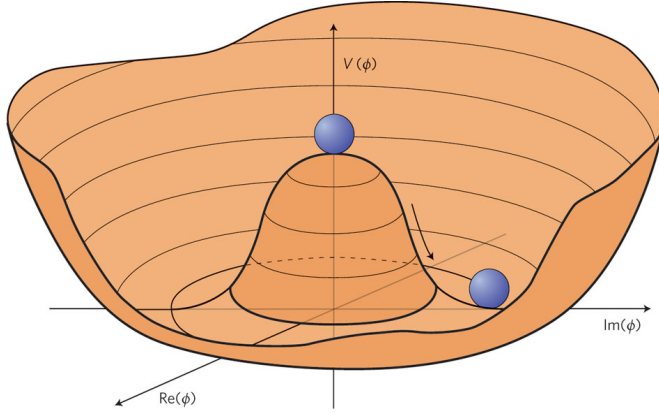


Figure 2.1: The Higgs Potential chosen where $\mu^2 < 0, \lambda > 0$ such that the minimum does not exist at 0, but instead in a ring of infinite minima about zero, thus introducing degeneracy and breaking the electroweak symmetry into that of QED. [7]

are due to a linear combination of the weak hyper charge and isospin, T_3 and Y that vanishes for the Higgs. As this defines the conserved quantity Q for the electromagnetic group, this is not affected by the Higgs, and thus the $U(1)_{em}$ group remains unbroken. Conversely, the weak portion interacts with the Higgs and the W^\pm and Z bosons acquire mass.

2.2 Motivation for Physics Beyond the Standard Model

The standard model has been widely successful, predicting the existence of particles such as the W^\pm and Z Bosons, and the t quark, showing impressive agreement with experimental findings at the level of 0.1%. However, there are several signs that it is not a complete theory, that more information is needed to describe physics at higher energy scales. On the theoretical side, it is dissatisfying that the SM does not currently incorporate the gravitational force, explain the existence of dark matter and dark energy. Neutrino masses and flavour mixing are also unexplained, and the Higgs is as yet undiscovered. In addition it requires several input parameters to tune the masses of particles and flavour mixing, generally viewed as inelegant as this reliance on experimental data does not reflect the fundamental picture of nature. The existing SM is therefore generally thought

of as an effective theory, a very low energy approximation to a more complete theory[8].

The incorporation of the gravitational force has not bothered particle physicists much at the electro-weak energy scale as the strength of the effects of gravity on fundamental particles is negligible compared to the other fundamental forces. However, at an energy known as the Plank Scale, $M_p \sim 10^{18}$ GeV quantum gravitational effects become important, leading to the breakdown of the existing QFT picture of the Standard Model. Thus new physics must exist at this energy scale, or before, indicating the SM is only valid up to some unknown energy scale. We think of the SM as a low-energy approximation of some larger more fundamental theory. One other fundamental problem, the hierarchy problem, shows that between the electroweak and the plank scales there lies theoretical dissatisfaction with the SM.

As there is both theoretical and experimental concerns over the SM, this provokes theories Beyond the Standard Model (BSM), many of which come in to play at the TeV scale, which we are able to explore for the first time with the LHC. A detailed description of a few of the most interesting shortcomings most relevant to this thesis is given below.

2.2.1 The Hierarchy Problem

Although the Higgs Boson has yet to be observed experimentally, its mechanism is necessary to the Standard Model to provide mass to the particles, and thus is considered to exist unless proven otherwise. However, while it solves the SSB problem, the Higgs theory introduces theoretical issues of its own. The presence of the Higgs in the SM ensures the WW scattering amplitude does not violate unitarity, but only whilst the $m_H < 1\text{TeV}$, providing an upper bound on the expected mass[9].

However, the mass of the Higgs, given by its self interaction received extremely large radiative corrections. This is due to the heavy fermion anti-fermion pair loop contribution, seen in Figure 2.2.

If each coupling with a fermion f has a term in the Lagrangian $-\lambda_F H \bar{f} f$, it contributes a quadratically divergent factor δm_H^2 that corrects the squared mass of the Higgs.

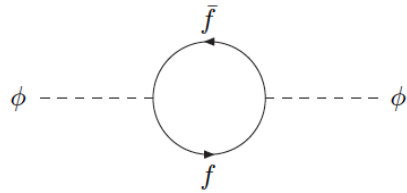


Figure 2.2: The loop contribution to the Higgs self-mass interaction from fermion-anti-fermion pairs in the SM

$$\delta m_H^2 = \sum_f -\frac{|\lambda_f|^2}{8\pi^2} \Lambda_{UV}^2 + \mathcal{O}(\ln \Lambda) \quad (2.24)$$

The factor λ_f represents the coupling for each type of fermion, which is largest in the case of the top quark, where $\lambda_t \approx .1$. The parameter Λ_{UV} is the *ultraviolet cutoff*, so named as it represents the smallest distance to probe in the calculation. It can be thought of as the scale at which the Standard Model is valid up to, as any new physics would change the theory.

If there were no new physics at a lower energy, it takes the value of the Plank Scale M_P , but in this case the correction will be 30 orders of magnitude higher than the 1 TeV upper bound justified experimentally[10]. As there exists nothing in the SM to fix the Higgs Mass, the theory requires fine-tuning, tweaking the parameters to agree with observational findings. This is generally accepted to be an inelegant method, as it requires the input of extra information, and indicates a gap in the fundamental description leading to searches for extensions to the Standard Model.

2.2.2 Cold Dark Matter

The existence of Dark Matter was postulated as early as 1933 by Zwicky [11], as the orbital velocities of galaxies in clusters were inconsistent with their observed mass, suggesting some additional mass was present but not luminous. Measurements of rotation curves of galaxies, cosmic microwave background and structure formation have confirmed this concept over the years. Experimental results from WMAP conclude only $\sim 4.5\%$ of the energy in our universe is made of the baryonic matter we see, while dark matter accounts for $\sim 23\%$ and the rest is comprised of another unknown, dark energy [12]. Although the existence of such

matter has been well documented, there is still no understanding of the physics behind the phenomena. In order to explain the properties a weakly interacting massive particle (WIMP) is required, and it must be electrically neutral. There is no provisions for such a particle in the SM, indicating additional particle content requiring extensions in the theory.

2.2.3 Unification of Coupling Constants

At the basis of theoretical particle physics is the observation of the symmetry and simplicity of nature. Unification, where several theories can be combined into one description, has undergone before, first Electricity and magnetism, and then electromagnetism with the weak force. While each of the three forces of the SM have their own coupling constant, as the energy scale is increased the coupling constants converge towards one another. However precision measurements show that within the current framework, there is no common point where all three intersect. In addition, at the Planck Scale as gravity's coupling constant would be of similar strength many hope for a Grand Unified Theory (GUT), occurring at this scale known also as the GUT scale. This is only possible with the incorporation of some new physics which would alter the trend of the couplings between the electroweak scale and this GUT scale.

2.3 Supersymmetry

Having discussed these major issues with the SM Theory, we move on to a discussion on a potential extension to the SM. There are several options, but this thesis will focus on the theory with the best solution to the three issues highlighted discussed in detail, beginning with a natural way to eradicate the hierarchy problem simply and without fine tuning.

The hierarchy problem could be removed, rather than controlled, if there were a way to cancel out the quadratic diverging term in the Higgs mass correction. As the correction for bosons has the opposite sign, the conception of a new symmetry was born, one between fermions and bosons. Known as SUperSYmmetry (SUSY), this theory extends the SM under this symmetry such that elementary particles in the SM each have a super partner differing by one half unit of spin as yet undiscovered, just as the anti-particles were once postulated. For every fermion

contributing to the quadratic divergence, a boson partner contributes the equal and opposite term, and thus the hierarchy problem cancels out and the mass of the Higgs can take a sensible value.

Under this symmetry elementary particles in the SM would each have corresponding super-partners, differing by one half unit of spin, such that a fermion has a scalar boson super partner, and vice versa. At the heart of supersymmetry is a transformation that changes the field of a fermion into that of a boson, and vice versa. The generator of the transformation shall be known as Q ,

$$Q|\text{fermion}\rangle = |\text{boson}\rangle, \quad Q|\text{boson}\rangle = |\text{fermion}\rangle \quad (2.25)$$

where the complex spinors that generate SUSY anti-commute, with the following relationships where P^μ is the generator of space-time translations and indices are suppressed:

$$\{Q, Q\} = \{Q^\dagger, Q^\dagger\} = 0 \quad \{Q, Q^\dagger\} = P^\mu \quad (2.26)$$

In addition to its neat solution to the hierarchy problem SUSY has several other consequences which lead to its position as the most favoured theory for new physics at the TeV scale. The inclusion of SUSY particles to the SM has the side affect of altering the runnings of the gauge coupling constants of the three fundamental forces. Figure 2.3 shows the running constants from the SM alongside those with the SUSY model incorporated. Whilst the SM allowed only two to intersect at any point, SUSY alters them such that they are consistent with theories of Grand Unification, as the three are equal at the GUT scale $Q \approx 10^{16}$ GeV.

Rather than a motivation, this is a pleasant coincidence, but lends plausibility to the theory. It also shows promising features necessary for theories to incorporate gravity, although it does not finish the job. SUSY itself cannot be the final fundamental theory of particle physics, but is an extension which shows much promise, and is a pre-requisite for many higher energy theories such as most formulations of String Theory[13]. The final, perhaps most exciting feature of SUSY is that it can offer a candidate for the particle that represents dark matter with the introduction of a new quantum number R - Parity.

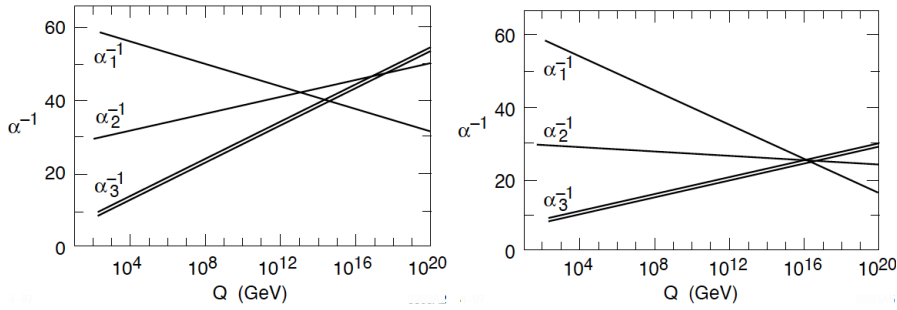


Figure 2.3: (a) The SM running gauge coupling constants for $SU(3)_C \times SU(2)_L \times U(1)_Y$ are shown with increasing energy scale Q . (b) same plot is made after the supersymmetric extension to the Standard Model has been applied. The double lines for α_3 indicate the error in experimental measurement, which is negligible for the other two. [14]

2.3.1 R-Parity

Constructing the most general form of SUSY, terms appear which allow processes which violate two quantum numbers, the baryon number B and the lepton number L . Whilst there is no theoretical reason for this to be a problem, these interactions have not been observed, and are constrained heavily. An undeniable constraint is the lifetime of the proton, which is very large, whereas these processes would facilitate its decay. whilst B and L are not fundamental symmetries in the theory, it is possible to construct a new quantum number R defined in Equation 2.27 which can be required as a symmetry R-parity[15]. It distinguishes between particles from the SM and the sparticles introduced by SUSY, as under this construction, all SM particles carry R of +1 and all super partners carry -1.

$$R = (-1)^{3(B-L)+2S} \quad (2.27)$$

Whilst terms in the Quantum Field Theory do allow for the possibility of violation of this parity, experimental measurements has excluded this for sparticles with masses on the TeV scale, and therefore those within the reach of the LHC. Thus the majority of searches consider models with a symmetry which forbids this violation and conserves R_p . Several phenomenological consequences that transcend specific models arise from this assumption which provide the backbone to SUSY searches at the LHC:

- In order for SUSY particles to be produced at the LHC under this framework, they must be pair produced from SM particles.
- The heavier particles will cascade down a decay chain ending through creation of the lightest of the supersymmetric particles, denoted the Lightest Super Partner (LSP)
- The LSP must be stable as it cannot decay into SM particles, and through cosmological bounds must be electrically neutral.

These characteristics of the LSP show us that it is a WIMP, the type of particle that is sought in Dark Matter searches. These particles will not interact in a detector, therefore are characterised in an experiment as large amounts of missing energy. As this is directly a characteristic of a WIMP in the final state, such a signature represents not only SUSY but is shared by other new physics models with a dark matter candidate particle.

Models may be constructed to constrain the violation of B and L without R-parity conservation, but those shall not be considered in this thesis, as this unique feature provides both physical motivation and a search strategy for physics at the LHC.

2.3.2 MSSM

Whilst there are many ways to construct mathematically the theory of Supersymmetry, it is usual to do it in the way which introduces the least number of new degrees of freedom. This corresponds to the minimal particle contact required to satisfy the core symmetry, which corresponds to one new degree of freedom for each existing SM one. This approach is known as the Minimal Supersymmetric Standard Model (MSSM), and has an additional new particles, known as a sparticle, for each known SM particle.

The particles are arranged to fit the irreducible representation of the symmetry, in *supermultiplets*, each of which contains both fermions and bosons. The number of bosonic and fermionic degrees of freedom are therefore equal in any supermultiplet. There are two types of supermultiplet available, a chiral supermultiplet which describes a left-handed fermion, its right handed anti-particle, a complex boson and its conjugate, and a vector multiplet - a massless

vector field and a left handed fermion, which result in the fermion and its anti-particle and two transversely polarised vectors bosons[16].

The names of the spin-0 bosons that partner the SM fermions are prefixed with “s-”, known as squarks and sleptons, collectively the sfermions. As the SM contains a distinction between left and right handed fermions, the boson super partners have one of each too, and are labelled RH and LH, but it is important to remember this is not a description of the super partner itself, merely a label to describe the SM particle it is associated with. The particles are written with a tilde above the SM symbol so the top quark t becomes the ”stop” quark, \tilde{s} .

The names of the fermions from the SM bosons are appended with “-ino” such as the super partners of the gluons, the gluinos. However, for the other fundamental SM bosons, identifying their super-partners is not so simple. The symmetry acts not on the results of electroweak symmetry breaking but on the fields of the $SU(2)_L \times U(1)_Y$ group. Thus there should be three Winos W and a Bino \tilde{B} .

The Higgs receives different treatment in SUSY as from in the SM, where the scalar field gives up three degrees of freedom to give mass to the vector bosons W^\pm and Z . In SUSY, instead two supermultiplets with differing quantum number are required to maintain the electroweak symmetry breaking, one chiral and one vector. These give mass respectively to the up-type quarks of charge $-1/3$ and the down-type quarks of charge $+2/3$, and thus are named H_u and H_d [17]. Where the SM has one complex doublet, the MSSM has two complex Higgs doublets, hence the sector has 8 degrees of freedom. Three are lost to give the W and Z bosons mass in electroweak symmetry breaking, leaving five which represent five Higgs boson particles: the charged Higgs bosons H^\pm , and three neutral bosons h , H and A . The corresponding super-partners are known as the higgsinos.

2.3.3 Supersymmetry Breaking

In order to satisfy an exact symmetry, one would expect that each super-partner would have the same characteristics as its SM partner, including its mass. This would indicate they were within the reach of previous physics experiments, but it is clear this is not true as there has been no experimental evidence of particles in the energy spectra previously covered by experimental research. Drawing parallels with the problem of electro-weak symmetry breaking, we say SUSY is

broken by some mechanism, resulting in particles with heavier masses than their counterparts. Although the size of these masses could be theoretically anything, in order for SUSY to eliminate the hierarchy problem this breaking must occur at the Electroweak Scale, which puts an upper bound on the mass differences of 1 TeV.

This is known as “soft” SUSY breaking, and offers the hope of discovering this new physics at the TeV scale, as is now possible for the first time with the LHC. This involves “soft” mass terms incorporated into the Lagrangian theory that do not introduce quadratic divergences that would provide a new “hierarchy problem”. However, the nature of this breaking is not known and thus it is traditional to formulate it in the theory to contain all the mass and mixing terms allowed by the underlying symmetry, which gives arbitrary masses to the sparticles. As there are many unknowns this introduces a large number of parameters to the system. Not all is lost, as SUSY is still capable of making useful predictions, however to compete the theory an understanding of the nature of SUSY breaking is really required.

Due to electroweak symmetry and soft SUSY breaking the fermions superpartners of the $SU(2)_L \times U(1)_Y$ group are not generally the mass eigenstates. Instead the winos and bino mix with the higgsino fields to produce the mass eigenstates in two groups, the charginos $\tilde{\chi}_{1,2}^{\pm}$ and the neutralinos $\tilde{\chi}_{1,2,3,4}^0$.

2.3.4 Minimal Supergravity and the Constrained MSSM

Even assuming a minimal particle content, the MSSM has a large number of free parameters, introduced through SUSY and Electroweak symmetry breaking, 105 new parameters in addition to the 19 already present in the SM. When it comes to experimental searches, this is an unworkable number, for to examine possible behaviour of SUSY one would have to look in 105 dimensions. Thus for the purpose of making models to work with, it is desired to constrain this number in the theory. One popular GUT model is the theory of minimal SUper GRAvity, otherwise known as mSUGRA.

The many parameters of the MSSM are in fact not all constants, but rather vary with the energy scale. Thus, to contain the model we can assume that there is some “hidden sector” (perhaps on the order of the M_P) which contains fields with no couplings to what is now thought of as the “visible sector” of

the MSSM. There should then be some messenger between the two, that allows supersymmetry breaking to be mediated to the MSSM to provide the soft terms. One popular theory as to the nature of this messenger is that it is “gravity mediated”.

The MSSM combined with the theory of mSUGRA is called the Constrained MSSM, or CMSSM, as the number of free parameters has been reduced to a manageable five. These factors are:

- A common scalar mass m_0
- A common gauging mass $m_{1/2}$
- The SUSY Breaking common trilinear coupling A_0
- The ratio of the vacuum expectation values of the two Higgs Fields $\tan \beta$
- The sign of the Higgs parameter, $\text{sign}(\mu)$

With this relatively small parameter space it is possible to construct models with which to construct search strategies, and allows us to exclude regions with the advent of new results. A given point in mSUGRA space defines the mass hierarchy of the squarks, gluinos, charginos and neutralinos, therefore governing the interactions that are possible, as well as the identity of the LSP. Thus in different regions the production mechanisms can differ, however in the majority of phase space the LSP is the lightest of the neutralinos, $\tilde{\chi}_1^0$. For convenience, mSUGRA is shown graphically in the $m_0 - m_{1/2}$ plane, for set values of the other three parameters.

There are other theories that support mechanisms of SUSY breaking, such as Gauge-Mediated Symmetry Breaking (GMSB) and Anomaly Mediated Symmetry Breaking (AMSB) but these are not considered for the purpose of this thesis.

Current Limits on the CMSSM

Two types of limits exist in mSUGRA space, those imposed theoretically and those that result from experimental data. Of the latter, some are contributed from cosmology, and others from particle physics.

There are some regions of the parameter space where the masses of the particles have a hierarchy which results in the stau being the LSP. This is

theoretically forbidden as the LSP certainly contributes some if not all of the dark matter in the universe, and it is known to be neutral.

In addition, a further region is excluded whereby the relic density of the LSP is consistent with the WMAP measurement of the Dark Matter density.

2.3.5 Production Mechanisms in pp collisions

At a proton-proton collider at TeV energies such as the LHC, as discussed before we can consider the protons as a set of partons each carrying a fraction of the total momentum. It is these quarks and gluons that collide. At such high energies these can be from the gluons and the sea as well as the valence quarks, thus there are qq , $q\bar{q}$, qg and gg collisions to consider. Assuming SUSY exists within the reach of the LHC, indicated by the restriction imposed on the mass differences of SUSY Breaking, then from these interacting pairs large production rates of both squarks and gluinos are expected. Cross sections in the region of 100 pb to 1fb are possible for SUSY sparticles with masses between 0.5 TeV and 1 TeV [18]. Predominantly the production is the result of strong processes resulting in squarks and gluinos, although weak production does exist albeit at smaller cross sections. Decays from these particles through charginos and neutralinos would result in production of the LSP, but the structure of these decays depends on the mass hierarchy of the sparticles, which is determined by the values of m_0 and $m_{1/2}$. Thus a chosen point in this plane represents a certain set of kinematics. SUSY production in these collisions is dominated by the pair-productions $qq \rightarrow \tilde{g}\tilde{g}, \tilde{q}\tilde{q}, \tilde{q}\bar{q}$. The relative cross sections of these decay modes depend on the region of mSUGRA

Within mSUGRA there are three distinct regions which exhibit different decay modes, defined by the mass relationship between the gluinos and the squarks. These can be seen Figure 2.4 , where the diagonal green lines represent a cross-over in the squark-gluino hierarchy. Passing left-right on the diagram, the regions are:

Region1: $m_{\tilde{g}} > m_{\tilde{q}}$ As the gluinos are heavier than the squarks, the general form of decays is

$$\tilde{g} \rightarrow \tilde{q}\bar{q}, \tilde{q} \rightarrow q\chi \quad (2.28)$$

Region 2: $m_{\tilde{g}} < m_{\tilde{q}_L}, m_{\tilde{g}} > m_{\tilde{t}_1}$ Here the mass of the gluino between that of the heaviest and lightest squark, therefore more complicated decay

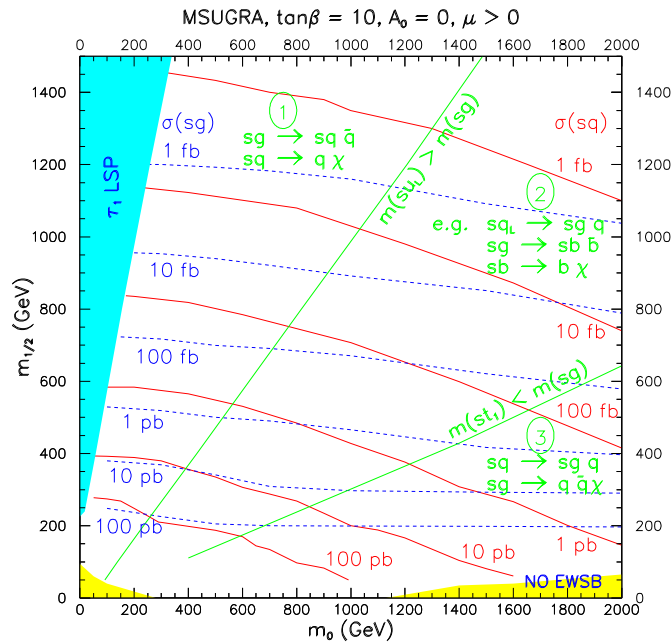


Figure 2.4: The $m_0 - m_{1/2}$ plane of m SUGRA depicting diagonal lines separating three distinct regions of mass hierarchies based on the mass difference of squarks and gluinos. Lines of constant production cross section for squarks and gluinos are shown in red and blue respectively. The allowed decays in each region are shown, where sq denotes a squark, and (sg) a gluino.[19]

relationships between the two are allowed, and these depend on exactly which quarks are heavier and which lighter. The \tilde{q}_L are the heaviest, while states such as \tilde{b}_1 and \tilde{t}_1 are some of the lightest. The heavier quarks decay to lighter squarks and to gluinos, and the gluino decays to lighter squarks.

Region 3: $m_{\tilde{g}} < m_{\tilde{q}}$ Finally in this region the gluino is lighter than any squark, and the allowed decays take the form

$$\tilde{q} \rightarrow \tilde{g}q, \tilde{g} \rightarrow q\bar{q}\chi \quad (2.29)$$

As the dominating decay of both squarks and gluinos produce quarks, we expect in a SUSY event many hadronic jets from these sources along with the gluon radiation from the incoming and outgoing partons. Thus a traditional SUSY signature that provides the basis for this thesis is that of multiple jets and evidence of a (missing) LSP.

Chapter 3

The Compact Muon Solenoid Experiment at the LHC

3.1 The Large Hadron Collider

The Large Hadron Collider (LHC) is a double-ring circular synchrotron at CERN designed to collide two proton beams with a centre of mass energy $\sqrt{s} = 14$ TeV at a final design luminosity of $10^{34}\text{cm}^{-2}\text{s}^{-1}$. The energy and luminosity have been chosen to with the aim of discovering new physics at the TeV scale, out of reach to previous experiments, where theories predict new physics both within and outside the Standard Model. It will also be used to collide heavy lead ions (Pb^{82+}) to an energy of 2.76 TeV per nucleon, in specific runs, with the purpose of investigating QCD matter at energies 30 times higher than previous experiments. The LHC has unparalleled reach in the search for new physics, not only due to the significant increase of energy over the Tevatron, the previous record holder, but also due to the intensity of the beam delivered. The number of events produced by a given physical process depends proportionally on its cross section σ , and therefore proportional to \sqrt{s} and the luminosity \mathcal{L} , which has the dependence shown in Equation 3.1 below [20]:

$$n = \mathcal{L}\sigma, \quad \mathcal{L} = \frac{N_b^2 n_b f_{rev} \gamma_r}{4\pi\epsilon_n \beta^*} F \quad (3.1)$$

where N_b is the number of particles in a single bunch, n_b is the number of bunches in a beam, f_{rev} the frequency of revolutions, γ_r is the relativistic gamma,

ϵ_n is the beam emittance and β^* is the beta function associated with the collision point. The geometric luminosity function F provides a reduction factor based on the beam crossing angle, and depends on the full crossing angle at the IP θ_c , and the transverse and longitudinal RMS beam dimensions σ_* and σ_z with the following dependency:

$$F^2 = \frac{1}{1 + (\frac{\theta_c \sigma_z}{2\sigma_*})} \quad (3.2)$$

Situated in the tunnel of the previous e^+e^- machine LEP located underneath the Franco-Swiss border, the LHC is mostly circular with a circumference of 27km, consisting of 8 arced sectors connected by 8 straight sections in which are the numbered Interaction Points (IP), where the two beams circulating in opposite directions can be allowed to intercept. To bend the protons around the rings, the beams must experience opposite dipole fields from one another, and have two separate vacuum systems. As the tunnel has restricted space available, the dipole magnets are twin bore with two coils and, but share the same structure and cryogenics. The 1232 superconducting dipole magnets present must produce a field in excess of 8T due to the high momentum of the protons, and thus have a high current and must be cooled below 2K by liquid helium to ensure safe operation. The beams are non-continuous, grouped in "bunches" at intervals. In the straight sections the two beams share the same beam line and can be directed to coincide at the IP's. In order to maximise the number of interactions, quadropole magnets are used to collimate the beam providing a minimum cross section at the moment of interaction.

At four of these IP's are located the four main detectors that analyse the data from collisions: the two high luminosity experiments ATLAS (A Toroidal LHC Apparatus) at IP1 and CMS(Compact Muon Solenoid) at IP5 are multi-purpose detectors analysing the p-p collisions for signs of new physics. At IP8 the LHCb (LHC beauty) detector looks for CP violation and other rare decays in a forward detector with lower luminosity runs, and ALICE (A Large Ion Collider Experiment) at IP2 will investigate the lead-lead ion collisions. The locations of the detectors in the LHC ring is shown in Figure 3.1 [21] .

The magnets are optimised for beams of a certain energy range, and therefore the protons cannot be fully accelerated in the LHC. Therefore supply of protons are delivered through a series of other machines that make up part of the CERN accelerator complex, the layout of which is shown in Figure 3.2.

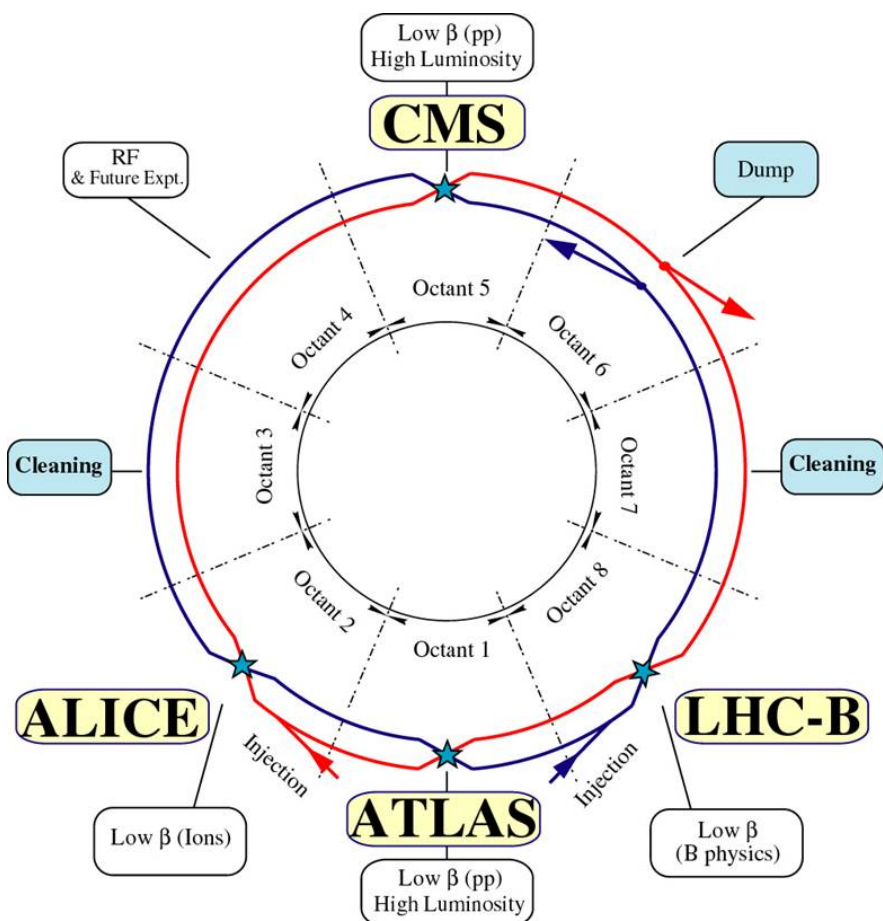


Figure 3.1: Schematic of the LHC ring and the location of the major experiments.

A beam of 50MeV protons is created in LINAC2, in 6 bunches, and each bunch is then split into 12, resulting in 72 bunches which are fed into the Proton Synchotron Booster. After accelerating to an energy of 1.4GeV, they enter the Proton Synchotron, where they are accelerated to 26GeV, and fed in sets of 2-4 into the Super Proton Synchotron. Now 144-288 bunches, they are accelerated to 460GeV ready of injection into the LHC. Twelve of these sets are injected into the LHC at one, directly into both rings, giving a nominal bunch density of 2808, with a spacing of 25ns. This process takes around 20 minutes, and then the LHC takes a further 20 minutes to ramp the protons up to the desired energy. The magnets preventing the beams coinciding in the detectors are turned off and stable collisions occur. However, the luminosity falls regularly as the run progresses, and after 6-12 hours, it has fallen below an acceptable level, and the beam is dumped before repeating the process again.

Using these short runs of high luminosity it is possible for the LHC to take vast amounts of data, and assuming 200 days of data taking a year at design luminosity the machine will be able to deliver 100fb^{-1} a year. As part of the early phase of operation the machine was operated in 2010-2011 at 3.5 TeV per beam, $\sqrt{s} = 7\text{TeV}$, in order to protect the magnets, and is not expected to run at full energy until 2014. The 2011 run delivered 5.727fb^{-1} data, the first 1.1fb^{-1} of which was delivered by the end of June, and is considered for this thesis.

3.2 The Compact Muon Solenoid

The Compact Muon Solenoid (CMS) is one of the two high-luminosity multi-purpose detectors at the LHC, designed to capitalise on the full range of physics opportunities available as a new energy scale is probed. These goals are pursued through the design and construction of the detector and development of software for the reconstruction of physics objects. The detector is constructed of several detector sub-systems contained inside and wrapped in layers around a central 13m long 4T super conducting solenoid as shown in Figure 3.3.

The detector is 21m long, 15m wide and weighs 14000 tonnes, and consists of five wheel-like barrel sections and two end-caps to close. In order for CMS to search for new physics among the high order of Standard Model backgrounds, it is of key importance to develop a detector which has impressive energy and

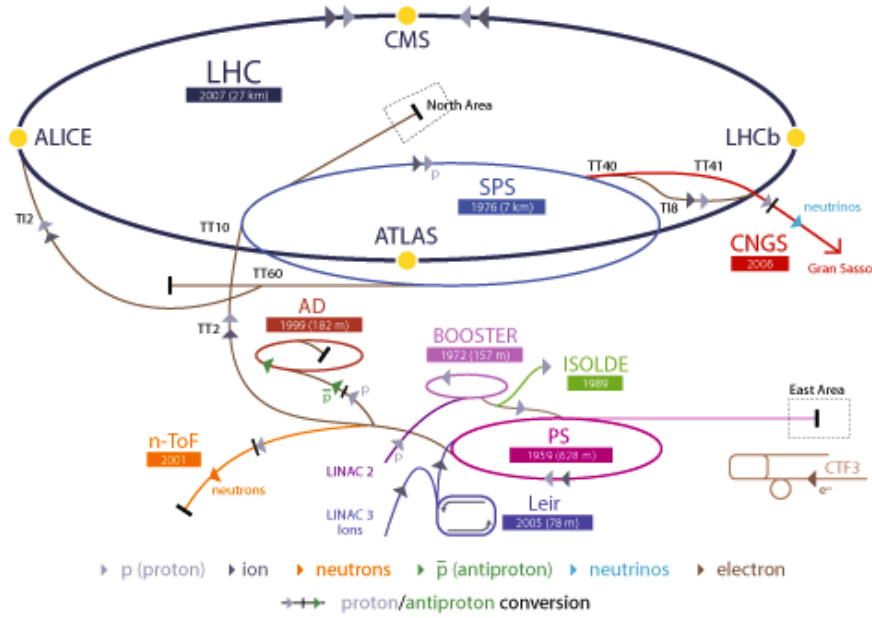


Figure 3.2: Layout of the CERN accelerator complex, illustrating the relationship between the LHC and its supporting accelerators tasked with delivering proton beams at 460 GeV.

momentum resolution, and particle identification. Different particles interact differently with matter and therefore a number of sub-detectors are needed in order to gather all the relative information. This is then combined in order to reconstruct the objects.

The high magnetic field was chosen in order to achieve the bending power necessary for good charged particle momentum resolution. The inner bore of the solenoid is large enough that the inner tracker and the calorimeters are located inside, which minimises the material the partials pass through before entering the calorimeters. This allows a good energy measurement. Four muon "stations" of aluminium drift tubes are integrated within the iron magnetic field return yoke. The full design description can be found in the CMS Technical Design Proposal [22]. As different particles pass through the detector they interact in the sub-systems depending on their type. A transverse slice through the detector illustrating the path through the machine of each type of particle is shown in Figure 3.4

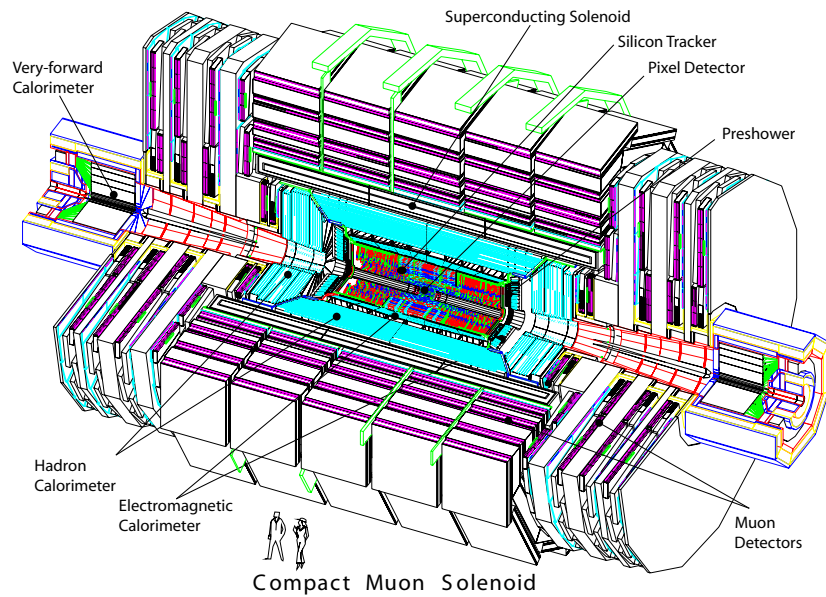


Figure 3.3: A cutaway diagram of the CMS detector structure identifying the main individual sub-systems.

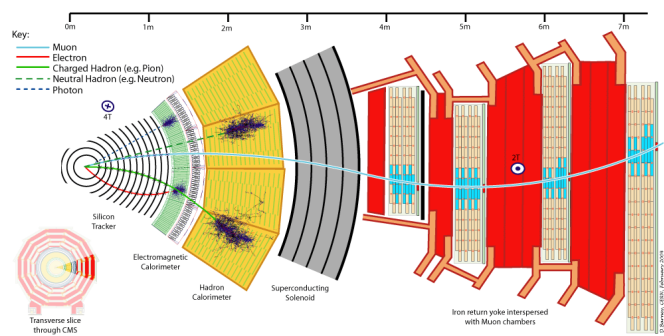


Figure 3.4: Transverse slice through the CMS Detector showing each type of particle and how it interacts with the sub-detectors.

3.2.1 Coordinate System

The coordinate system chosen by CMS uses the nominal interaction point within the detector as the origin. The x-axis points radially inwards to the centre of the beam pipe, and the y-axis points vertically upward. The z-axis then points in the direction of the beam. The azimuthal angle ϕ is defined as the angle from the x-axis in the x-y plane, and the polar angle θ from the z-axis. However, it is common convention to express θ in terms of the Lorentz Invariant quantity, pseudorapidity $\eta = -\ln \tan(\theta/2)$, as particle production is approximately uniform in η . The transverse components of the energy and momentum, denoted E_T and p_T are then calculated from the x and y components.

3.2.2 Superconducting Magnet

The geometry of the magnetic field is integral to the design and cylindrical structure of the CMS detector, as it uses a global solenoidal magnet. A strong magnetic field is essential to the design of a detector, bending charged particles in order to measure their charge and momentum. In order to ensure that the curvature is significant even with particles of high momentum, the CMS solenoid is designed to be capable of delivering a homogenous field of 4T. Consisting of four layers of NbTi coils, in a vacuum with a cryogenic system maintaining a temperature of 4.5K, the solenoid has a diameter of 5.9m and length 12.5m, and when operating at full current is capable of storing 2.6 GJ of potential energy.

As the solenoid is so large, not only the inner tracking system but also both calorimeter sub-detectors can be accommodated in the interior, giving significant advantage to electromagnetic and jet energy resolution as particles will not have traversed the high-density magnet coil before these measurements are taken. The flux is returned with a large iron yoke of $10^7 kg$, surrounding the inner magnet and built with a barrel of 5 wheels, and two end-caps each containing three disks. The muon system is built within the iron return yoke, in order to take advantage of the reverse magnetic field produced in the outer region, and thus follows the same structure. The drawback of a solenoidal field is that it had strong inhomogeneity in the end-caps, affecting the performance of the muon subsystem, which shall be discussed later.

3.2.3 Tracker

The first sub-detector encountered by particles is the multi-layer silicon tracker, which records precise information about the path of charged particles bending under the magnetic field. It is placed as close to the interaction point as possible in order to distinguish the primary interaction from secondary vertices of particles with significant lifetimes. This is particularly important in the case of identifying B mesons, which can travel a measurable distance before decaying.

The tracker is divided into regions defined by the radius r from the interaction point, as the expected particle flux decreases rapidly as the radius increases. This is due to the high magnetic field, which causes low momentum particles to have small radial helical trajectories.

Nearest to the primary vertex at 4cm, where the expected particle flux is at its highest ($\sim 10^8 \text{ cm}^{-2} \text{s}^{-1}$) are 66 million silicon pixel detectors of size $100 \times 150 \mu\text{m}^2$, arrayed in three barrel layers and two end-cap disks. This region is laid out to optimise the resolution in determining the vertex position, delivering a granularity of $10\mu\text{m}$ in the $r\text{-}\theta$ plane and $20\mu\text{m}$ in the $r\text{-}z$ plane. Pixel detectors have the advantage of being able to measure all three coordinates of the particle simultaneously. However this requires a huge number of readout channels and drives the costs of construction up. For this reason these are chosen for the innermost region where the flux is highest, while the rest of the detector are composed of silicon micro-strip devices.

Outside of the pixel detector lies the silicon strip tracker beginning at $r = 20\text{cm}$, divided into two parts, the inner and outer components. As the flux of particles expected is lower than in the pixel detector, the use of 11.4 million silicon strip detectors allows the desired granularity while reducing costs. Whilst these do now allow a simultaneous 3-coordinate measurement, the layers are constructed at known angles to one another and therefore combined together all three coordinates can be measured. The inner region, immediately outside the Pixel tracker, is composed of four barrel layers (TIB) and closed with three disks (TID) on each end, occupying the region up to $r=55\text{cm}$, where the microstrip sensors are $320\mu\text{m}$ thick oriented along the beam line in TIB and radially in the TID. The outer region has 6 barrel layers (TOB) further apart than in the inner sector, and closed with 9 end-caps (TEC) on the end of the barrel, extending out to $r=116\text{cm}$. The strips here are $500\mu\text{m}$ thick

In total the tracker covers a total area of 205m^2 with 76 million channels and provides a transverse momentum measurement for high momentum tracks with resolution 1-2% in the region $|\eta| < 1.6$.

3.2.4 ECAL

Immediately outside of the tracker, and still within the magnet core, sits the Electromagnetic Calorimeter (ECAL), used to measure the energy of electrons, photons and pions via the energy they lose through radiation. Electrons lose their energy in the material through bremsstrahlung, and photons by decaying to an electron-positron pair. Using a hermetic homogenous calorimeter of scintillating crystals, this energy can be converted to scintillation light which is picked up by a light sensitive detector.

The use of high density crystals allows a fast calorimeter which has fine granularity and is radiation resistant, requirements which are essential in the LHC environment. After rigorous research and development, lead tungstate (PbWO_4) crystals were chosen as the optimal solution to the requirements of LHC operation, due to a number of desirable characteristics. The extremely short radiation length $X_0 = 0.89\text{cm}$ allows the construction of a compact ECAL which therefore can reside within the solenoid, hence reducing the layers of material the particles have already passed through. In addition, the material has a low Moliere radius (2.2cm) meaning the transverse size of the electromagnetic shower is small, leading to good shower position resolution and separation. It is also essential that a fast scintillator is used, in order to distinguish between bunch crossings. In crystals of PbWO_4 80% of the scintillation light is emitted within 25ns, the bunch spacing of the LHC. Finally the crystals are hard to radiation, as their method of scintillation is resistant to radiation damage.

The ECAL is structurally divided into three distinct regions, the End-caps (EE), the Barrel (EB) and the Preshower (PS), which together cover a pseudorapidity range $|\eta| \leq 3$. The ECAL Barrel is a cylindrical arrangement of 61200 PbWO_4 crystals covering the pseudo rapidity range $|\eta| \leq 1.479$ with a granularity of $\Delta\eta \times \Delta\phi = 0.0174 \times 0.0174$. The radius to the front-face of the crystals is 1.29 m.

The ECAL is closed by two identical end-cap regions, which cover the range $1.479 \leq |\eta| \leq 3$ at the margins of the barrel, each consisting of 7324 crystals

divided into two halves, or *Dees*. Precision energy measurements are possible up to $|\eta| = 2.6$, but crystals are include up to $|\eta| = 3$ to assist the forward-direction energy-flow measurement. The end cap crystals are also wedge shaped with a square front face $28.62 \times 28.62\text{mm}^2$ and a square back face $30 \times 30\text{mm}^2$. The crystals point slightly away from the interaction point in order to make the end-caps hermetic, and are grouped mechanically into 5×5 super-crystals (SC).

The size of the crystals is chosen to reflect the properties and requirements, such that the front face surface area is 22mm x 22mm (the size of the Moliere radius) and the longitudinal depth of the crystals is 230mm, which is $25.8 X_0$ in the barrel, hence allowing a fine granularity and a compact ECAL. In the end-caps the presence of the PS allows for shorter crystals, of 220mm, corresponding to $24.7 X_0$.

A additional component, the Pre-Shower is present in front of the end-caps covering a range of $1.653 \leq |\eta| \leq 2.6$ and consists of two layers of absorbing lead converters and silicon detectors. The primary function of the PS is to identify neutral pions that decay into two photons in the end-caps, which can fake a high-energy photon. It also possesses a high granularity, and therefore is used to improve position determination of particles, and helps the identification of electrons against minimum ionising particles. The two layers of the PS have their strips orthogonal to one another such that the first layer has vertical strips to measure the critical position, and the second horizontal strips for the horizontal position.

The scintillators are read out using photodetectors, which convert the scintillating light of the crystals into an electric signal. The crystals were chosen by a rigorous optimisation of the properties required, which results in a high-performance ECAL, however this material has a relatively low light yield. In order to overcome this, photodetectors designed for use in a magnetic field with intrinsic gain are used. Vacuum Phototriodes (VPTs) are used in the end-caps. These are unsuitable in the central region due to high magnetic, but due to lower radiation levels Avalanche Photodiodes (APDs) are used. Both the crystals and the photodetectors are sensitive to temperature changes, so a stable temperature must be maintained. Radiation damage to the crystals decreases with temperature, but so do the thermal effects which result in recovery. The operational temperature, 18C is chosen as it is the point of equilibrium between

damage and recovery.

The resolution of an ECAL can be described as a function of the energy E in GeV, shown in Equation 3.3, for energies below about 500 GeV [23]. Above this shower leakage from the back of the crystals become non-negligible.

$$\left(\frac{\sigma}{E}\right)^2 = \left(\frac{S}{\sqrt{E}}\right)^2 + \left(\frac{N}{E}\right)^2 + C^2 \quad (3.3)$$

The stochastic term S represents fluctuations related to statistics, including photoelectron statistics and intrinsic shower variations. The noise term N takes into account electronic noise summed over readout channels, and the constant term C accounts for the uncertainty in calibration and the detector non-uniformity. Measurements from test beam reconstructed energy distributions show values for the terms to be $S = 2.8 \pm 0.1\%$, $N = 0.12 \text{ GeV}$ and $C = 0.30 \pm 0.01\%$.

3.2.5 HCAL

Outside the ECAL lies the Hadronic Calorimeter (HCAL), responsible for the measurement of the hadronic activity of an event. This also leads to a measurement of apparent missing energy from neutrinos or exotic particles, an important quantity in many searches for new physics. In order to measure the energy of hadrons in a compact space, a sampling calorimeter of interleaved layers of absorbers and scintillators is used. The absorbing material forces hadronic showering through nuclear interaction with heavy nuclei, and the active scintillating material then detects samples the showers of charged particles produced. The absorber material is described by the interaction length λ_I , the distance a hadron will travel through the material before it has lost roughly 63% of its energy through nuclear interactions.

The HCAL is divided into several sections, defined by pseudo-rapidity in order to optimise the resolution under different conditions. Within the space between the ECAL and the magnet coil lie the HCAL Barrel (HB) at $|\eta| < 1.305$, and the HCAL End-Caps (HE) at $1.305 < |\eta| < 3.0$, hermetically joined to completely surround the ECAL. In order to increase the hermicity of the HCAL, and therefore improve the accuracy of the missing energy measurement, the two elements of the HCAL Forward calorimeter (HF) overlap with the HE and extend the range in pseudorapidity to $|\eta| < 5$. There is also a complimentary layer

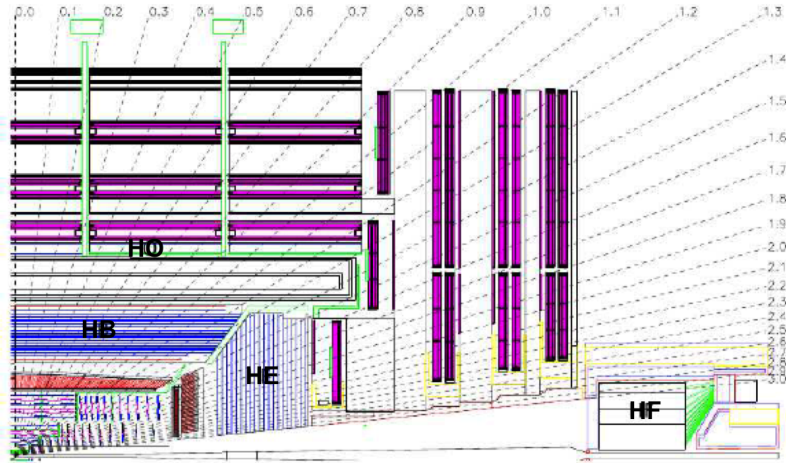


Figure 3.5: Diagram of one quadrant in the $r\theta$ plane showing the locations of the components of the HCAL: HB, HE, HO and HF, with lines of constant η shown.

of scintillators on the outside of the coil, known as the HCAL Outer (HO). This provides shower containment in the central region, where the number of interaction lengths travelled by a particle is at its lowest [24].

The barrel consists of two halves each with 18 identical azimuthal wedges, extending outwards 0.96m. Each wedge has 17 layers of 3.7mm thick plastic scintillator, interspersed with brass absorber plates, with the exception of the innermost and outermost absorbers, made from stainless steel to add structural stability. Directly behind the ECAL is placed the first active layer, with more than double the scintillator thickness (9mm) to actively sample the articles traversing the support material between the ECAL and HCAL. The final layer also has this thickness to catch showers that form late in the absorber.

A similar structure makes up the end-caps with 18 wedges in ϕ containing 19 active plastic scintillators with brass absorbers between. The number of interaction lengths travelled by particles in the HB and HE is dependent on the η of the particle, and while it is 10 at high η , in the central region this is as low as 5. In order to compensate for this, an outer barrel detector is added, consisting of two layers of scintillating material outside the magnet, and therefore utilising the core as an absorber. This extends the total thickness of the full calorimeter to at least 11.8 interaction lengths.

The design of the forward calorimeters is driven by the need for radiation

hardness, as the region closest to the beam line has an energy density up to seven times greater than in the central region. Thus absorbers made of stainless steel and active scintillators of quartz fibres are chosen. Twelve ϕ wedges are located 11.2m from the point of interaction, with the fibres parallel to the beam.

Measurements of hadron energies in the region $|\eta| < 3.0$ rely not only on the HCAL setup described, as a significant fraction of hadrons with have begun to shower while travelling through the ECAL, which contributes around one interaction length. The hadronic component of these showers will continue on into the HCAL, but much of the initial electromagnetic activity can be contained in the ECAL, thus use of measurements in both calorimeters are combined to reconstruct the true energy of a hadron. Using test beams over a range from 2 to 350 GeV/c the resolution for the reconstruction of hadron energy for the HCAL and ECAL combined is given by the following equation [25].

$$\left(\frac{\sigma}{E}\right)^2 = \left(\frac{84.7\%}{\sqrt{E}}\right)^2 + (7.4\%)^2 \quad (3.4)$$

3.2.6 Muon System

Interleaved in the iron return yoke of the detector are the components of the Muon System (MS), an important design feature giving CMS its middle initial. Many new physics signatures at high energy have final states with high momentum muons, and therefore accurately measuring these is crucial for many analyses, including Higgs and SUSY channels. As muons have high mass they interact little in the calorimeters, and thus retain a high percentage of their energy by the time they reach the iron return yoke. Putting the MS here far away from the interaction point allows finer precision, utilising the high magnetic field to bend even high momentum muons, and measuring the bending angle.

Muon momentum resolution using the MS is dominated at low energies ($0 < p_T^\mu < 200$ GeV/c) by the multiple scattering that occurs in the material prior to the first muon station, and therefore a better resolution could be obtain during the tracking system. However, it is possible to use the muon trajectory after the yoke to extrapolate back to the interaction point. Using the tracker and muon system together improves identification and measurements, especially as any particle detracted in the MS is expected to be a muon, as other particles are stopped earlier in the detector [26].

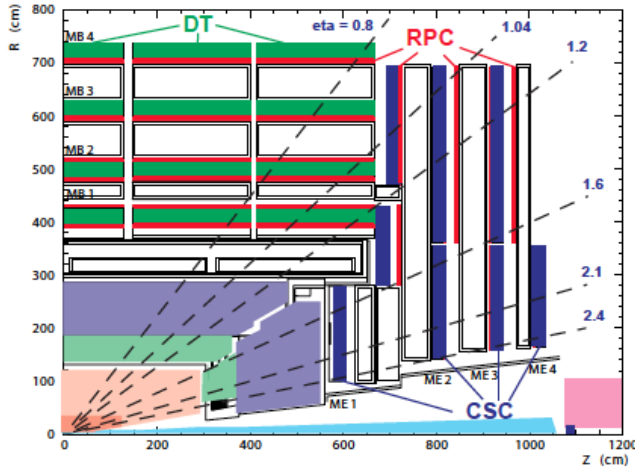


Figure 3.6: The Muon system shown in the $r - \theta$

Built within the iron yoke the MS shares the same structural layout, constructed in five barrel wheels, and two end-caps, together covering the region $|\eta| < 2.4$. As a large area must be covered, a silicon based setup such as the inner tracker would be too expensive, hence gaseous detectors are chosen. In the barrel region ($|\eta| < 1.2$) Drift Tubes (DT) are used, and in the end-caps ($0.9 < |\eta| < 2.4$) Cathode Strip Chambers (CSC) are preferred. While the DT and CSC detectors have a good position resolution, they have a long response time and are not suitable for use with the trigger, and so a third element is added in both regions, the Resistive Plate Chambers (RPC). The arrangement of the muon system is shown in Figure 3.6, with the locations of each type of detector shown.

In the barrel, the magnetic field is uniform, and therefore allows the use of Drift Tube chambers. Each of the five wheels are made up of 12 sectors, containing four chambers apiece, making up a full barrel of 240 chambers. The inner three chambers consist of three Super Layers (SL) using the first and third for the ϕ coordinate measurement and the second for the z coordinate. In the outer chamber, there are only two SL's and these contribute only to the ϕ measurement. Four layers of drift tubes make up a SL, and each layer is shifted by half a cell from the one beneath, to ensure any particle trajectory meets some active material. Each tube contains an anode wire and cathode strips, and is filled with a gas mixture of 85% Ar and 15% CO_2 gas. The Ar atoms are ionised by a

charged particle, and the resulting electrons and ions drift towards the anode and cathodes. Electrons reaching the wire are extremely excited by the high density field, which allows them to ionise further molecules, known as the "avalanche effect". Thus an electrical signal can be measured. The drift distance is 21mm and the drift time is limited to 380ns by the gas chosen, corresponding to 16 bunch crossings hence these are not suitable to provide accurate bunch information to the trigger.

Due to the aforementioned solenoidal magnetic field, the end-caps experience an irregular magnetic field, and a higher expected particle flux, and therefore drift tubes are not suitable. In this region 468 Cathode Strip Chambers are used, set out perpendicular in four stations in each end-cap. Trapezoidal chambers consist of seven radially oriented cathode strips, and in between six planes of azimuthal anode wires. The gas filling the gaps is made up of 40% Ar, 50% CO₂ and 10% CF₄, and the chambers work much in the same way as the DT's, with a high voltage applied to achieve the "avalanche effect". As the wires and strips are almost perpendicular its possible to make a simultaneous measurement in r and ϕ by identifying the charge fraction in several cathode strips.

In addition, a complimentary system of RPC's is installed in both the barrel and end-cap regions, providing extra information in the region $|\eta| < 1.6$. In the barrel there are 480 rectangular RPC's, with two layers per station, the inner two stations have one inside and one outside the DT's, and the outer two stations having both inside. The end-caps have overlapping trapezoidal chambers in the outer two concentric rings. These parallel-plate gaseous detectors have two thin gaps between plates, which are attached to high voltage to drive avalanche mode. The avalanche reaches the plates quickly, as the gas gaps have a small width, and so the measurement is made within ns, much smaller than the bunch crossing. The position resolution is adequate at the same time, and so the RPC's are used to contribute to the trigger, and also to map identified muons to a particular bunch crossing.

3.2.7 Trigger

When running at design luminosity, the LHC will collide protons with a bunch crossing of 25ns, each of which will result in 20 interactions corresponding to a rate of 40MHz of data, or 40 TB/second [27]. Not only is it impracticable for this

volume of data to be stored, but much of this corresponds to unwanted events, where no new particles have been produced, as the cross-sections for interesting physics processes are several magnitudes lower than the inelastic p-p cross section. Hence these events must be whittled into those which it is worthwhile to store and consider, which is done by the trigger system. This is divided into two components, the online hardware-based Level 1 Trigger (L1) to reduce the rate to that which can be routed from the buffer to the computing farm, and then the offline software-based High Level Trigger (HLT).

The L1 trigger is driven by the amount of time that data at the incoming rate that can be stored in the buffer, before needing to be overwritten. At design luminosity this is 128 bunch crossings, 3ns. Within this time the rate must be lowered to 10kHz, the acceptable rate for writing to the computing farm used for the HLT. This is accomplished using a tree system of triggers. First, the Regional Calorimeter Trigger (RCT) and Regional Muon Trigger (RMT) undergo local reconstruction of objects (muons, electrons, photons, jets). The Global Calorimeter Trigger (GCT) and the Global MUon Trigger (GMT) receive these objects, and sort them using a number of criteria e.g. Energy, momentum, quality of identification. The top four of each type are sent to the Global Trigger, which uses this information along with global event measurements such as total momentum to decide if the event passes an L1 Trigger requirement. If so it is sent to the HLT, if not it is not stored and passes out of the buffer.

The HLT essentially does the same thing as the L1 trigger, but is not driven by strict time requirements. Running on a large computer farm of multi-core computers, it has access to the entire readout data, and performs sophisticated calculations akin to those performed in physics analyses. Using partial reconstruction algorithms to clearly identify what objects are in an event, it is possible to filter according to a set of desired physics criteria. The desired rate to store to tape is 100Hz, and the HLT is designed and monitored constantly during data-taking to ensure the correct rate is achieved. In a given run a "menu" of different trigger paths is included, to select different types of event and with different thresholds. Some require the presence of a certain object, such as a Muon. Others combine requirements, and these are called Cross-Trigger. For example a family of triggers exist that require a certain HT and MHT. Within this family there are several different thresholds, which go down as low as can

be included in the menu without raising the rate prohibitively much. Thresholds that have a rate which is too high become "pre scaled".

Prescaled Triggers

If the rate of output of a given trigger becomes too high as the luminosity increases, the trigger will often remain in the menu with a lowered rate due to the inclusion of a "prescale factor" n . The trigger is known as "prescaled", as only 1 in n events that pass the trigger requirements will be included in the trigger output, thus reducing the efficiency of said trigger by the factor n .

For analysis search purposes this is undesirable as it would result in a significant loss of interesting events, but these pre scaled triggers can play a part in control samples and background estimates. In these areas it is suitable to multiply the yield by the prescale factor in order to provide an estimate of actual event numbers, whereas in the signal region it is essential to treat only physical yield measurements with an un-prescaled trigger.

Chapter 4

Event Reconstruction

The data stored directly from the CMS detector readout contains only the most basic level of information of a collision. As the particles created in the event pass through the detector they create signals at each point they interact, and these signals are locally reconstructed as a series of “hits”. This raw data is stored in CMS as the data format RAW. In order to undertake physics analyses the information is needed in terms of the four-vectors of particles. In order to interpret the raw data in terms of these physics objects a computational process known as object reconstruction is applied to the data. Using knowledge of the behaviour of each type of object and understanding of the detector, the objects are built from the hits, in such a way that optimises the efficiency for each type of object. Varying sets of requirements called “identification” or ID can then be applied to these objects at the analyses level to achieve the level of purity required.

The reconstruction of physics objects happens both within a sub-detector, and also by combining information from two or more sub detectors. The reconstruction is performed under the CMS Software framework (CMSSW) and the reconstructed data is stored in RECO format for use by individual analyses. The main focus of the analysis in this thesis requires well constructed jets and \cancel{E}_T , while electron, muon and photon objects are also required for vetoes and control samples.

4.1 Beamspot

The beamspot represents the locus of the region of beam collision in the detector, where the two bunches of protons meet. It is not an event-by-event measurement, but rather a property of a given physics run, measured over time. It is an important component of reconstruction, as it is used an estimate of the primary vertex, which is the position a given pair of protons interact to produce an event.

If the beamspot was at the origin of the CMS detector one would expect the distribution of the track closest approach angle ϕ_0 to be flat in the transverse impact parameter d_{xy} . If the beamspot is displaced this behaviour disappears, and thus for each run a fit is made on all available reconstructed tracks to regain this flat behaviour by adjusting the point that d_{xy} is with respect to, yielding the true beamspot.

4.2 Tracks

Whilst not a physics object in its own right, one of the most important elements of object reconstructions involves the identification of tracks left by charged particles in the inner tracker. There can then be used along with other sub detectors when reconstructing charged physics objects. In addition these tracks allow a precision identification of the vertex of interaction. In CMS an algorithm called the Combinatorial Track Finder (CTF) [28] is used to construct tracks from their representative hits.

The reconstruction of a track starts with the construction of a “seed”, an initial candidate track. It contains only a small subset of the available information from the tracker, but must be made up of at least 3 hits, or two hits and an additional beam constraint. The seed represents the initial estimate of the track’s trajectory, from which to collect its additional hits.

In order to achieve the best possible estimate, the seed is built from hits in the innermost area of the tracker, for three important reasons. Although in general the average occupancy decreases with r , the high-density nature of the pixel detector ensures the inner layer of pixel detectors has an occupancy lower than that of the outermost strip detectors. In addition, the pixel detectors give a better estimate of the trajectory due to their truly 2D measurements, and constructing them in the innermost layer minimises the material budget encountered, as not

all particles will reach the outer layers.

The next element of CTF is a pattern recognition module based on a Kalman Filter [29], that proceeds from the seed outwards and includes any additional hits associated with the basic estimated trajectory. As each new measurement is incorporated to the track the trajectory becomes more accurate. This proceeds for each track candidate in parallel, and where several hits are compatible several new candidates are created.

In order to safeguard against reconstructing one particle as more than one track, an ambiguity resolution mechanism is needed. Given any pair of track-candidates, the fraction of shared hits in the candidate with the fewest hits is examined, and if found to be greater than 50% this track is removed. If the number of hits is identical then that of the lower χ^2 remains while the other is removed.

Once all compatible hits have been incorporated the most accurate value of the track parameters can be extracted using a final fit. At this point any hits assigned to the track but otherwise not compatible with the track, based on the χ^2 of the expected residual, are deemed outliers and discarded before refitting. From the tracks selected, many will be fakes, known as “ghost” tracks, removed through a set of criteria based upon quality of fit (χ^2), the transverse and longitudinal impact parameters d_0 and d_z and the compatibility of the track with what is identified as the interaction vertex.

The fully CTF algorithm is used iteratively, starting with a pool of all hits identified in that event. After one iteration those hits that have been assigned to a track are removed from the pool, successful tracks are stored, and the process continues with the remaining hits. This process has 6 iterations, decided by the type of seed built. The first two are three-pixel seed and two-pixel seeds respectively, and pick up the high p_T tracks of an event. The second and third are also three and two pixel seeds, but with quality criterial loosened as most of the hits have been taken previously. The fifth and sixth iterations allow a seed to be built from strip detectors to include treks which are not covered by the pixel volume.

4.3 Vertex

The exact location of the initial p-p collision of a given event is not necessarily the same as the beamspot (although this can be used as a reasonable estimate) due to the unknown location of a given proton within the bunch. Known as the “primary interaction vertex”, this is reconstructed using the track collection. Prompt tracks are selected based on quality criteria such as the number of hits in each tracker sub-detector, the χ^2 of the fit and the transverse impact parameter. These are then clustered in z , and an adaptive vertex fit is used [30], where each track receives a weight between 0 and 1 due to its compatibility to the vertex common to the set of tracks [31].

4.4 Jets

The QCD property of confinement makes the treatment of partons in collider physics more complicated, as they hadronise once created and are not identified singularly. Additionally these primary hadrons can both emit gluons and decay and fragment into lighter hadrons. These decay products are all travelling in the same direction, as they have been “boosted” by the momentum of the primary hadron, so each of these groups of particles is called a “jet”. Physics analyses then make requirements on these jets, as opposed to specific requirement of quarks and gluons, where the “jet” concept in a perfect detector should represent the four-vector of the primary hadron. This is achieved through jet reconstruction where all information left in the detector from the decay products are assigned and added to a jet. As the products are moving under the same boost the jet can be thought to have a cone shape extending from the interaction vertex, where the radius of the cone is defined in the $\eta - \phi$ plane, $R = \sqrt{\Delta\eta^2 + \Delta\phi^2}$

At a hadron collider such as the LHC hadronic processes are abundant, and thus the method of defining and reconstructing these jets is crucial to and physics analyses. In CMS there are three types of reconstructed jets available, based on the sub-detectors used: Calorimeter Jets (CaloJets) use only the ECAL and HCAL, Jet Plus Tracks (JPT) Jets include also information from the tracker, and Particle Flow (PF) Jets use information from the whole detector whilst reconstructing all particles in parallel. The analysis in this thesis uses CaloJets, the reconstruction of which is discussed in more detail below.

The purpose of jet reconstruction is to group a set of boosted particles together, achieved by an algorithm that "clusters" the information from the calorimeters. The energy deposited in ECAL and HCAL cells are first combined into what are known as "calorimeter towers", consisting of one or more HCAL cells combined with the ECAL cells which geographically align to the HCAL cell. The tower energy is defined by the sum of cell energies passing an energy threshold to protect against electronic noise. Towers that fulfil the requirement of $E_T > 0.3\text{GeV}$ then form the input to the clustering algorithm used by CMS, anti- k_T [32].

4.4.1 The anti- k_T jet clustering method

Due to the expected levels of hadronic activity at the LHC, the jet clustering algorithm must be fast. In addition, it must be stable against the addition of soft particles, called "infra-red safe", as partons may emit soft gluons. It must also be "collinear safe", meaning it yields the same jets if a parton were to split into two collinear partons, so that they would both end up in the same jet. These two conditions are essential so that the experimental data may be compared to theoretical calculations regardless of the order they are performed at.

The anti- k_T clustering method [33] is a sequential recombination algorithm that fulfils these criteria [34], working pair-wise to combine nearby towers starting with those highest in p_T first. The decision of which order to combine pairs in is achieved with the use of two distance metrics, the distance d_{ij} between two towers i and j , and the distance d_{iB} between the i th tower and the beam. Considering all possible combinations of both metrics, the smallest is identified.

If this smallest value is the first case, the two towers i and j are combined into one prototype jet, whose position is weighted by the momenta of its parts. If it is the second case, the tower i is identified as a jet and removed from the list. This process is continued with the updated towers and prototype jets, until all towers have been combined. The definition of the metrics are seen in Equations 4.1 and 4.2 where $\Delta_{ij}^2 = (y_i - y_j)^2 + (\phi_i - \phi_j)^2$.

$$d_{ij} = \min(k_{ti}^{2p}, k_{tj}^{2p}) \frac{\Delta_{ij}^2}{R^2} \quad (4.1)$$

$$d_{iB} = k_{ti}^{2p} \quad (4.2)$$

Tower i has transverse momentum k_{ti} , rapidity y_i and azimuth ϕ_i . The variable R is analogous to the cone radius definition described above, and for this analysis $R = 0.5$. This general form of the metrics governs several types of jet algorithm of this family, differing in the value of power p . This is the parameter responsible for the relative importance of momenta and distance, and for anti- k_T $p = -1$ placing the importance on the momenta, and giving the “anti” in its name (after another variant, the k_T algorithm for which $p = +1$ [35]).

In this algorithm a hard particle creating a large energy deposit with no other hard deposits surrounding it will gather in the soft particle deposits. If another hard particle is found within $2R$ then the soft deposits are shared between them with weights relative to the hard particle momenta, unless they are within R of one another in which case they are identified as one jet.

The shape of the jet is defined alone by the cone about the hard particle, resulting in a perfectly conical jet except in the case where more than one hard particle exists within $2R$. If the two hard jets are within R or one another, the shape is either dominated by the hardest if there is a significant difference in the momenta, or if they are similar, defined by the total area covered by both cones. If the jets are not within R but within $2R$, there is not space for each jet to be conical, so either the hardest jet is conical and the softer is missing a piece, or if they have similar momenta each has a chunk missing with a boundary line down the middle of the shared area. Figure 4.1 shows in the $y\text{-}\phi$ plane jets reconstructed by anti- k_T for a sample event (generated by Herwig [36]) in which many soft deposits exist. Many coloured circular jet patterns are seen, representing conical jets, as well as the cases with close hard deposits demonstrating the shared and clipped jet area shapes.

Contamination from both pileup and underlying events can contribute soft energy deposits which may affect the momenta of jets reconstructed, the effect of which is known as the “back reaction”. One of the major advantages of the anti- k_T algorithm is that due to the relative importance of hard deposits over softer deposits this effect is suppressed, allowing more accurate measurement of jet momenta than other comparable models, leading to its selection by CMS.

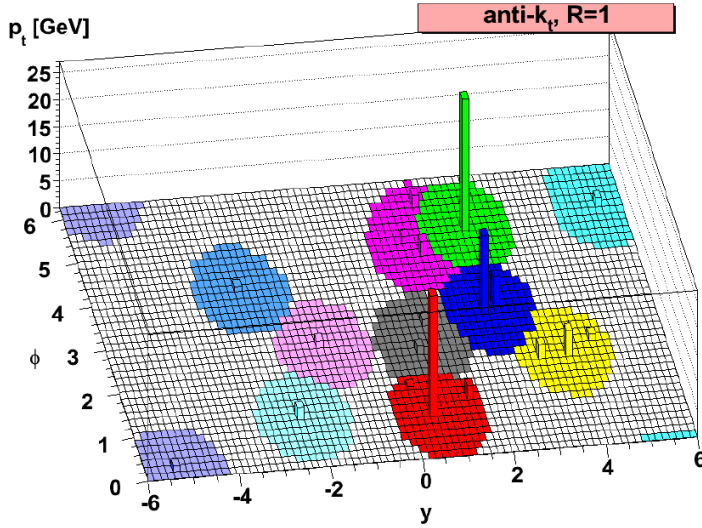


Figure 4.1: Illustration of the reconstructed jets for a sample Herwig generated event, with many soft deposits. Each coloured area represents the shape of the jet reconstructed, illustrating the trend to a conical nature of anti- k_T , and the behaviour of the algorithm where two hard deposits are close. Taken from [33].

4.4.2 Jet Energy Scale Corrections

The jets reconstructed in the detector using the method above typically have an energy that is different to that we would measure in a perfect situation. This is due to the nature of the response of the calorimeters, which is non-linear and non-uniform, as well as any residual effect contributed from pileup and underlying events (although this is small as mentioned above). For this reason, reconstructed jets must undergo energy corrections before they can be used in physics analyses.

The aim of these Jet Energy Scale (JES) corrections is to relate the energy measured in the detector to the energy of the underlying jet particles through knowledge of the detector response. There are three typical levels of correction

L1 - Offset An offset is subtracted to remove the energy contributions that are not associated with the event but rather from electronic noise and pileup events.

L2 - Relative Next the value is multiplied by a factor which is a function of a given pseudorapidity η to correct the relative differences in responses in different regions of the calorimeters.

L3 - Absolute Finally the value is multiplied by a second factor, which corrects the variable response to different jet p_T . The response to a given particle never returns the entire proportion of energy, and the percentage returned depends heavily on the momenta of the particle.

For the current dataset presented in this thesis, only L2 and L3 corrections were applied (L2L3), as L1 corrections deemed unnecessary due to low expected pileup rates at low luminosity. The combined L2L3 correction is performed using a combination of Monte Carlo calibration and corrections using data-driven methods. However crosschecks were made with the L1 offset included to ascertain validity of this assumption.

Initially an estimate of the correction is calculated with the help of Monte Carlo truth information, representing the major portion of the calibration. Here instead of separating the three levels, an all-together approach is used where relative and absolute are tackled simultaneously. Events generated by PYTHIA [37] are passed through the full CMS detector simulation GEANT 4 [38], in order to identify the reconstructed jets. In addition, full information for the real physical jet, known as a *generator* jet is retained. Each reconstructed jet is matched its own generator jet in the $\eta - \phi$ plane, making a requirement on the cone radius $R \geq 0.25$ to avoid mis-matching. A comparison of the momenta of the reconstructed jet and the generator jet allows a calibration factor to be extracted relative to the jet's η and ϕ .

Having calibrated the momenta using Monte-Carlo data-driven corrections of the relative and absolute calibrations are made. The relative correction is extracted using di-jet events balanced in p_T where one is detected in the central region, and the other may have any η value. The measurement of the second jet energy is compared to the well-defined measurement of the central region (chosen as the control region as it delivers the best performance for high p_T jets) in order to return the correction factor dependant on η . Having applied this correction, another is performed for the absolute using an events where a photon lies back to back with a jet. Comparing the momenta of the two gives an understanding of the distribution of the percentage of energy that has been included in a jet yielding the required factor.

With the application of the steps of calibration, the total energy of the particles within the jet has been recovered to an acceptable level required by

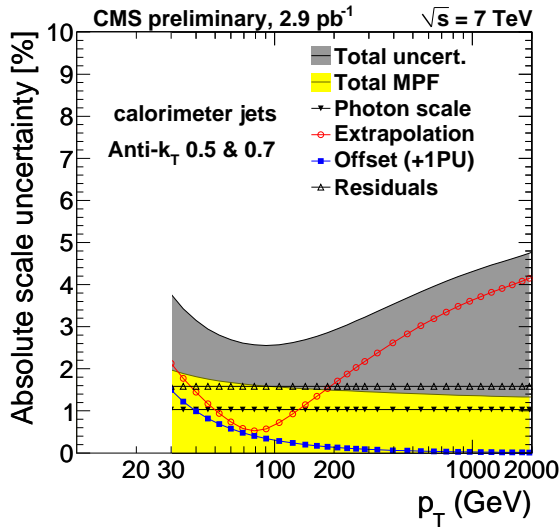


Figure 4.2: Total uncertainty (grey) of jet energy scale with respect to p_T after full L1L2L3 corrections applied for 2.9pb^{-1} of 7TeV data at CMS. Individual uncertainties of algorithm components shown also. Taken from [39].

the physics analyses of CMS. The full L1L2L3 corrections have a precision corresponding to an $3 - 6\%$ uncertainty of the jet energy scale (JES) for jet momenta ranging from 30 GeV up to 2TeV, as illustrated in first 7TeV collisions in Figure 4.2 [39].

4.5 Missing Energy

Alongside reconstruction of physics objects comes the calculation of “missing energy”, an important signal. In the Standard Model, neutrinos pass through the detector without interacting and therefore are responsible for energy “gone missing”, alone of the known particles. However in some New Physics models, most notably SUSY, there are suggestions of other more massive particles that would exhibit this signature.

As previously mentioned the LSP if it exists would not react, meaning its typical signature in a detector is that of energy gone undetected. This is observed as a momentum imbalance, or “missing energy” of the observed particles. In an ideally hermetic detector this would be a simple measurement through a vectorial sum of all existing energy deposits. However, even the best detector design cannot avoid the requirement of an opening through which the beams enter the detector,

and thus any particles moving toward this forward region may escape detection, thus spoiling the accuracy of the missing energy constraint.

Although these particles may have considerable momenta in the direction of the beam axis, in order to have an η outside the range of the calorimeters $-5 < \eta < 5$ its momentum transverse to the beam p_T must be less than $0.013E$ where E is its total energy. This ensures the transverse momentum lost to particles outside the acceptance is very small, thus an imbalance can indicate a particle leaving no deposit. The imbalance is referred to as *missing transverse energy*, \vec{E}_T , the magnitude of the 2D vector of missing p_T , which is written as \vec{E}_T . The reconstruction of these in CMS can occur in several ways, but the construction of calorimeter \vec{E}_T (caloMET) involves the summation of all n calorimeter towers in an event given in Equations 4.3 and 4.4 [40].

$$\vec{E}_T = - \sum_n E_n (\sin\theta_n \cos\phi_n \hat{\mathbf{i}} + \sin\theta_n \sin\phi_n \hat{\mathbf{j}}) \quad (4.3)$$

$$E_T = |\vec{E}_T| \quad (4.4)$$

4.5.1 \vec{E}_T Corrections

The energy deposits from the calorimeter towers summed are the uncorrected values, which like before in the jet reconstruction also require corrections, separated into two types. Type I corrections take into account the JES corrections described earlier in Section 4.4.2, as well as corrections to take care of muons and hadronic taus in an event. Type II accounts for effects from pile-up or underlying soft events.

Type I Corrections

The Type I corrections account for corrections associated with physics object measurements. Firstly, as the JES corrections for jets are relevant to the \vec{E}_T reconstruction also, a correction must be applied to bring \vec{E}_T in line with the true energy of the jets. The relevant correction described in Section 4.4.2 to each jet that has a corrected $p_T \geq 20\text{GeV}$ and an Electromagnetic Fraction (EMF) $i > 0.9$ is used to modify \vec{E}_T . The requirement on the EMF prevents applying the corrections in the case of an electron reconstructed as a jet, as this will have a

high fraction of electromagnetic energy.

The \cancel{E}_T measured in the calorimeters must be then corrected for any muon present, as a muon would pass through the calorimeter volume without depositing much of its energy. The information regarding a muon in the event is measured and reconstructed accurately using both the tracker and the muon system (see below). Having added any deposits the muon has made to the calorimeter to the $\vec{\cancel{E}}_T$ the p_T of the muon can then be subtracted to remove the effect of the missed muon on the \cancel{E}_T . This is done for each reconstructed muon that is reconstructed using both Muon algorithms (see Section 4.6) and passes a set of quality criteria. Among these cuts is a requirement on the isolation of the muon, as not all deposits in a non-isolated muon would be from the muon itself, and therefore would result in an over correction [41].

An additional correction is needed to account for the case of a tau that decays hadronically, as these tau-jets have differing characteristics from other jets. They are likely to have a low particle multiplicity where each product carries a significant energy, as opposed to the usual case of high-multiplicity soft products. In the region used for jet reconstruction $R \geq 0.5$ about the tau, $\vec{\cancel{E}}_T$ is summed, and the true energy of the tau removed from it in order to yield the correction necessary.

Type II Corrections

Having corrected all the hard jets this second step of corrections addresses the jets outside the type I acceptance and any energy deposits not clustered into jets, to remove the effects of underlying events and pile-up. This is obtained using a Monte Carlo control samples of events with a Z decay to two electrons, as characteristically the Z has low p_T and there is much unclustered energy. The sum of momenta of the towers unclustered into jets \vec{U} is obtained by taking the uncorrected E_T of an event, removing the momenta of the uncorrected jets and of the electrons. \vec{U} is then corrected using the Monte Carlo truth information [42].

4.5.2 Using Jets for Missing Energy - \cancel{H}_T

Another type of \cancel{E}_T reconstruction is possible, when the hadronic missing energy is created using the vectorial sum of the reconstructed jets of an event. This type is known as \cancel{H}_T , defined in Equation 4.5 where p_T^n is the transverse momentum

of the n th jet. In a hadronic event with no other standard physics objects other than jets is analogous to a \cancel{E}_T measurement, albeit relying only on the jet reconstruction.

$$\cancel{H}_T = \left| - \sum_n p_T^n \right| \quad (4.5)$$

The advantage of using \cancel{H}_T is that unclustered energy is automatically not a part of the sum, so automatically this variable is less sensitive to detector effects and pile-up than \cancel{E}_T , and therefore more robust, making it desirable for early measurements at the LHC. However through the same logic, it may fail to include real jets that are below the threshold, or unclustered energy that did belong to the event, factors which affect its resolution.

4.6 Muon

Muons are reconstructed in CMS by combining the information recorded in the muon systems with reconstructed tracks from the tracker. The small number of deposits made by muons in the calorimeter systems are not used in reconstruction although are used in muon identification criteria. The reconstruction of tracker tracks have been described already in Section 4.2.

In the muon chambers a local reconstruction occurs also, creating a *standalone muon track* [43]. Seeds are generated from track segments created by fitting adjacent hits within the layers of the DT or CSC detectors. As in the tracker, the seed suggests an initial estimate of the muon four-vector, and the fit is then extended to include segments from all the sub detector types, again using a Kalman Filter. Duplicates known as ghosts exist where one muon gives rise to more than one seed, thus tracks that share hits are compared and the best kept. Tracks are then constrained by the beam spot position within uncertainty in order to improve momentum measurement.

Once local reconstruction in the tracker and muon chapters is complete, they are passed to global muon reconstruction. There are two algorithms of muon reconstruction which are both used in parallel to create two type of candidate muons, depending on the direction of the extrapolation between tracker and muon systems.

Global Muons These muons are reconstructed from the “outside - in”. Starting

with a standalone muon, a match is made back to a reconstructed track before a fit is made to the combination. This works especially well for muons that carry high p_T , greater than 200 GeV, as within this limit the muon systems have greater resolution and thus are superior to the tracker information.

Tracker Muons These muons reconstructed from the “inside-out”. Here, all tracks of $p_T > 0.5$ GeV are treated as if they possibly came from muons. Each of these muon candidates is followed through to the muon system, allowing for possible energy losses and scattering. If any muon segment track is identified as a match, then the resulting track is considered a muon. As this only requires one single segment in the muon system this reconstruction method is most accurate for low momentum muons where the full volume of the muon system is not reached.

Providing they carry significant momentum muons in CMS collisions are mainly reconstructed as one of these types, and may often be reconstructed as both. However, about 1% of muons produce a standalone muon track only, and no matching tracker track is found. These are also retained.

The muon collection contains candidates from all three cases. Where the same track from the tracker has been involved in the reconstruction of both a Global and a Tracker muon, they are merged into one. The standalone muon tracks only included in the case where no other reconstruction used any of the muon segments. Combining the algorithms gives the best efficiency for the muon collection, and requirements of which to allow for analysis can be set later in Muon Identification criteria [44].

4.7 Photons

Photons are reconstructed solely with the information from the energy deposited in the ECAL. As a photon traverses the tracker material prior to the calorimeter system, photon conversions can occur. In addition, a primary electron travelling in the detector also loses energy through bremsstrahlung and corresponding photons are emitted tangentially to its curved trajectory. This leads to a characteristic energy pattern spread out in ϕ as the trail of photons is left but

narrow in η under the strong magnetic field. A clustering algorithm is therefore used to gather the energy from one primary particle into a SuperCluster (SC).

Different algorithms are required depending on the geometry - the “Hybrid” algorithm is used in the barrel, and the “Multi5x5” in the end-caps [45]. The Hybrid algorithm selects “dominoes”, strip-like collections of crystals in this $\eta - \phi$ geometry, whereas in the end-caps the structure is not arranged in $\eta - \phi$ and therefore Multi5x5 clusters each seed in a 5x5 crystal window, and allows combination with other overlapping 5x5 clusters.

Energy corrections must be applied to the SC to allow for detector effects in the calorimeter, typically at the 1% level. The weighted average of deposits in the SC determine the candidate location and the relationship between this and the primary vertex gives the direction. From the corrected SC’s photons are reconstructed providing the SC energy corresponds to energy in the HCAL of no more than 15% SC energy, and no matching track is found.

4.8 Electrons

The reconstruction of electrons in CMS combines the information from the energy deposits in the ECAL and the information from the tracker. This can be done both beginning with the ECAL and extrapolating to the tracker (ECAL-seeded) or vice versa (tracker-seeded). As the majority of isolated electrons can be reconstructed using the ECAL-seeded approach this is used for the veto in this analysis.

The reconstruction process begins by gathering compatible hits in the ECAL and combining them into a SuperCluster, the same described under Photon reconstruction. The algorithm responsible for generating electron superclusters takes advantage of this, combining individual hits into clusters, and then combining clusters within a narrow path in ϕ .

The tracker tracks left by electrons cannot be merely reconstructed using the method described above, as the high percentage of energy loss due to Bremsstrahlung makes the use of a Kalman Filter unsuitable, as the energy loss is non-Gaussian. Instead, a variant known as the Gaussian Sum Filter (GSF) [46] is more suitable, although slower. A supercluster is matched to a seed in the inner tracker, and the electron track reconstructed by extrapolation and fitted

with the GSF. As the GSF takes more processing power than the Kalman filter a pre-selection is applied to reduce the time taken, based on the compatibility of the track and supercluster in the $\eta - \phi$ plane [47].

Chapter 5

Searching for SUSY with α_T

The data collected by the CMS detector could hold signs of physics Beyond the Standard Model (BSM). In order to search for signs of new physics they must be distinguished from the vast quantity of Standard Model processes that will arise. Due to the nature of hadron collisions, a large background from QCD events is present, which poses challenges unlike the clean lepton colliders. The events one wishes to look for are termed “signal” events, and all others become part of the “background”. Search strategies are developed to optimise the selection of desired events whilst rejecting a large proportion of the unwanted “background” events. The validity of a search is tested using Monte Carlo simulations of both possible signal and expected background events, and is often evaluated by the proportion of signal S to background B, the S/B of a search.

This thesis focuses on searching for new physics inspired by almost all SUSY models. In this chapter we explore the nature of such new physics and the development of a new variable α_T which forms the backbone of a search for events with quarks and a large quantity of missing energy.

5.1 Inclusive SUSY Search

As previously discussed in Chapter 2, SUSY models that conserve R-Parity and therefore indicate new physics at the TeV scale introduce a candidate particle for dark matter. As this LSP cannot be observed due to its weakly interacting nature, searching for it is analogous to a search for large missing energy in particle collisions. In the CMS detector reconstruction of all visible particles allows us to

calculate the transverse component of this quantity, missing E_T or \cancel{E}_T .

As there are many models to describe the exact nature of SUSY due to the unknown mechanism of SUSY breaking, it is desirable to design an experimental search which does not rely on any one in particular, or even on the assumption of SUSY. These are called “inclusive” searches, and retain sensitivity to any new physics resulting in a new particle with the properties of a WIMP. The main feature is a requirement of a large quantity of \cancel{E}_T along with final state objects (hadronic jets, leptons, photons). The search space is then divided into channels via the final state objects required, in order to perform orthogonal searches to increase sensitivity and to allow combination

Discussion of SUSY on the whole and specific models such as mSUGRA are then used to quantify the reach of the search and to tune the cuts with Monte Carlo data. Where no new physics is found it can be useful to set limits on the parameters of such models, and in this thesis we will use mSUGRA for this purpose, along with test points in the mSUGRA phase space. However it is important to remember that the search itself remains open and sensitive to any WIMP candidate.

Physics at the LHC will suffer from high background rates, especially those from QCD, and the main goal of any analysis is selecting the new physics events required whilst removing the background from Standard Model processes. Missing energy can be observed in events in two ways, real missing energy from the production of weakly interacting particles, such as neutrinos and LSP’s, and fake missing energy which is a result of mismeasurement of objects, or missed objects.

Having noted that the generic signal produced by any such new physics model is a large amount of \cancel{E}_T , it might be assumed this forms the main variable to separate signal from background events. As \cancel{E}_T is measured in the calorimeters, it can be affected by miscalibration and noise in the detector, thus is not robust for early physics at the LHC.

To combat this issue there is also the quantity \cancel{H}_T which represents the vector sum of transverse momenta p_T of the jets in the system, giving the hadronic missing energy analogous to \cancel{E}_T in a hadronic search. However, there are limitations to the use of either of these quantities, as they are not robust to mismeasurements of the jets.

A background event with no missing energy may therefore be selected as having considerable E_T or H_T due to these mismeasurments, and thus it is natural to look for other variables which have a higher discriminatory power.

5.2 α_T in a di-jet system

The first step in devising a SUSY search strategy begins with the simplest of channels, the “dijet” search with just two jets and missing energy corresponding to two missing neutralinos. This channel is motivated by one of the cinematic scenarios of mSUGRA mentioned in Chapter 2, where the gluino is heavier than the squarks, therefore squarks are liable to decay directly to the LSP producing a quark jet. Due to the low multiplicity it is easy to understand kinematically the situation in play.

At the LHC the dominant background is from QCD diet events, produced with an extremely large cross section. These events do not actually produce E_T but can “fake” this signature through detector effects such as mismeasurement or missed objects. In addition there are a number of other backgrounds that produce real missing energy in electroweak interactions, $W + \text{jets}$, $t\bar{t}$ and $Z \rightarrow \nu\bar{\nu} + \text{jets}$, which we will refer to collectively as EWK. The greatest task on hand is to eliminate the dominating QCD background, which in a perfect detector could be easily achieved with a simple cut on E_T or H_T . However, due to the “fake” E_T signature from QCD events, a significant proportion of these events remain after such a cut, so it is desirable to devise a variable which can separate true sources of missing energy, and those arising from the detector.

In a QCD diet event, were it to be perfectly measured, the two jets are pair produced and following conservation laws must be back-to-back and of equal magnitude. In events with real missing energy, such as our potential SUSY signal, the jets have been produced independently of one another, and such rules do not govern them. The distribution of the azimuthal angle between the two jets, $\Delta\phi$, is therefore very different for the QCD background and potential signal events.

It is possible to exploit the nature of this further using a new variable proposed by Randall and Tucker-Smith, α , defined in Equation 5.1 [48].

$$\alpha = \frac{E_T^{j2}}{M_{inv}^{j1,j2}} \tag{5.1}$$

The E_T^{j2} is the transverse energy of the second jet (the lowest in energy) and $M_{inv}^{j1,j2}$ is the invariant mass of the dijet system. The design of this variable allows us to exploit the expected back-to-back nature of any dijet from QCD. A well-measured QCD event can only take values of $\alpha < 0.5$. In sharp contrast, a SUSY event can, due to the unseen neutralinos, produce jets in a similar direction with a low invariant mass giving rise to high values of α .

The transverse variant of this variable, given in Equation 5.1 makes use of the transverse mass M_T of the two jets as opposed to the invariant mass.

$$\alpha_T = \frac{E_T^{j2}}{M_T} \quad (5.2)$$

In this case a well-measured QCD event will have exactly 0.5. While both show equally strong power of background discrimination, α_T has greater signal retention for certain mSUGRA points,[49] and therefore is deemed comparable or superior. It is upon this variable that the search strategy is formed. The presence of the second jet energy in the numerator also gives rise to one of the most important properties of this variable, its resilience to jet mismeasurement. If there is a large mismeasurement of one of the jets, the order could be inverted. As a perfectly measured QCD event yields $\alpha_T = 0.5$, the cut chosen is $\alpha_T > 0.55$ in order to take into account the finite resolution of the jet energy measurement.

The explicit reliance of α_T on $\Delta\phi$ can be seen when the relationship is rewritten in the massless limit, in Equation 5.3. This relationship indicates a high correlation, and thus a cut on α_T renders a further cut on $\Delta\phi$ negligible[50].

$$\alpha_T = \frac{\sqrt{E_T^{j2}/E_T^{j1}}}{2(1 - \cos\Delta\phi)} \quad (5.3)$$

5.3 α_T in a n-jet system

More complicated decay processes result in hadronic signatures with more than two jets, generalised to the n-jet system, for example where a gluino-squark pair decay to produce three quarks and two LSP's. In order to increase phase space the dijet search channel may be extended to a final state including N jets and considerable \cancel{E}_T , where $N \geq 2$. This is colloquially known as the all-hadronic search channel as it comprises any fully-hadronic decay modes that might yield

possible SUSY signal.

Following the success of the construction of the α_T variable in the dijet topology, the variable was extended to a general form applicable for an n-jet system, thus incorporating the full hadronic SUSY search channel[51]. This is undertaken by modelling the system of n jets as though it were a dijet system, through the mathematical construction of two pseudo jets. Thus α_T can be calculated using the properties of the pseudo jets.

The two pseudo-jets are built by merging the n jets present in two sets with a vectorial sum deciding the direction, and a length equal to the sum of the magnitudes of the composite jets. The combinations chosen to assign n jets into 2 pseudo jets is done such that they are as balanced as possible, i.e. the difference in H_T , ΔH_T is at a minimum. All combinations are therefore considered, and the one which satisfies this condition is chosen. With this psedo-dijet system we can construct a formalism for α_T that uses the basic kinematic variables of the system in Equation 5.4.

$$\alpha_T = \frac{1}{2} \frac{(H_T - \Delta H_T)}{\sqrt{H_T^2 - |\not{H}_T|^2}} = \frac{1}{2} \frac{1 - \Delta H_T/H_T}{\sqrt{1 - (\not{H}_T/H_T)^2}} \quad (5.4)$$

The second form of the definition shows its dependence on the ratios of ΔH_T and \not{H}_T to the events H_T . In a well measured QCD event there is no \not{H}_T , and $\Delta H_T/H_T < 1/3$, from which the maximal value comes from the rare “Mercedes Star” QCD event with three jets of equal mass and momenta with the $\Delta\phi$ between any chosen two being equal. Therefore with an ideal detector QCD events have $0.333 < \alpha_T < 0.5$, but large mismeasurement leads to a high \not{H}_T which can higher the values of α_T . The chosen cut value of $\alpha_T > 0.55$ corresponds to a missing energy fraction $\not{H}_T/H_T > 0.4$, and as this occurs in QCD events the ratio $\Delta H_T/H_T$ is liable to increase also. This relationship prevents α_T for QCD events from significantly exceeding 0.5 unless an object of sizeable momentum were missed altogether in the calculation.

It has been shown that whilst the sharp cut-off for QCD events at $\alpha_T = 0.5$ becomes less distinct, it is still pronounced and thus retains the powerful background rejection properties desired[52]. Performance tests with smeared jet energies shows the α_T variable applied to a multi-jet analysis is robust to jet mismeasurement, and superior in this area to a standard \not{E}_T analysis. The jet energy scale does not directly affect α_T but its resolution improves for increasing

H_T , as demonstrated with 7 TeV data in Reference [53].

5.4 Defining the ratio R_{α_T}

The proportion of SUSY signal to background differs greatly with the H_T of the event, with background processes dominating at low values while SUSY becomes more prominent for high H_T . In order to investigate this behaviour a new variable R_{α_T} is defined in Equation 5.5 as the ratio of events passing the cut $\alpha_T > X$ with those that fail it, where X is normally 0.55.

$$R_{\alpha_T}(X) = \frac{N(\alpha_T > X)}{N(\alpha_T < X)} \quad (5.5)$$

The relationship of this variable with H_T that can then be studied for background processes and potential SUSY signal using Monte Carlo samples. Where QCD events with no real missing energy dominate the numerator, tightening the H_T cut results in a decreasing R_{α_T} . If the QCD background is negligible due to a successful α_T cut, the now-dominating electroweak backgrounds contribute some real missing energy in the form of neutrinos and exhibit a flat relationship with H_T . However, in the presence of an mSUGRA SUSY signal in the numerator an increase of H_T corresponds to an increasing R_{α_T} . These three distinctive behaviours provide a strong search strategy using R_{α_T} in exclusive bins of H_T . These trends have been shown to be robust to jet mismeasurements, or even when 1 jet in 25 is not included in the calculation [53]

5.5 Extending α_T for single-lepton searches

A cleaner SUSY signature can be obtained through the single lepton channel, where the topology identical save the extra requirement that there be one muon or electron in the final state. In addition, requiring a lepton can provide a useful control sample for the hadronic search. Hence it is interesting to develop the α_T search to apply to this channel, especially where the lepton p_T is low and hence the dominant background is from fake leptons in QCD events.

In this case, in the final state there is one lepton, and n jets where n is at least two. Production mechanisms for one lepton and two jets in SUSY decay modes at the LHC are similar to those of the 3-jet hadronic channel. Thus it is possible

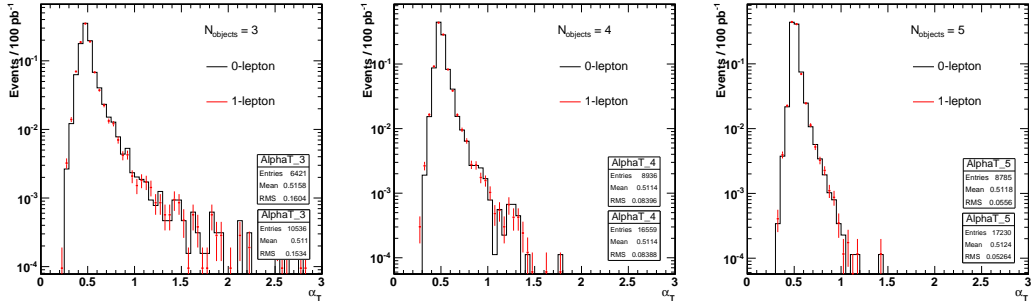


Figure 5.1: The shape of the α_T distributions for object multiplicity N for the N -jet channel (0-lepton) and the $N-1$ jet plus 1 lepton channel superimposed. From left to right the object multiplicities shown are $N=3$, $N=4$, $N=5$.

to draw parallels, and describe the system as an n-object system. Here, an n-jet hadronic event is treated the same as that which has 1 lepton and $n-1$ jets. The quantities in the definition of α_T are extended to include the lepton as if it were a jet, such that the lepton is included in the building of the two pseudo-jets.

The validity of this approach can be seen in Figure 5.1 where the hadronic (0-lepton) and single leptonic (1-lepton) cases are shown superimposed for the SUSY test point LM0, for three different object multiplicities 3, 4 and 5[54]. As can be seen, although the shape of the α_T distributions change with the object multiplicity, there is a good agreement between the n jet system and the n-1 jet plus lepton system.

5.6 Reliance of α_T on jet object definition

As mentioned above, although α_T is robust to mismeasurements a large value can be obtained from a QCD event if significant objects are not included in the measurement. To remain within the capabilities of the detector and reconstruction algorithms, the definition of a jet for the purpose of analysis requires the passing of a certain jet energy threshold. As this value is relatively small compared to the total H_T of an event, it should not contribute a large mismeasurement effect to the α_T variable. However there might be some cases for high jet multiplicities where a large number of low-energy jets just below the threshold are not considered, and so the α_T value is skewed. Hence, to remove this effect it is possible to make a cut in the ratio of the missing energy estimated

from jets H_T and that measured by the calorimeter systems \cancel{E}_T so that an event with $R_{miss} > 1.25$ is rejected.

Chapter 6

Searching for Supersymmetry with α_T in all-hadronic events

The analysis presented here represents a model-independent search for new physics in the all-hadronic channel, where the final state is defined by the presence of jets and missing energy. Designed to search for signs of supersymmetry whilst remaining sensitive to other new physics models, an inclusive strategy is used imposing restrictions only on the final state. Events are chosen based on their compatibility with a topology of heavy new particles pair-produced in p-p collisions, which decay through a chain with an end product which is stable and undetectable.

Isolating these new physics events from Standard Model background processes is essential in order to identify an excess. Controlling the dominant background from QCD Multijet processed is the central feature of the strategy, implementing use of the powerful discriminant, the α_T variable described in Chapter 5. The remaining backgrounds from electroweak processes may then be accounted for using data-driven estimation techniques in muon and photon control samples. The analysis presented here was done in 2011 and uses 1.1fb^{-1} data, representing an update on the previous iteration of this analysis using 35pb^{-1} 2010 data, which will be periodically referred to and is fully documented at [55].

6.1 Samples

This analysis uses datasets both from Monte Carlo simulation (MC) and of data recorded by the CMS detector in 2011.

6.1.1 Monte Carlo Simulation

Datasets of simulated events with calculated cross-sections are required for any analysis at the LHC. The following samples are used, full details of which can be found in Appendix A.

Standard Model Background

- QCD Multijet
- $W + \text{jets}$
- $Z \rightarrow \nu\bar{\nu} + \text{jets}$
- $t\bar{t} + \text{jets}$
- $\gamma + \text{jets}$

CMSSM SUSY Signal

For the purpose of understanding the possible yields from CMSSM SUSY, two mSUGRA parameter points are used. CMS has a dedicated set of 10 Low Mass(LM) points designed for initial data-taking from which we have chosen LM4 and LM6, the values of which are found in Table 6.1.

mSUGRA Point	m_0	$m_{1/2}$	A_0	$\tan \beta$	$\text{sign}(\mu)$
LM4	210 GeV	285 GeV	0	10	+
LM6	85 GeV	400 GeV	0	10	+

Table 6.1: The two CMSSM SUSY signal points used and their corresponding mSUGRA parameter values.

These points are chosen for their existence above the exclusion limit set previously, shown in Figure 6.1 on the exclusion plot from the 2010 iteration of this analysis[55].

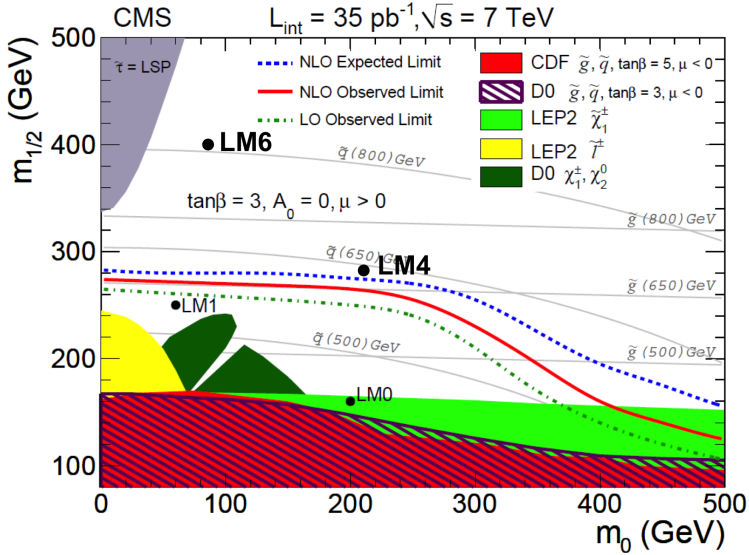


Figure 6.1: The exclusion limit set in the previous incarnation of this analysis with the 35pb^{-1} 2010 CMS dataset shown in the $m_0 - m_{1/2}$ plane with $\tan \beta = 10$, $A_0 = 0$ and $\text{sign}(\mu) = +$. Reference points LM4 and LM6 to be used in the 2011 analysis are illustrated, in the region yet to be excluded. Previously used reference points LM0 and LM1 are shown below the limit already excluded [55].

6.1.2 Data Sample

This analysis considers data collected by CMS at $\sqrt{s} = 7$ TeV in 2011 between March and June, during the data-taking period known locally as Run2011A. Analyses use only the data taken whilst CMS was fully operational, and thus the data used were specified by the certified list of “good runs” that correspond to $1.1 \pm 0.05 \text{ fb}^{-1}$ of integrated luminosity [56].

As described previously, loose requirements on the types of triggers passed allow the sorting of the data into each Primary Dataset (PD). For the hadronic analysis the HT dataset is used, with basic low-threshold H_T triggers required. Higher threshold triggers are applied subsequently as part of the analysis selection, detailed in Section 6.3.

For the data-driven estimation techniques muon and photon control samples are defined. For the muon control sample, the HT PD is also used, as a low muon p_T requirement makes this better suited than the dedicated Muon PD. However the photon control sample uses the dedicated Photon PD that requires some basic threshold photon triggers to be passed. The photon control sample had slightly

lower statistics available (1.06 fb^{-1}) and henceforth a correction factor is applied to yields from this control sample to normalise to the signal region.

6.2 Analysis Framework

For the purpose of the analysis private ntuples are generated fro the RECO samples using the CMSSW framework and CMS’s Physics Analysis Toolkit (PAT), retaining all variables from the intermediate step of PAT-tuples recommended by the CMS SUSY group. Following this private code is used on the ntuples to perform the analysis.

6.3 Trigger

In order to select the signal events and minimise the contamination from backgrounds, a set of selection criteria is applied. As described previously in Section 3.2.7, data collected by the CMS detector is stored and organised according to the L1 and HLT trigger paths passed. While the datasets chosen in Section 6.1.2 have some basic level trigger requirements, we also require a more stringent set of requirements.

In the previous iteration of this analysis for the 2010 dataset, a set of pure H_T triggers was used. However these are unsuitable for the 2011 analysis as due to the increase in instantaneous luminosity the rate of triggers with desirable thresholds have become too high and become prescaled, rendering them unsuitable for the signal selection, although they will play a part in the control region. Moving to higher H_T thresholds is also undesirable as it would reduce a significant portion of the search region.

The use of cross-object triggers is now employed, requiring events that pass thresholds in both H_T and \cancel{H}_T for the signal region. As the era of data-taking progressed there were several menu-changes, during which time we required the lowest un-prescaled thresholds available at a given time to ensure signal yields are accurate, some of which are implemented in the menu under different versions, the relevant paths appended with `_v*`.

The first set of runs in the 2011 dataset correspond to a trigger used with thresholds in $[H_T, \cancel{H}_T] = [260, 60]$ GeV. After this the CMS standard thresholds

were shifted down by 10 GeV, relevant for the major portion of data taking. For all runs henceforth the lowest unprescaled cross-trigger had an H_T threshold of 250 GeV, during which time the \cancel{H}_T thresholds of the lowest unprescaled evolve through 60, 70 and 90 GeV.

HLT Trigger Path
HLT_HT260_MHT60_v2
HLT_HT250_MHT60_v2
HLT_HT250_MHT60_v3
HLT_HT250_MHT60_v4
HLT_HT250_MHT70_v1
HLT_HT250_MHT70_v3
HLT_HT250_MHT70_v4
HLT_HT250_MHT90_v1

Table 6.2: List of HLT trigger paths for the signal selection from which the lowest unprescaled was used or any given run.

The quantities H_T and \cancel{H}_T used in the trigger requirements differ from those used in the analysis. The trigger uses jets built in online reconstruction with uncorrected energy to form these quantities, whereas those quantities in our analysis use only jets passing the object requirements and with corrected energy. Thus it is not the case that an H_T trigger of threshold X is efficient for events with $H_T \gtrless X$ in the analysis. It is necessary to ensure the trigger is efficient with regard to analysis cuts in both H_T and \cancel{H}_T .

In this two step process, the efficiencies of pure H_T triggers of thresholds 250 and 260 are identified through comparison to an orthogonal sample, using a Muon H_T cross trigger. These triggers can be considered 100% efficient by an offline H_T cut of 275 GeV, and thus this is selected for the analysis. Having made this cut the efficiency of the \cancel{H}_T part may be tested, with reference to α_T (which is analogous to a cut on MHT). In the lowest bin of the analysis, $275 < H_T < 325$ GeV a small inefficiency was measured of $0.99_{-0.02}^{+0.01}$, and in all other bins $H_T > 325$ the analysis is measured as fully efficient - $1.0_{-0.03}^{+0.00}$.

This analysis makes use of those events which fail the α_T selection criteria also, as the hadronic bulk control sample. In this region the chosen signal triggers would not be efficient as we wish to use the events with low \cancel{H}_T which would not

pass that element of the trigger requirement. Here the pre-scaled H_T triggers are suitable for use, taking into account the prescale factors to gain yields in this bulk sample, an approach which is suitable due to the high statistics from QCD events. The lowest prescale of the trigger thresholds chosen for each H_T bin, shown in Table 6.3, are used at each point in the evolution of the trigger menu.

Analysis H_T Region	HLT Trigger Paths
$275 < H_T < 325$	HLT-HT250_v*, HLT-HT260_v*
$325 < H_T < 375$	HLT-HT300_v*
$375 < H_T < 475$	HLT-HT300_v*, HLT-HT350_v*
$475 < H_T < 575$	HLT-HT440_v*, HLT-HT450_v*
$H_T > 575$	HLT-HT520_v*, HLT-HT550_v*

Table 6.3: The prescaled HLT trigger paths used for each H_T region of the hadronic control sample, where $\alpha_T < 0.55$. N.B. The H_T that defines the region is built from jets with corrected energy that pass the requirements of the analysis, while the H_T quoted in the trigger definition is uncorrected and built using online reconstruction jets available to the trigger.

In the muon control sample, due to the low $p_T^\mu = 10$ GeV threshold we use the same triggers as for the hadronic signal sample. The photon sample makes use of the single photon trigger paths shown in Table 6.4, using the lowest unprescaled threshold available for each given run in the data.

HLT Trigger Paths
HLT_Photon75_CaloIdVL
HLT_Photon75_CaloIdVL_IsoL
HLT_Photon90_CaloIdVL
HLT_Photon90_CaloIdVL_IsoL

Table 6.4: The list of HLT trigger paths available used to select the events for the Photon Control sample from which the lowest unprescaled photon threshold is selected in any given run.

Events passing the relevant triggers proceed into the analysis selection.

6.4 Object Definitions

6.4.1 Good Event Definition

In order for an event to be considered suitable for use in physics analyses, it must be defined as a “Good Event”. Such an event is required to have at least one non-fake good primary vertex with $N_{dof} > 4$. Constraints on the vertex position along the beam axis $|z_{vtx}| < 24$ cm and perpendicular to the axis of $\rho < 2$ cm must be satisfied. Events that have many fake tracks are identified as monster events and removed, by requiring that the ratio of High Purity tracks to the total number be greater than 25% in events with more than 9 tracks.

6.4.2 Jets

The jets used in this analysis are Calo Jets, reconstructed as described in Section 4.4 using the anti- k_T jet clustering algorithm. In addition, a reconstructed jet must pass an additional selection in order to be considered for the analysis:

- Corrected jet transverse momentum requirement of $p_T > 50$ GeV
- Jet pseudo-rapidity $|\eta| < 3$ required to ensure within the fiducial range of the calorimeter systems.
- Passes “loose” jet identification criteria to reject jets resulting from unphysical energy using cuts in Table 6.5.

Any jet which passes the E_T and η requirements but fails the “loose” identification criteria is noted, and the event is marked as containing an “odd” jet, as the presence of such a particle reflects an event whose kinematics are poorly understood and may therefore lead to a misleading \cancel{H}_T .

6.4.3 H_T and \cancel{H}_T

The calculation of both H_T and \cancel{H}_T is performed using only the jets selected by the selection above in Section 6.4.2.

Definition	Variable	Cut
Fraction of jet energy contributed by the “hottest” hybrid photo-diode	f_{HPD}	< 0.98
Minimum number of cells required to contribute 90% of the jet energy	N_{cells}^{90}	≤ 2
Fraction of jet energy contributed by deposits in ECAL	f_{EM}	> 0.01
Balance of the energy measured in the short(E_S) and long(E_L) HF fibers.	$R_{HF} = \frac{(E_S - E_L)}{(E_S + E_L)}$ (if $p_T^{jet} > 80$ GeV)	$R_{HF} > -0.9$ $(-0.9 < R_{HF} < 1)$

Table 6.5: Set of cuts applied in “loose” CaloJet ID used to reject jets resulting from fake calorimeter deposits representing unphysical energy. Devised using cosmic run data as a pure sample of non-collider “fake” jets, full details of which can be found in [57]

6.4.4 Muons

Although muons are not required by the analysis, a veto on them must be employed, based on muons that satisfy the following set of criteria:

- $p_T^\mu > 10$ GeV
- $|\eta| < 2.5$
- Relative Combined Isolation = $(Iso_{tracker} + Iso_{ECAL} + Iso_{HCAL})/p_T^\mu < 0.15^1$
- Passes “tight” muon identification, using cuts shown in Table 6.6.

6.4.5 Electrons

Similarly electrons are also defined for veto purposes, with the definition of an electron in the analysis as that passing the following cuts:

- $E_T^e > 10$ GeV
- $|\eta| < 2.5$

¹The components $Iso_{tracker}$ (Iso_{ECAL} , Iso_{HCAL}) represent the sum of $p_T(E_T)$ in the relevant detector component, calculated in a cone of $R = 0.3$ in $\eta - \phi$ around the muon trajectory. The track hits used to reconstruct the muon are not used and any muon deposit in the calorimeters is removed via a smaller veto cone.

Definition	Variable	Cut
Reconstructed with outside-in algorithm	Global Muon	Required
Reconstructed with inside-out algorithm	Tracker Muon	Required
Global muon track fit quality	χ^2	< 10
Number of hits in the silicon tracker included in track	N_{trk}^{hits}	> 10
Number of pixel hits in N_{trk}^{hits}	N_{pixel}^{hits}	> 0
Number of hits in muon system included in Global Muon	N_{muon}^{hits}	≥ 1
Transverse impact parameter with respect to vertex	d_{xy}	$< 2 \text{ mm}$

Table 6.6: Set of cuts applied in “tight” Muon ID, taken from [58]

- Combined Isolation = $(\sum_{\text{tracker}} p_T + \sum_{ECAL} E_T + \sum_{HCAL} E_T)/p_T^e < 0.15$
- Pass WP95 electron identification implemented using cuts in Table 6.7.

Definition	Variable	Barrel Cut	End-Cap Cut
RMS of the width in η of the crystals about the most energetic crystal in the seed	$\sigma_{inj\eta}$	< 0.01	< 0.03
Difference in ϕ between track and supercluster	$\Delta\phi_{vtx}$	< 0.8	< 0.7
Difference in η between track and supercluster	$\Delta\eta_{vtx}$	< 0.007	< 0.01
Ratio of HCAL energy in $\Delta R = 0.15$ to ECAL seed energy	H / E	< 0.15	< 0.07

Table 6.7: Set of cuts applied in “WP95” Electron ID, taken from [59] corresponding to an intended 95% efficiency for signal electrons in W events for electrons with $p_T > 20 \text{ GeV}$.

6.4.6 Photons

Photons in the analysis are defined by the following set of requirements:

¹where electron $p_T > 20 \text{ GeV}$, measured with a sample of $W \rightarrow e$ events.

- $p_T^\gamma > 25 \text{ GeV}$
- $|\eta| < 2.5$
- Passes “tight” photon cut-based identification (including isolation) using cuts shown in Table 6.8.

Definition	Variable	Barrel Cut	End-Cap Cut
Tracker Isolation in a cone of R=0.4	Iso_{trk}	$< (2.0GeV + 0.001E_T^\gamma)$	
ECAL Isolation in an outer cone of R=0.4 (inner cone R=0.06 removed).	Iso_{ECAL}	$< (4.2GeV + 0.006E_T^\gamma)$	
HCAL Isolation in an outer cone of R=0.4 (inner cone R=0.15 removed).	Iso_{HCAL}	$< (2.2GeV + 0.0025E_T^\gamma)$	
RMS of the width in η of the crystals about the most energetic crystal in the seed	$\sigma_{inj\eta}$	< 0.013	< 0.030
Ratio of HCAL energy in $\Delta R = 0.15$ to ECAL seed energy	H / E	< 0.05	< 0.05

Table 6.8: Set of cuts applied in “tight” Photon ID, taken from [60]

6.5 Pre-Selection

A basic selection of events used for comparison of distributions between data and monte-carlo events shall be known as ”pre-selection”, following the details set out in this section.

HCAL Barrel and End-cap (HBHE) Noise Filter Events where noise has been identified in the HCAL are removed also, using an algorithm which checks for Photodetectors which have at least 17 out of 18 channels with an $E > 1.5 \text{ GeV}$.

Following these conditions events are then selected by the following criteria, using the definitions of physics objects according to the criteria stated previously:

- Pass triggers as detailed in Section 6.3.
- Pass Good Event selection as detailed in Section 6.4.1.

- Require events with $N_{jet} \geq 2$
- $N_{muon} = N_{electron} = 0$ to reduce the effects of missing energy from neutrinos.
- $N_{photon} = 0$ to ensure a pure hadronic set of events.
- Events with > 0 “odd” jets are vetoed.
- Additional constraint on the transverse momentum of the two leading jets $p_T^{j1}, p_T^{j2} > 100$ GeV.
- Additional constraint on the leading jet pseudorapidity $|\eta^{j1}| < 2.5$.
- $H_T \geq 275$ GeV

6.6 Final Signal Selection

After the preselection a final set of cuts is applied, including the α_T cut that defines the signal region alongside cleaning cuts which remove events that may lead to inaccurate results.

- $\alpha_T > 0.55$
- If the ratio $R_{miss} = \cancel{H}_T / \cancel{E}_T > 1.25$, the event is rejected. This protect the quantity α_T from the scenario where many jets fail the $p_T = 50$ GeV threshold thus resulting in fake \cancel{H}_T and thus misleading values of α_T .
- To prevent against fake missing energy resulting from dead or masked cells in the ECAL or the gap between the barrel and end-caps the following procedure is used: The jet most likely to be responsible for the \cancel{H}_T is found. If the angle ϕ between this jet and the vector $\vec{\cancel{H}}_T$ (known as $\Delta\phi^*$) less than 0.5 then the $\eta - \phi$ distance between the jet and the nearest masked ECAL cell is computed, along with the distance from the detector gap. If either distance is smaller than 0.3 then the event is rejected.

6.7 An H_T Shape Analysis

Previous iterations of this analysis strategy with the 35pb^{-1} 2010 LHC dataset [55] used a cut-and-count strategy for all events passing the selection, defining the

signal region by an $H_T > 375$ and using lower regions in H_T as control regions. The 2011 analysis follows the same selection but motivated by the increasing luminosity is undertaken as a Shape Analysis in bins of H_T , using the whole range $H_T > 275$ GeV as a signal region. This allows greater sensitivity to states of higher mass.

The set of lower bin edges are as follows: [275,325,375,475,574,675,775,875], where each bin is exclusive with an upper limit corresponding to the lower edge of the next bin, except in the case of the final bin which is inclusive $H_T > 875$. The background estimation techniques employed from data therefore are designed to identify the contribution in each distinct bin.

In order to include the two lowest bins in H_T it is necessary to scale the jet thresholds stated in Section 6.5 in order to maintain even event kinematics allowing a shape analysis approach. The background from $t\bar{t} + \text{jets}$ carries a bias to higher jet multiplicities compared to the other EWK components, and thus with identical jet definitions exhibits a turn on behaviour in H_T . In order to remedy this, the lowest two bins have both the p_T threshold required by definition and the additional second jet p_T requirement scaled. The scale factor is $l/375$, where l represents the bin lower edge in question, leading to the thresholds shown in Table 6.9.

H_T Region	Jet Definition	Second-Leading Jet Cut
$275 < H_T < 325$	$p_T > 36.7$ GeV	$p_T^{j1}, p_T^{j2} > 73.3$ GeV
$325 < H_T < 375$	$p_T > 43.3$ GeV	$p_T^{j1}, p_T^{j2} > 86.7$ GeV
$H_T > 375$	$p_T > 50$ GeV	$p_T^{j1}, p_T^{j2} > 100$ GeV

Table 6.9: The three different regions of jet scaling, with values indicated both for the basic definition of a jet used in the analysis, and the second-to-leading jet energy cut. The former is especially important as this alters the value of H_T as this is calculated using the jets in the event.

6.8 Hadronic Signal Region Results

6.8.1 Data to Monte-Carlo Comparisons

Distributions of the 2011 data with MC samples alongside are shown in this section. The MC samples are normalised to 1.1fb^{-1} for shape comparison and

to illustrate the accuracy of modelling provided, although these are not used in background estimation as data control samples are used later.

In Figure 6.2 distributions of H_T and the jet multiplicity (NJet) are shown for events that pass the pre-selection with an additional cut of $\cancel{H}_T > 100$ GeV to ensure trigger efficiency. For simplicity only bins with $H_T > 375$ GeV have been included in the plots, so as to maintain one set of jet thresholds. There is good agreement in both cases variables, with no noticeable shape disagreement. Using events with the same selection, Figure 6.3(a) shows the high discriminatory power of the α_T variable between the QCD “fake” \cancel{E}_T background and signal events with real \cancel{E}_T . The region $0.46 < \alpha_T < 0.6$ is expanded in Figure 6.3(b), illustrating the rapid QCD fall-off to zero that motivates the chosen cut value of 0.55.

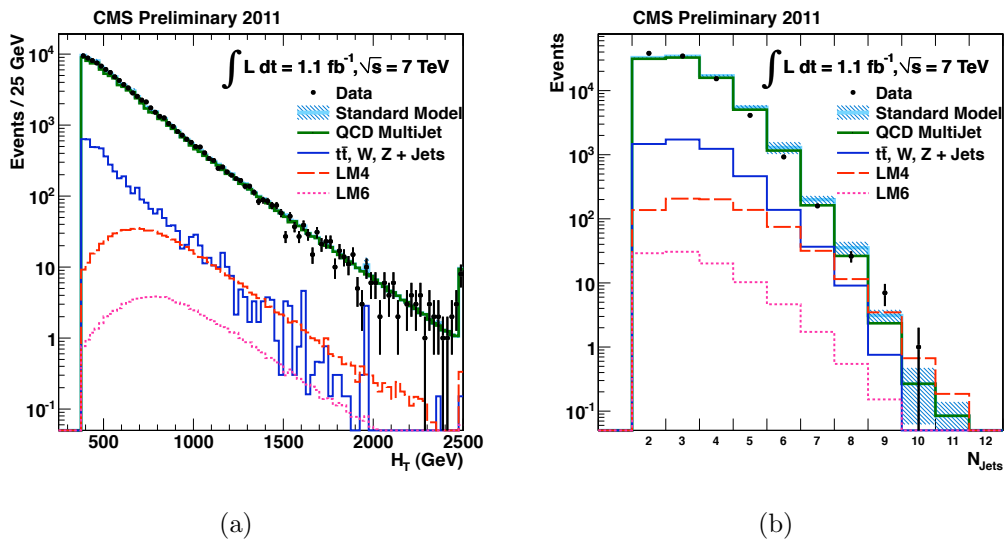


Figure 6.2: Distributions of (a) H_T , (b) N_{Jet} , showing comparisons of 1.1 fb^{-1} 2011 7 TeV CMS Data and equivalently weighted Monte-Carlo prior to the α_T selection cut, for $H_T \geq 375$ GeV and $\cancel{H}_T > 100$ GeV. SUSY Signal reference points LM4 & LM6 shown for illustration of potential yields.

The distributions of jet multiplicity, $\Delta\phi^*$ and M_{eff} after the final selection cuts are applied can be seen respectively in Figure 6.4. Data shows a good overall comparison to the Standard Model MC, although here statistics are more limited accounting for fluctuations. The $\Delta\phi^*$ distribution in Figure 6.4(c) is consistent with the expectation that the α_T cut completely eradicate contamination from QCD events, as any evidence of such would lead to a peak at low values, instead of the flat behaviour seen. In addition no notable excess can be seen of data

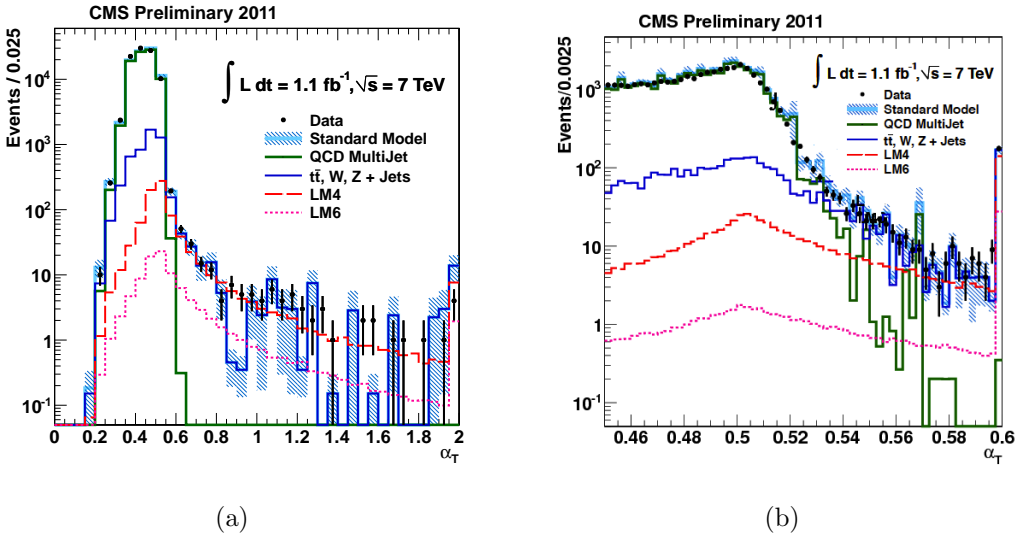


Figure 6.3: Distributions of α_T showing comparisons of 1.1 fb^{-1} 2011 7TeV CMS Data and equivalently weighted Monte-Carlo prior to the α_T selection cut, for $H_T \geq 375 \text{ GeV}$ and $\cancel{H}_T > 100 \text{ GeV}$. The α_T distribution is shown fully (left) and also shown zoomed (b) in the region $0.46 < \alpha_T < 0.6$. SUSY Signal reference points LM4 & LM6 shown for illustration of potential yields.

over MC although this observation is merely an aside, as a more detailed shape analysis will be used to evaluate this quantitatively in later sections.

6.8.2 R_{α_T} on H_T

Rather than a simple cut-and-count experiment a shape analysis in H_T bins as defined in Section sec:shape is desirable to look simultaneously in a large signal region in H_T . This is performed using the properties of the R_{α_T} variable, as discussed in Section 5.4, due to its unique properties separating the three possible components in its numerator: contamination from QCD, EWK backgrounds and SUSY signal events.

Hadronic Bulk Control Selection

While the numerator is defined by the final selection defined previously the denominator, which shall be known as the hadronic bulk control region, is defined by the pre-selection only, with the additional change of triggers essential as the cross triggers would put an inadvertent \cancel{H}_T cut, biasing the α_T distribution. Here, as it is a control region we use a suite of pre scaled H_T triggers described previously.

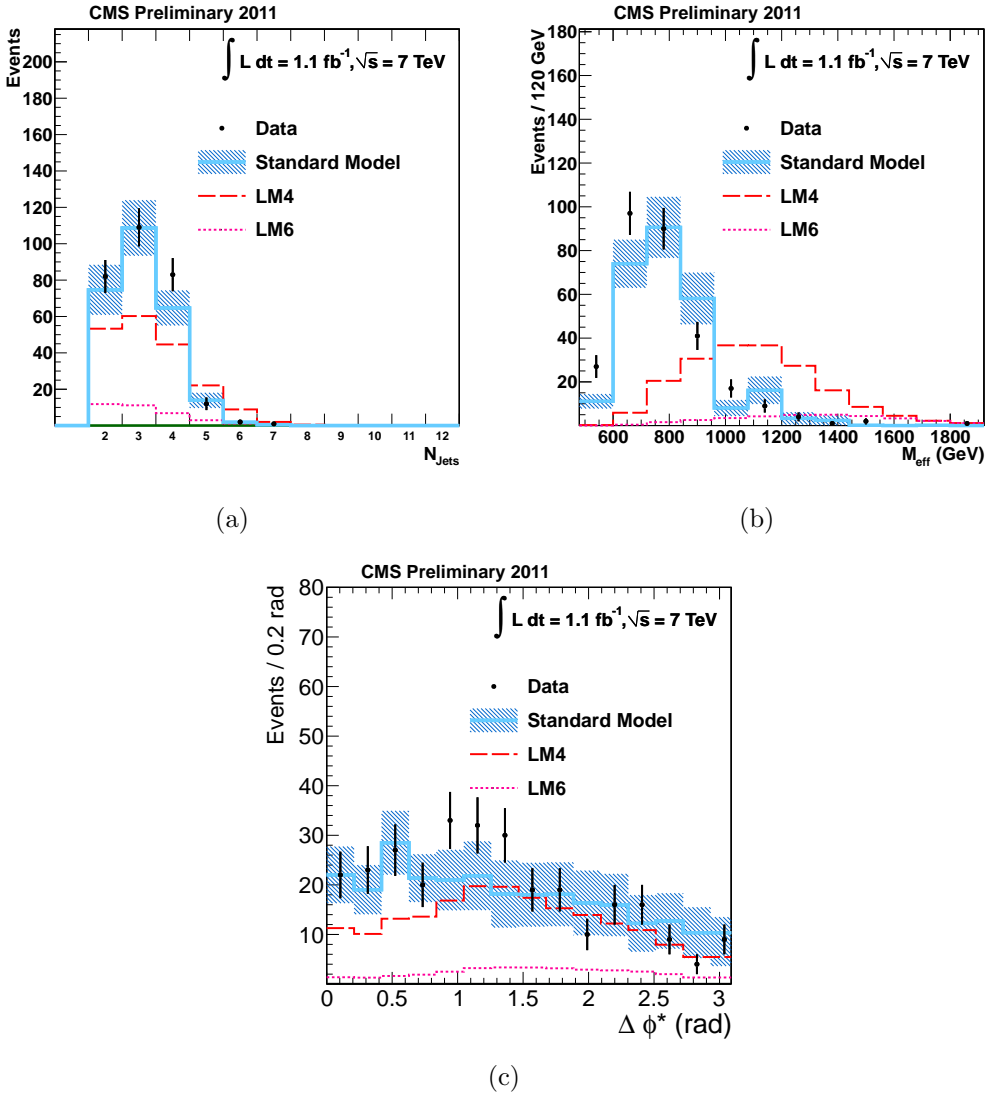


Figure 6.4: Distributions of (a) Jet Multiplicity, (b) $M_{\text{eff}} (= H_T + \not{H}_T)$ and (c) $\Delta\phi^$ showing comparisons of 1.1 fb^{-1} 2011 7TeV CMS Data and equivalently weighted Standard Model Monte-Carlo in basic kinematic quantities after the full α_T selection. SUSY Signal reference points LM4 & LM6 shown for illustration of potential yields.*

It is important to remove not just the α_T cut but all cuts of the final level selection as the cleaning cuts may introduce a bias to high missing energy. The bin-by-bin 1.1fb^{-1} yields for the hadronic signal and hadronic bulk selections are found in Table 6.10, along with each corresponding value for R_{α_T} .

H_T Bin (GeV)	275–325	325–375	375–475	475–575
$\alpha_T > 0.55$	782	321	196	62
$\alpha_T < 0.55$	$5.73 \cdot 10^7$	$2.36 \cdot 10^7$	$1.62 \cdot 10^7$	$5.12 \cdot 10^6$
$R_{\alpha_T}(10^{-5})$	$1.36 \pm 0.05_{\text{stat}}$	$1.36 \pm 0.08_{\text{stat}}$	$1.21 \pm 0.09_{\text{stat}}$	$1.21 \pm 0.15_{\text{stat}}$

H_T Bin (GeV)	575–675	675–775	775–875	875– ∞
$\alpha_T > 0.55$	21	6	3	1
$\alpha_T < 0.55$	$1.78 \cdot 10^6$	$6.89 \cdot 10^5$	$2.90 \cdot 10^5$	$2.60 \cdot 10^5$
$R_{\alpha_T}(10^{-5})$	$1.18 \pm 0.26_{\text{stat}}$	$0.87 \pm 0.36_{\text{stat}}$	$1.03 \pm 0.60_{\text{stat}}$	$0.39 \pm 0.52_{\text{stat}}$

Table 6.10: The number of events passing and failing the α_T cut and the resulting R_{α_T} value divided into H_T bins , for 1.1 fb^{-1} of data collected in 2011.

The behaviour of R_{α_T} over the range of H_T bins is further explored in Figure 6.5(a), showing the values measured from data (black) alongside those derived from SM MC simulation events in three cases: without SUSY signal (red), with LM4 signal (blue) and with LM6 signal (green). The data is consistent with a hypothesis of a flat line with a p-value of 0.29, as is the MC SM only with a p-value of 0.50. The inclusion of the LM4(LM6) signal MC events renders the distribution non-consistent with a flat hypothesis, as expected. As it is known that QCD contamination in the numerator leads to an exponentially falling R_{α_T} as H_T increases we find the data consistent with our hypothesis that the signal sample is free of QCD contamination.

To test the sensitivity of the shape of R_{α_T} to the cross-sections used in SM MC, Figure 6.5(b) shows the H_T dependence with the effective cross-sections of the major EWK backgrounds varied individually by $\pm 15\%$, to encompass the level of our current certainty of their values. In all cases the behaviour continues to be consistent with a flat hypothesis, the worst case p-value of which is 0.47 confirming the validity of the conclusion of flat behaviour. As results support the theory that α_T has removed the QCD background, no dedicated background estimation technique is needed, although a small QCD contribution will be allowed in the eventual fit to ensure that there is no bias and to account for any small remaining

contribution.

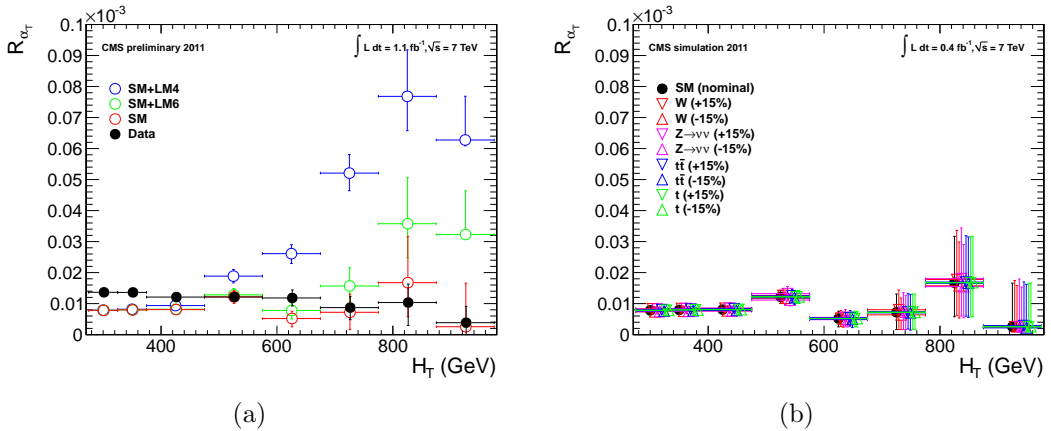


Figure 6.5: (Left) The dependence of R_{α_T} on H_T for events with $N_{\text{jet}} \geq 2$. (Right) Dependence of rat on H_T when varying the effective cross-section of the four major EWK background components individually by $\pm 15\%$. (Markers are artificially offset for clarity.)

Having eradicated the majority of the QCD background the selection is left with a remaining dominating background stemming from electroweak processes where real missing energy is created in the form of neutrinos. There are three major backgrounds relevant, $Z + \text{jets}$, $W + \text{jets}$ and $t\bar{t}$. Events with $Z + \text{jets}$ form a true irreducible background with decay to $\nu\bar{\nu}$ producing a true event with jets and missing energy, and hence requires a method of estimation to quantify its contribution to the yield. A data-driven method is used with the construction of a $\gamma + \text{jets}$ control sample.

It can be seen that there is also an irreducible background from $W + \text{jets}$ and $t\bar{t}$ events, both of which in the kinematic space of the final selection concern the decays of boosted W 's. It is interesting to understand the composition of the decays responsible, as these should be leptonic and therefore easy to identify and eliminate with our vetoes.

6.8.3 Composition of Selected $t\bar{t} + \text{jets}$ and $W + \text{jets}$ Background Events

Figure 6.6 shows the breakdown of the decays for the $t\bar{t}$ component (a), the W component (b), and for the combined $t\bar{t}$ - W background (c) after all cuts in the

final selection. The category responsible for the greatest number of events involves the decay $W \rightarrow \tau\nu$, where the tau lepton decays hadronically. In this case the tau is identified as a jet and as such fulfils the selection criteria, accounting for 41.5% of the events. The contribution from W decays to $e\nu(\mu\nu)$ where the $e(\mu)$ is outside the p_T and $|\eta|$ acceptance of the analysis account for 19.6%(21.8%), a total of 41.4% divided evenly between the flavours. Another 15.2% of events represent the veto inefficiency where the W decays to $e, \mu\nu$ within this acceptance but failing the quality criteria required (isolation, ID), the larger proportion of which is from the electron veto. There is an additional 1.8% of fully leptonic decays where more than one lepton is missed, coming from the $t\bar{t}$ source only in the case that both W bosons decay leptonically. The remaining 0.1%, representing a negligible effect (< 1 event for 1.1fb^{-1}) consist of $t\bar{t}$ decays in which non-isolated leptons are produced within jet fragmentation and meson decay, therefore regarded as a fully hadronic decay despite the existence of missing energy from neutrinos.

6.9 Estimation of $t\bar{t}$ and $W + \text{Jets}$ Backgrounds with a high p_T control sample using $W \rightarrow \mu\nu$ events.

In order to estimate the background contribution resulting from these boosted W decays from $W + \text{jets}$ and $t\bar{t} + \text{jets}$ events, a control sample is used. Here energetic W bosons that decay through a muon-neutrino pair are selected in the kinematic region of the search in order to extrapolate the expected yield in the hadronic selection.

6.9.1 μ Control Sample Selection

The aim of the μ control selection is to select events kinematically similar to those serving as background to the hadronic signal sample, but in the case of a well-identified muon, ensuring orthogonality with the signal selection. The muon veto mentioned earlier is replaced with a requirement for one and only one μ in the event, and the isolation requirement in the definition of a μ is tightened to 0.1 (compared with the hadronic analysis value of 0.15) to ensure a high purity sample of well reconstructed isolated μ 's. The final level cuts are also included

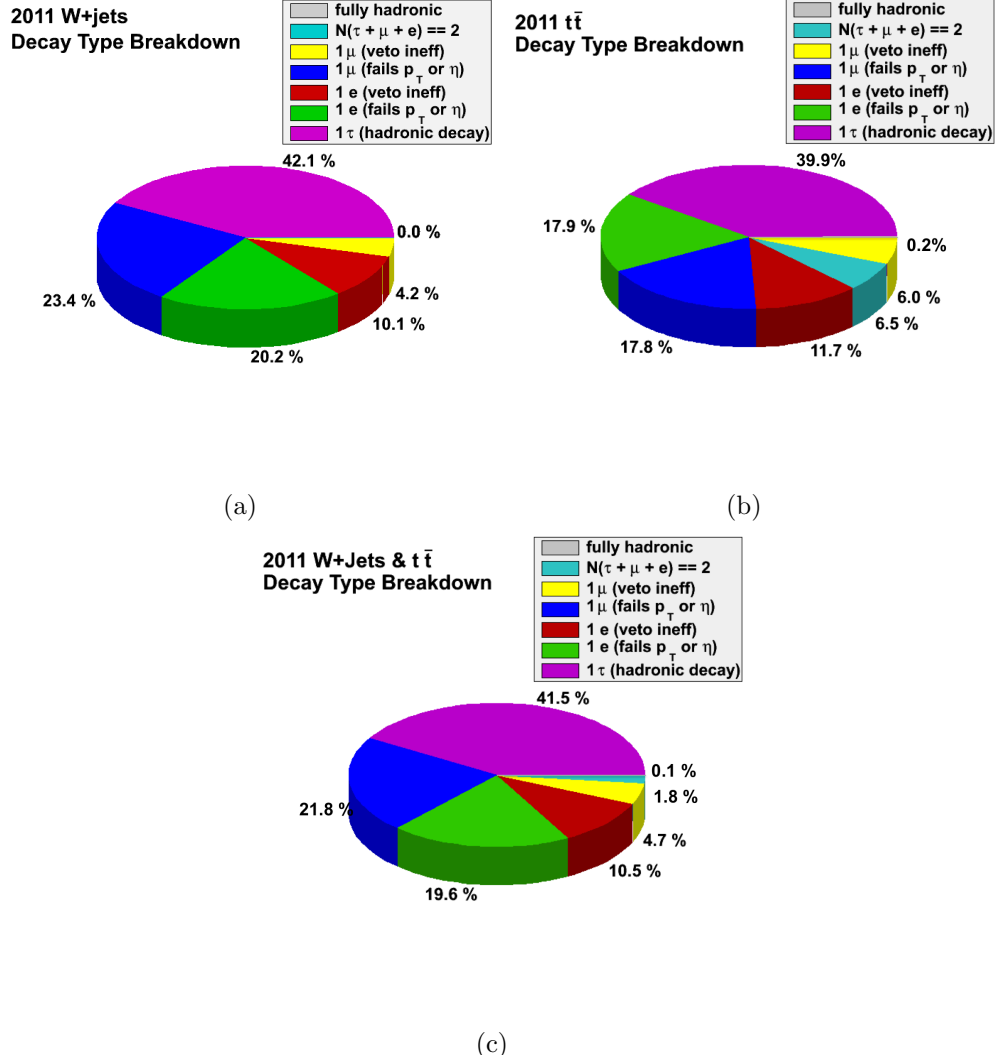


Figure 6.6: Type breakdown of decays resulting in a $W + \text{jets}$ and $t\bar{t} + \text{jets}$ event selected by the hadronic signal selection. Shown using Monte-Carlo truth information separately for $W+\text{jets}$ (a) and $t\bar{t}+\text{jets}$ (b) events, and both combined in the full $t\bar{t}-W$ background (c).

in this sample.

An additional set of requirements is also included with the muon requirement to select only events with kinematics that fit the decay $W \rightarrow \mu\nu$:

- $M_T > 30$ GeV where M_T is synonymous with the transverse mass of the W candidate.
- $\Delta R(\text{jet}, \text{muon}) > 0.5$.
- $\cancel{H}_T / H_T > 0.4$ placing an effective cut on p_T^W as this is synonymous with \cancel{H}_T .
- No second isolated muon outside of acceptance, reducing the contamination from $Z \rightarrow \mu\mu$.

Kinematic distributions of the events selected for the μ control sample are shown in Figure 6.7 prior to application of the α_T cut to demonstrate the agreement between data and Monte Carlo with high statistics. As the muon selection implicitly requires a cut on \cancel{H}_T / H_T that at its lowest ensures $\cancel{H}_T > 110$ GeV, no additional requirement is needed to ensure the trigger is efficient at the pre- α_T stage.

Agreement of data to $t\bar{t}$ - W MC in all distributions is good and no significant excess nor shape-disagreement are seen. In addition examination of the transverse mass distribution in Figure 6.7(f) confirms a peak at 80 GeV ($m^W \sim 80.385$) confirming the sample is dominated by W bosons. These observations lead to a conclusion that the sample is well modelled by Monte-Carlo and clean from contamination, confirming the validity of the selection and motivating the use of a Monte Carlo ratio in the prediction calculation. The QCD contamination is found to be negligible and therefore not seen in these distributions.

In Figure 6.8 the distributions are shown after the α_T cut, showing the same conclusions with lower statistics. This corresponds to the selection used for prediction.

6.9.2 Prediction Calculation

The prediction of the W boson decay contribution to the hadronic signal yield in the data, $W_{\text{data}}^{\text{had}}$, can be made from the analogous muon control yield W_{data}^μ providing the ratio between the hadronic and μ selections R_μ^{had} is known. This is

6.9. Estimation of $t\bar{t}$ and $W + \text{Jets}$ Backgrounds with a high p_T control sample using $W \rightarrow \mu\nu$ events.

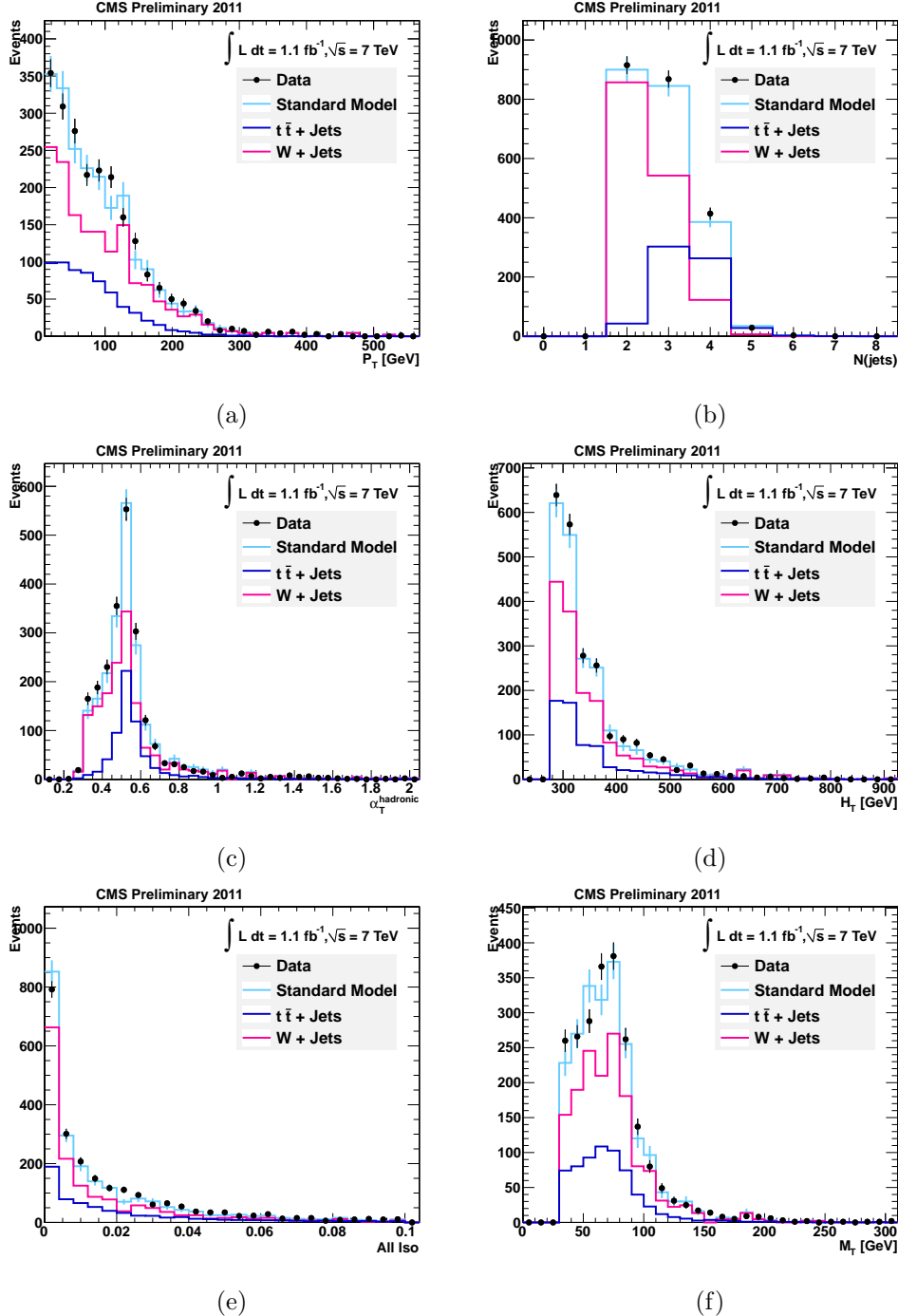


Figure 6.7: Distributions of (a) p_T^μ , (b) Jet Multiplicity ($N(\text{jet})$), (c) α_T , (d) H_T , (e) Muon Combined Isolation and (f) M_T for the μ control selection **before** the $\alpha_T > 0.55$ cut is applied. Shows comparisons of $1.1 \text{ fb}^{-1} 2011 7\text{TeV}$ CMS Data and equivalently weighted Monte-Carlo.

6.9. Estimation of $t\bar{t}$ and $W + \text{Jets}$ Backgrounds with a high p_T control sample using $W \rightarrow \mu\nu$ events.

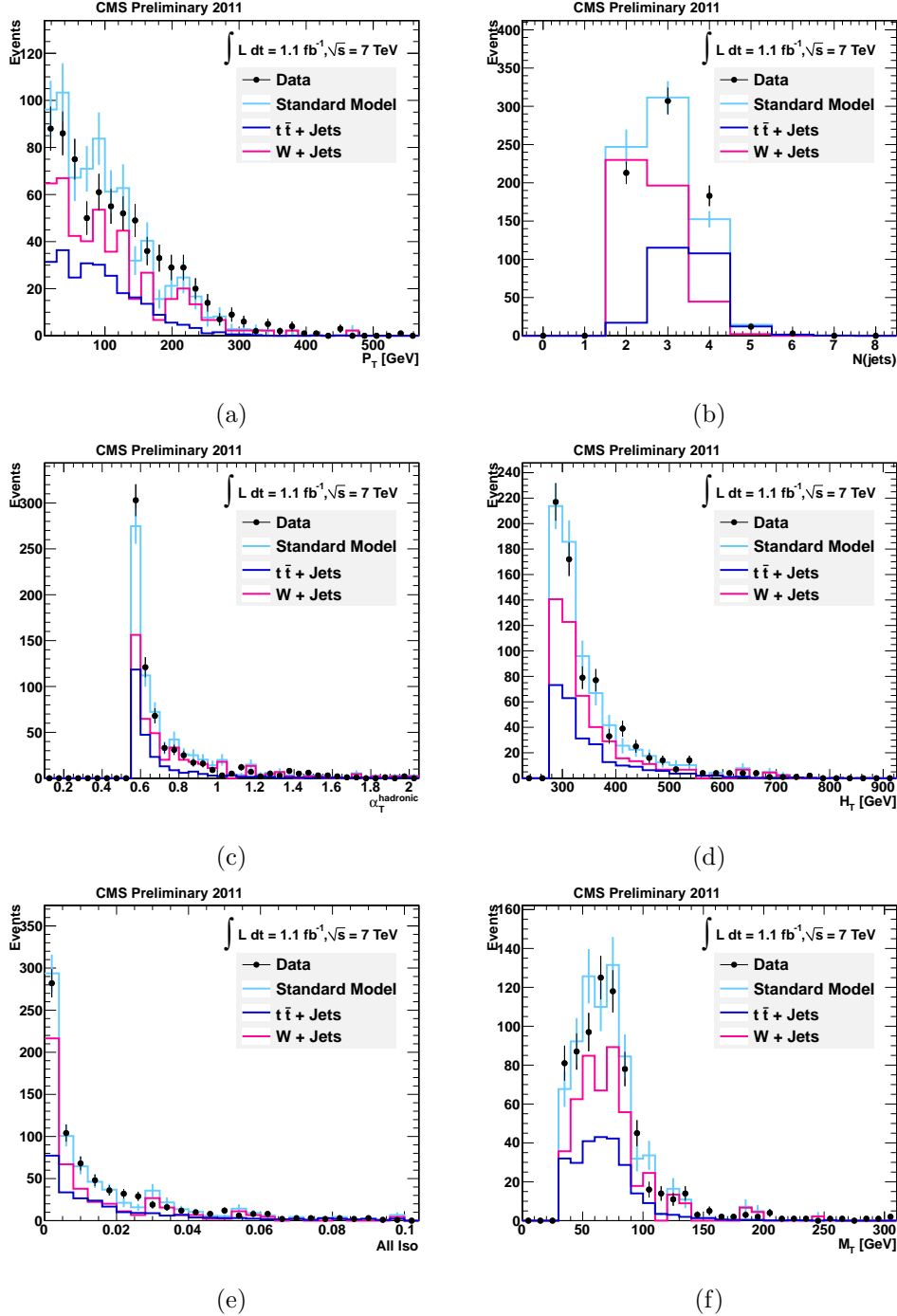


Figure 6.8: Distributions of (a) p_T^μ , (b) Jet Multiplicity ($N(\text{jet})$), (c) α_T , (d) H_T , (e) Muon Combined Isolation and (f) M_T for the μ control selection **after** the $\alpha_T > 0.55$ cut is applied. Shows comparisons of $1.1 \text{ fb}^{-1} 2011 7\text{TeV}$ CMS Data and equivalently weighted Monte-Carlo.

taken from the events passing each selection in the $t\bar{t} + \text{jets}$ and $W + \text{jets}$ Monte Carlo simulations W_{MC}^{had} and W_{MC}^μ , which corrects for the selection efficiencies and acceptance. The full estimation is made using Equation 6.1.

$$W_{data}^{had} = W_{data}^\mu \times R_\mu^{had} = W_{data}^\mu \times \left(\frac{W_{MC}^{had}}{W_{MC}^\mu} \right) \quad (6.1)$$

Calculating the contribution separately for each hadronic bin in this way results in the values for the ratio R_μ^{had} as shown in Table 6.11. As there are low MC statistics in the highest bins the errors become large, which affects the error of a prediction made. In addition, the values seem to have no trend, as expected as the behaviour of the backgrounds is not expected to change in H_T . Thus in order to improve results, one ratio R_μ^{had} is calculated for $H_T > 375$ GeV and used in the six highest bins, to provide six individual bin estimates. The two lowest bin estimates are calculated using exclusive ratios, as the MC statistics are sufficient.

H_T Bin (GeV)	R_μ^{had}
275–325	$1.14 \pm 0.06_{\text{stat}}$
325–375	$0.96 \pm 0.07_{\text{stat}}$
375–475	$0.88 \pm 0.09_{\text{stat}}$
475–575	$0.90 \pm 0.15_{\text{stat}}$
575–675	$1.31 \pm 0.37_{\text{stat}}$
675–775	$0.64 \pm 0.29_{\text{stat}}$
775–875	$0.34 \pm 0.27_{\text{stat}}$
875– ∞	$2.00 \pm 1.97_{\text{stat}}$
375–∞	$0.90 \pm 0.07_{\text{stat}}$

*Table 6.11: The bin-by-bin Monte Carlo ratios R_μ^{had} for the 8 H_T bins of the signal region, along with the ratio calculated for the inclusive region encompassing the 6 highest bins. The ratios shown in **bold** indicate those chosen for the prediction calculation to minimise additional error propagation to the prediction introduced by low MC statistics.*

The bin-by-bin results including prediction are shown in Table 6.12, with the normalised MC event yields that contribute to R_μ^{had} per bin (although the ratio quoted for the 6 higher bins is the overall ratio as described earlier) and the yields in data for the μ selection at 1.1fb^{-1} . Both statistical errors and systematic errors are quoted, the latter corresponding to a 30% uncertainty taken directly from the 2010 analysis, the calculation and validity of which are described below.

6.9. Estimation of $t\bar{t}$ and $W + \text{Jets}$ Backgrounds with a high p_T control sample using $W \rightarrow \mu\nu$ events.

H_T Bin (GeV)	275–325	325–375	375–475	475–575
MC $W + t\bar{t}$	$463.0 \pm 16.0_{\text{stat}}$	$171.2 \pm 9.5_{\text{stat}}$	$116.3 \pm 8.3_{\text{stat}}$	$43.7 \pm 5.1_{\text{stat}}$
MC $\mu + \text{jets}$	$407.5 \pm 14.5_{\text{stat}}$	$179.1 \pm 9.6_{\text{stat}}$	$131.6 \pm 8.8_{\text{stat}}$	$48.7 \pm 5.5_{\text{stat}}$
MC Ratio	1.14	0.96	0.90	0.90
Data $\mu + \text{jets}$	389	156	113	39
W + $t\bar{t}$ Prediction	$442.0 \pm 22.4_{\text{stat}}$ $\pm 132.6_{\text{syst}}$	$149.1 \pm 11.9_{\text{stat}}$ $\pm 44.7_{\text{syst}}$	$101.9 \pm 9.6_{\text{stat}}$ $\pm 30.6_{\text{syst}}$	$35.2 \pm 5.6_{\text{stat}}$ $\pm 10.6_{\text{syst}}$

H_T Bin (GeV)	575–675	675–775	775–875	875– ∞
MC $W + t\bar{t}$	$17.5 \pm 3.2_{\text{stat}}$	$5.1 \pm 1.8_{\text{stat}}$	$1.1 \pm 0.7_{\text{stat}}$	$1.8 \pm 1.0_{\text{stat}}$
MC $\mu + \text{jets}$	$13.3 \pm 2.9_{\text{stat}}$	$8.0 \pm 2.3_{\text{stat}}$	$3.2 \pm 1.4_{\text{stat}}$	$0.9 \pm 0.7_{\text{stat}}$
MC Ratio	0.90	0.90	0.90	0.90
Data $\mu + \text{jets}$	17	5	0	0
W + $t\bar{t}$ Prediction	$15.3 \pm 3.7_{\text{stat}}$ $\pm 4.6_{\text{syst}}$	$4.5 \pm 2.0_{\text{stat}}$ $\pm 1.4_{\text{syst}}$	$0.0 \pm 1.0_{\text{stat}}$	$0.0 \pm 1.0_{\text{stat}}$

Table 6.12: Muon sample predictions with 1.1fb^{-1} . Errors quoted on predictions correspond to statistical errors and an additional conservative systematic uncertainty of 30%, as used in the 2010 analysis.

6.9.3 μ Control Sample Systematic Uncertainty

Although the prediction is data-driven the reliance on the ratio R_{MC}^{had} which is taken from Monte Carlo introduces sources of uncertainty based not on the accuracy of modelling, and thus we apply conservative

Dependence of the Prediction Calculation

The number of events measured in data $W_{data,meas}^{\mu}$ is related to the actual total number of $W \rightarrow \mu\nu$ events $W_{data,actual}^{\mu}$ by the relation in Equation 6.2 where the purity p represents the fraction of events in the control sample that originate from $W + \text{Jets}$ and $t\bar{t}$ processes, and f_X, a_X and ϵ_X are the fraction of events, acceptance and efficiency of each process $X = W, t\bar{t}$.

$$W_{data,actual}^{\mu} = W_{data,meas}^{\mu} \times \left(\frac{f_W}{a_W \times \epsilon_W} + \frac{f_{t\bar{t}}}{a_{t\bar{t}} \times \epsilon_{t\bar{t}}} \right) \times p \quad (6.2)$$

The purity is assumed to be 1 due to the lack of QCD contamination demonstrated in MC.

In addition, the prediction of W_{data}^{had} in Equation 6.1 can be rewritten in

Equation 6.3 in terms of $W_{data,actual}^\mu$ and the probabilities P_X^{had} of an $W \rightarrow l\nu$ event from process X passing the hadronic signal selection as the charged lepton was not identified by the lepton vetoes.

$$W_{data}^{had} = W_{data,actual}^\mu \times \left(\frac{W_{MC}^{had}}{W_{MC,actual}^\mu} \right) = W_{data,actual}^\mu \times (f_W P_W^{had} + f_{t\bar{t}} P_{t\bar{t}}^{had}) \quad (6.3)$$

Using these two equations together yields the full dependence of the ratio R_W^{had} in Equation 6.4, analogous with Equation —refeq:mupred where we assume $p = 1$ and the other factors of which are taken directly from the MC yields.

$$W_{data}^{had} = W_{data,meas}^\mu \times \left(\frac{f_W}{a_W \times \epsilon_W} + \frac{f_{t\bar{t}}}{a_{t\bar{t}} \times \epsilon_{t\bar{t}}} \right) \times (f_W P_W^{had} + f_{t\bar{t}} P_{t\bar{t}}^{had}) \times p \quad (6.4)$$

Multiplying out the full dependence introduces quadratic terms in the fractions pertaining to each component, f_W , $f_{t\bar{t}}$ which multiply the factors $P_W^{had}/(a_W \times \epsilon_W)$ and $P_{t\bar{t}}^{had}/(a_{t\bar{t}} \times \epsilon_{t\bar{t}})$. This can be calculated in MC by dividing the yield in the MC of each component of the full hadronic signal selection without the lepton veto with that once the lepton veto has been applied. Yields normalised to 1.1fb^{-1} are shown in Table 6.13 without and with the lepton veto, and the corresponding values of $P^{had}/(a \times \epsilon)$, indicating these are similar. Using the full H_T range (left) there is a small difference not seen in the 2010 analysis which is reduced by using the highest 6 bins only. The similarity between these two factors indicates that fluctuations in the fractions of W and $t\bar{t}$ events have little effect despite their quadratic nature, allowing a linear treatment of the uncertainties on the remaining factors.

Components of the Overall Uncertainty

Although the estimation technique is data-driven the use of the ratio R_{MC}^{had} places a reliance on Monte Carlo, and so we treat all factors that affect this ratio conservatively when assigning uncertainties. The values chosen are in accord with that developed for the previous iteration of this analysis, with the following contributory factors:

- The largest contribution to the overall uncertainty is from the uncertainty

All Bins, $H_T > 275$ GeV			6 High Bins, $H_T > 375$ GeV		
X	W + Jets	$t\bar{t} + \text{jets}$	X	W + Jets	$t\bar{t} + \text{jets}$
Before e,μ vetoes	2161.86	1035.50	Before e,μ vetoes	568.34	283.92
After e,μ vetoes	594.24	227.53	After e,μ vetoes	126.62	58.91
$P_X^{\text{had}}/(a_X \times \epsilon_X)$	0.27	0.22	$P_X^{\text{had}}/(a_X \times \epsilon_X)$	0.24	0.23

Table 6.13: $t\bar{t}$ -W MC yields having passed all the hadronic signal final selection cuts without and with the lepton vetoes, normalised for 1.1fb^{-1} . The factor $P_X^{\text{had}}/(a_X \times \epsilon_X)$ for each process X is calculated from the division of the full selection yield by the yield before the vetoes are applied.

of the probability p for a W decay to pass the lepton veto, divided into individual uncertainties on each type of decay averaged whilst weighted by the frequency of that decay as described earlier in Section 6.8.3. Overall this contributes 23%, consisting of the following components assigned in conduction with 2010 W and Z cross-section measurements [61]:

- Events surviving due to hadronic tau decays are governed by the tau-jet response. In order to obtain the uncertainty the response was varied by $\pm 10\%$, a conservative amount given the JES it at its greatest 6%. The MC yield from such decays changed by 7% under this variation, and so we choose this for our uncertainty.
- Events out of acceptance rely on accurate modelling of a . The properties of W are found to be well modelled but the measurement is performed for higher p_T than we use in this analysis, therefore we apply a conservative 10%.
- The inefficiency of lepton ID requirements measured in electrons has a 30% under-estimation from MC in data. In muons the under-estimate is slight, but the uncertainty from Isolation requirements is not well understood, as unknown pile-up effects could alter this drastically. Therefore a conservative 100% estimate is applied to remain above measured discrepancies, given the small proportion of events this effects.
- The small number of fully leptonic $t\bar{t}$ decays is dominated by di- τ events. The expected uncertainty should take into account all the above effects, as all are relevant and responsible for some of these

events remaining. In this case we assign a 50% uncertainty .

- The effect of acceptance a times efficiency $\epsilon^{1/a} \times \epsilon$ is predicted using the MC, but there is an uncertainty resulting from the difference in this between MC and data, which when measured for W and Z cross sections contributes 1.6%, and for $t\bar{t}$ it is 6.1%. Conservatively we chose 6.1% which represents an overestimate as the proportion of W events in reality reduces this component.
- There is an uncertainty on the assumption the that the control sample is pure, i.e. that the fraction of events f in the sample that come from W and $t\bar{t}$ decays is 1. From Monte Carlo we have observed the contamination from QCD to be negligible, but to allow for poor QCD MC modelling assign a conservative uncertainty of 200% on the expected QCD yield, still only contributing a 3% uncertainty on f .

The overall uncertainty is then achieved by adding these components in quadrature, which yields a value of 24%. Whilst lower than the value taken from the 2010 analysis, 30%, it is consistent and shows there is not an underestimate. The error is reduced due to the inclusion of the two low H_T bins which reduces the overall percentage contributed from the lepton veto inefficiency, which propagates the highest error. Excluding the lower two bins brings this calculation in line with 30% and as the overall sensitivity is lowest in these two bins the outcome of introducing an over-estimate of the uncertainty will have little effect on the limit.

6.9.4 Signal Contamination in μ Control Sample

In the case where SUSY-like New Physics exists, the μ selection may receive some contamination from signal events producing missing energy alongside one lepton. Table 6.14 shows the bin-by-bin event yields for test point LM6 alongside the yields from SM, and the relevant significance s/b . The contamination is small in all but the highest bin where the significance exceeds 1.

As there can be such contamination and this depends on the model of signal, the possible signal contribution must be included in the μ control sample during the simultaneous fit. This will be included through the % efficiency of the μ selection in bin i , ϵ_μ^i obtained by

$$\epsilon_{\mu}^i = 100 \times \frac{N_{\mu}}{N_{tot}} \quad (6.5)$$

where N_{μ} is the number of signal events that pass the μ selection, and N_{tot} is the total number of signal events prior to selection. The values of ϵ_{μ}^i for LM6 are also included in Table 6.14, where the value of N_{tot} for LM6 is 335.23.

H_T Bin (GeV)	275–325	325–375	375–475	475–575
SM ($W + t\bar{t}$)	407.5	179.1	131.6	48.7
LM6	0.13	0.15	0.53	0.82
S/B	0.00	0.00	0.00	0.02
$\epsilon_{\mu}^i(\text{LM6})$ (%)	0.045	0.045	0.16	0.25

H_T Bin (GeV)	575–675	675–775	775–875	875– ∞
SM ($W + t\bar{t}$)	13.3	8.0	3.2	0.9
LM6	1.09	1.17	0.95	1.21
S/B	0.08	0.15	0.30	1.34
$\epsilon_{\mu}^i(\text{LM6})$ (%)	0.325	0.348	0.283	0.362

Table 6.14: Signal contamination yields from LM6 in the μ Control Sample in 1.1fb^{-1} Monte Carlo, shown alongside Standard Model MC yields and significance S/B . Efficiency of the μ selection in LM6 $\epsilon_{\mu}^i(\text{LM6})$ in % is calculated by $100 * (\text{yield}/N_{tot})$ where N_{tot} is the total events in the LM6 sample at 1.1fb^{-1} , 335.23.

6.10 Estimation of $Z \rightarrow \nu\bar{\nu} + \text{jets}$ background using photon + jets events

The irreducible background from the Z boson decay to a $\nu\bar{\nu}$ pair is estimated with the use of an energetic γ control sample, in a similar manner to that described for the μ control sample. The similarity between the kinematics of $Z \rightarrow \nu\bar{\nu} + \text{jets}$ events and $\gamma + \text{jets}$ can be exploited, in the scenario where the photon is disregarded from calculations of quantities H_T , \cancel{H}_T and α_T . The events therefore appear to have missing energy with a similar spectrum to that of $Z \rightarrow \nu\bar{\nu}$ events, albeit being produced at a larger cross-section [62]. This method has been designed and documented in [63].

The γ control sample is defined similarly to that of the μ control sample, retaining the hadronic signal region final selection with the removal of the photon veto and the following photon requirements:

- $p_T^\gamma > 100$ GeV putting the photon momentum above the mass of the Z (91.2 GeV) to enhance the similarity of kinematics.
- $|\eta^\gamma| < 1.45$
- $\Delta R(\gamma, \text{jet}) > 1$

The α_T and Jet Multiplicity distributions of the γ control sample selection events prior to the α_T cut are shown in Figure 6.9 for the bins in the region $H_T > 375$ GeV for data and MC from QCD and $\gamma + \text{jets}$ events, taken from MADGRAPH. The distributions show good shape agreement although the total yield in data is higher than in MC. As the method will only use MC to make a comparison ratio between the two selections any inaccuracies of the cross-section have no relevance to the estimation and therefore the method is still valid.

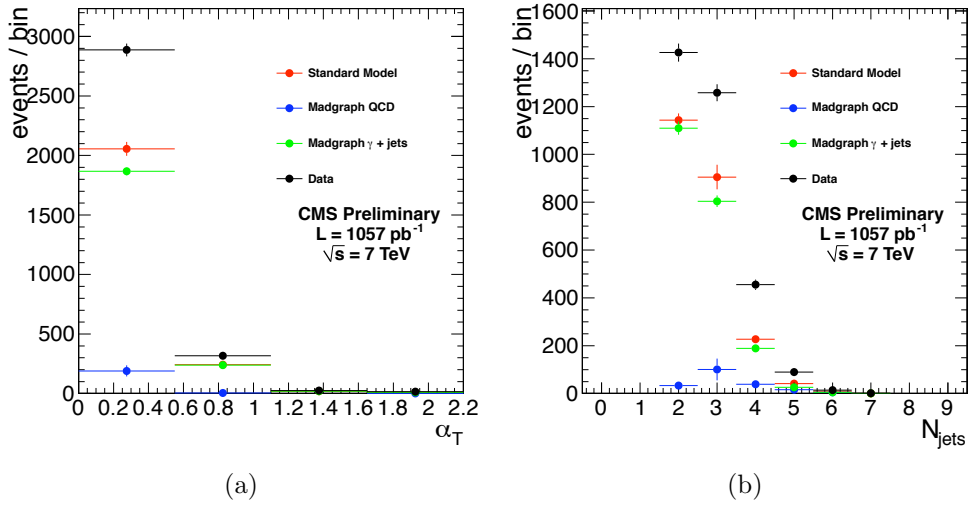


Figure 6.9: Data-MC comparisons for the photon control sample. $H_T > 375$ GeV and $\mathcal{H}_T/H_T > 0.4$ are required. Left: the distribution of α_T . Right: the distribution of the number of jets.

After the α_T cut the γ control sample is mainly free from QCD although there is a small number of events remaining, resulting in a purity factor of 0.92 and 0.97 in the two lowest bins and 0.99 in all other bins.

6.10.1 Z Background Prediction Calculation

In a similar way to the tt-W prediction, it is possible to extrapolate the prediction for the Z component of the hadronic signal yield, Z_{data}^{pred} from the measured yield of events in the $\gamma + \text{jets}$ control sample γ_{data}^{meas} , using as a translation factor the ratio $R_{Z/\gamma}^{MC}$. This is described in Equation 6.6, where the ratio $R_{Z/\gamma}^{MC}$ is created using the hadronic signal yield from Z + jets MC events, Z_{MC} and the γ control selection yield in $\gamma + \text{jets}$ MC, γ_{MC} . The purity of the γ selection p is included as a multiplicative factor to correct for the QCD contamination in γ_{data}^{meas} , i.e. $\gamma_{data}^{corr} = p\gamma_{data}^{meas}$.

$$Z_{data}^{pred} = p \times \gamma_{data}^{meas} \times R_{Z/\gamma}^{MC} = \gamma_{data}^{corr} \times \left(\frac{Z_{MC}}{\gamma_{MC}} \right) \quad (6.6)$$

The calculation for the ratio $R_{Z/\gamma}^{MC}$ is performed once in each of the two lowest signal bins, whilst the six higher bins use one shared ratio as in the μ control method. The variation of the shapes with H_T are minimal and this approach minimises the error from MC statistics that will be passed on to the prediction in the highest bins.

The bin-by-bin results including prediction are shown in Table 6.15, with the normalised MC event yields that contribute to R_μ^{had} per bin and the yields in data for the γ selection at 1.1fb^{-1} . On the prediction both statistical errors and systematic errors are quoted, the latter corresponding to a 40% uncertainty used in the previous analysis, the components of which are listed below.

6.10.2 γ Control Sample Systematic Uncertainty

As in the μ control sample, the data-driven estimation techniques rely on a Monte Carlo ratio, and so we treat all factors that affect this ratio conservatively when assigning uncertainties. The values chosen are in accord with that developed for the previous iteration of this analysis, with the following contributory factors:

- As the Madgraph MC samples used are different in the numerator and denominator a factor of theoretical uncertainty exists on the relative cross-sections, taken conservatively as 30% [62] from MADGRAPH [64].
- The acceptance a is assigned an uncertainty of 5%, given the understanding of $\gamma + \text{jets}$ processes is good. The efficiency ϵ is assigned a conservative

H_T Bin (GeV)	275–325	325–375	375–475	475–575
MC $Z \rightarrow \nu\bar{\nu}$	$212.6 \pm 20.4_{\text{stat}}$	$92.0 \pm 20.4_{\text{stat}}$	$61.3 \pm 20.4_{\text{stat}}$	$42.9 \pm 10.2_{\text{stat}}$
MC $\gamma + \text{jets}$	$613.1 \pm 20.4_{\text{stat}}$	$265.7 \pm 10.2_{\text{stat}}$	$168.6 \pm 10.2_{\text{stat}}$	$55.2 \pm 8.2_{\text{stat}}$
MC Ratio	0.35	0.35	0.44	0.44
Data $\gamma + \text{jets}$	867.5	313.7	214.6	68.5
Sample Purity	0.92	0.97	0.99	0.99
$Z \rightarrow \nu\bar{\nu}$ Prediction	$276.8 \pm 9.5_{\text{stat}}$ $\pm 110.7_{\text{syst}}$	$105.3 \pm 6.0_{\text{stat}}$ $\pm 42.1_{\text{syst}}$	$93.5 \pm 6.4_{\text{stat}}$ $\pm 37.4_{\text{syst}}$	$29.8 \pm 3.6_{\text{stat}}$ $\pm 11.9_{\text{syst}}$

H_T Bin (GeV)	575–675	675–775	775–875	875– ∞
MC $Z \rightarrow \nu\bar{\nu}$	$5.1 \pm 5.1_{\text{stat}}$	$0.0 \pm 3.1_{\text{stat}}$	$3.1 \pm 3.1_{\text{stat}}$	$0.0 \pm 3.1_{\text{stat}}$
MC $\gamma + \text{jets}$	$23.5 \pm 5.1_{\text{stat}}$	$3.1 \pm 2.0_{\text{stat}}$	$3.1 \pm 2.0_{\text{stat}}$	$2.0 \pm 1.0_{\text{stat}}$
MC Ratio	0.44	0.44	0.44	0.44
Data $\gamma + \text{jets}$	24.5	12.3	4.1	4.1
Sample Purity	0.99	0.99	0.99	0.99
$Z \rightarrow \nu\bar{\nu}$ Prediction	$10.7 \pm 2.2_{\text{stat}}$ $\pm 4.3_{\text{syst}}$	$5.3 \pm 1.5_{\text{stat}}$ $\pm 2.1_{\text{syst}}$	$1.8 \pm 0.9_{\text{stat}}$ $\pm 0.7_{\text{syst}}$	$1.8 \pm 0.9_{\text{stat}}$ $\pm 0.7_{\text{syst}}$

Table 6.15: Bin-by-bin prediction of $Z \rightarrow \nu\bar{\nu}$ irreducible background after final selection, using $\gamma + \text{jets}$ control sample with 1.1fb^{-1} 2011 data.

20% as although the ID variables are validated with tag-and-probe [] the tests are not reformed in the high H_T

- The purity P is assigned an 20% uncertainty to take into account the uncertainty in the modelling of QCD MC which is used to estimate contamination.

Combining these events in quadrature and rounding to the nearest 10% yields an overall uncertainty of 40%

6.10.3 Cross-Prediction between Control Samples

A cross-prediction can be made between the two control samples, providing a cross-check in order to validate the methods and assigned systematics. The number of $W + \text{jets}$ events with μ decays $N_{\text{data},\text{pred}}^W$ can be predicted from the γ control sample, exploiting the similarities between the kinematics of $W \rightarrow \mu\nu + \text{jets}$ and $Z \rightarrow \nu\bar{\nu} + \text{jets}$. In order to ensure the sample is not contaminated by events from $t\bar{t}$ production, an additional requirement that the jet multiplicity is

constrained to 2 is made in both selections. The prediction proceeds using the same MC ratio strategy, as in Equation 6.7.

$$N_{\text{pred}}^W = N_{\text{data}}^\gamma \times \left(\frac{N_{\text{MC}}^W}{N_{\text{MC}}^\gamma} \right) \quad (6.7)$$

The ratio $N_{\text{MC}}^W/N_{\text{MC}}^\gamma$ is found to be independent of H_T and therefore one factor 0.42 ± 0.04 is extracted for the whole set of bins. The results of the prediction are shown in Table 6.16 alongside the number of W + jets events $N_{\text{data,meas}}^W$ found in data from the selection with MC statistical errors and systematic uncertainties in line with those described for the two control samples.

H_T	N_{data}^γ	$N_{\text{MC}}^W/N_{\text{MC}}^{\text{phot}}$	N_{pred}^W	N_{obs}^W
275	336	$0.42 \pm 0.04_{\text{MCstat}}$	$141.8 \pm 7.7_{\text{stat}} \pm 14.6_{\text{MCstat}} \pm 56.7_{\text{syst}}$	128
325	127	$0.42 \pm 0.04_{\text{MCstat}}$	$53.6 \pm 4.8_{\text{stat}} \pm 5.5_{\text{MCstat}} \pm 21.4_{\text{syst}}$	37
375	96	$0.42 \pm 0.04_{\text{MCstat}}$	$40.5 \pm 4.1_{\text{stat}} \pm 4.2_{\text{MCstat}} \pm 16.2_{\text{syst}}$	36
475	27	$0.42 \pm 0.04_{\text{MCstat}}$	$11.4 \pm 2.2_{\text{stat}} \pm 1.2_{\text{MCstat}} \pm 4.6_{\text{syst}}$	12
575	13	$0.42 \pm 0.04_{\text{MCstat}}$	$5.5 \pm 1.5_{\text{stat}} \pm 0.6_{\text{MCstat}} \pm 2.2_{\text{syst}}$	2

Table 6.16: Predictions of $W \rightarrow \mu\nu + 2$ jets events using the $\gamma + \text{jets}$ sample at 1.1fb^{-1} , including statistical errors and a systematic uncertainty of 40% as used in the $Z + \text{Jets}$ prediction.

The number of events predicted are compatible with those measured in data within the uncertainties estimated by the techniques.

6.11 Signal Region Systematic Uncertainties

A number of experimental systematic uncertainties have an effect on the efficiencies of potential signal, which are detailed here.

Luminosity

The measurement of luminosity taken propagates through to an uncertainty on the signal event yield when considering any new physics model, which is currently 6% [56]

Effect of dead ECAL cut

The cut that removes events where a jet points towards a region with masked ECAL towers has varying efficiencies for different signal models. This introduces an uncertainty based on the distribution about the mean. A study using several points in the CMSSM yields a standard deviation $\sim 2\%$. In addition there is a contribution to the uncertainty due to the resolution of ΔR , 0.05 for jets with $p_T > 100$ GeV. Such a variation corresponds to 2.2%, and the overall uncertainty for this cut is therefore 3%

Effect of $e/\mu/\gamma$ Veto

The rejection of leptons and photons have efficiencies that agree in data very well with QCD Monte Carlo using three different generators (PYTHIA6, PYTHIA8, MADGRAPH), the variation of which is at maximum 0.8% for the total effect which rejects $\sim 5\%$ of events. We choose to assign half this value, 2.5% representing 50% of the total veto inefficiency.

Jet Energy Scale and Resolution

Fluctuations of the JES affect the jets that pass the p_T and H_T requirement, which has an effect on the overall result. Varying this in accordance with results described in Section 4.4.2 show variations on yields of CMSSM points within $+1.9\%$ and -2.2% , of which a systematic of 2% is chosen as the latter would not artificially improve the yield. The resolution from MC is found to be 10-15% better than in data, and our correction for that yields a 1% uncertainty on signal yield. Overall 2.5% is contributed from JES and resolution.

Theoretical Uncertainty

In addition to the experimental uncertainties listed above, there is a theoretical contribution stemming from the choice of the renormalisation and factorisation scales used to calculate NLO cross sections and the PDF's used in signal Monte Carlo contribute an 10% effect.

Adding all these sources of uncertainty in quadrature gives an overall uncertainty of 12.5%, which is carried onwards to the limit calculation.

6.12 Statistical Interpretation

Having obtained the yields and predictions as detailed in previous sections, it is desirable to quantify and interpret the results of the three selections simultaneously with respect to the SM only hypothesis and also possible CMSSM SUSY signal. The results in all 3 selections are used simultaneously together in order to draw conclusions. A likelihood model is used for each of the three samples describing the relevant results along with the uncertainties, with the number of observed events in each assumed to have a Poisson Distribution $\text{Pois}(n|\mu)$ where the number of expected events is μ as in Equation 6.8.

$$\text{Pois}(n|\mu) = \frac{\mu^n}{n!} e^{-\mu} \quad (6.8)$$

The likelihood of μ being the number of expected events given the outcome n can then be expressed in terms of this probability distribution. Where μ depends on a set of unknown parameters maximising L provides estimates for the models parameters. The $N=8$ measurements corresponding to each H_T bin enter the likelihood distinctly and simultaneously through a product of Poisson distributions. It does not distinguish between bins of differing width.

6.12.1 Hadronic Signal Selection Likelihood

Given a set of observed event yields for the hadronic signal selection n^i in $i=1,\dots,N$ H_T bins, the likelihood L_{had} is described by:

$$L_{had} = \prod_i \text{Pois}(n^i | b^i + s^i) \equiv \prod_i \text{Pois}(n^i | b_{ewk}^i + b_{qcd}^i + s^i) \quad (6.9)$$

where the expected yields are composed of s^i the expected number of signal events in the i th bin, and b^i the expected Standard Model background, assuming $b^i \equiv b_{ewk}^i + b_{qcd}^i$ where b_{ewk}^i is the expected yield from electroweak processes, and b_{qcd}^i the expected yield from QCD.

6.12.2 Expression of b^i using R_{α_T} evolution in H_T

The separation of b^i into electroweak and QCD components allows the expression of each in terms of its characteristic behaviour of R_{α_T} as H_T evolves.

The hypothesis of R_{α_T} exponentially falling with increasing H_T can be expressed as a function of two parameters A and k in the following way:

$$R_{\alpha_T}(H_T) = Ae^{-kH_T}, \quad (6.10)$$

This can be used to express a hypothesis of flat behaviour also, by setting k = 0. A further observation is introduced, m^i which represents the observation of the hadronic bulk selection (where $\alpha_T < 0.55$). It is then possible to express the expected background b_p^i from a process p in terms of the H_T distribution of these bulk events, dN/dH_T :

$$b_p^i = \int_{x_i}^{x_{i+1}} \frac{dN}{dH_T} Ae^{-kH_T} dH_T, \quad (6.11)$$

where x_i is the lower bin edge in H_T , and x_{i+1} represents the upper edge (∞ in the case of the final bin). To simplify this continuous distribution the assumption is made that the full distribution of a given bin occurs at the mid-point of the bin, the mean $\langle H_T \rangle^i$, allowing the expression in terms of m^i :

$$\frac{dN}{dH_T} = \sum_i m^i \delta(x - \langle H_T \rangle^i), \quad (6.12)$$

yielding the full dependence of b_p^i in Equation 6.13.

$$b_p^i = \int_{x_i}^{x_{i+1}} m^i \delta(x - \langle H_T \rangle^i) Ae^{-kH_T} dH_T \quad (6.13)$$

This allows the expression in Equation ?? of the two components of b^i , in which the knowledge that R_{α_T} is flat in electroweak processes, and therefore $k_{ewk} = 0$ is used.

$$b_{ewk}^i = m^i A_{ewk} \quad b_{qcd}^i = m^i A_{qcd} e^{-k_{qcd} \langle H_T \rangle^i}. \quad (6.14)$$

The likelihood of the full set of the background expectations b^i now depends on three nuisance parameters, A_{ewk} , A_{qcd} and k_{qcd} .

6.12.3 Electroweak Control Sample Likelihoods

The electroweak component of the background b_{ewk}^i can additionally be decomposed into terms of the expected number of Z and $t\bar{t}W$ components b_Z^i and $b_{t\bar{t}W}^i$. Reversing $b_{ewk}^i = b_Z^i + b_{t\bar{t}W}^i$ by introducing a set of fit parameters f_Z^i , the fraction

of electroweak events that are Z in the i th bin, each component can be expressed as follows:

$$b_Z^i = f_Z^i \times b_{ewk}^i \quad b_{t\bar{t}W}^i = (1 - f_Z^i) \times b_{ewk}^i \quad (6.15)$$

Each of these components has an observational measurement n_γ and n_μ taken from the event yield in the photon and muon control samples respectively. Corresponding yields in simulation MC_γ^i and MC_μ^i are also known, along with the value in simulation of the expected amounts of Z and $t\bar{t}$ W in the hadronic signal region MC_Z^i and $MC_{t\bar{t}W}^i$, which combine to define the ratios r_γ^i and r_μ^i as follows:

$$r_\gamma^i = \frac{MC_\gamma^i}{MC_Z^i} \quad r_\mu^i = \frac{MC_\mu^i}{MC_{t\bar{t}W}^i} \quad (6.16)$$

The likelihoods regarding the two measured yields n_γ^i, n_μ^i can then be fully expressed as in Equation 6.17 and 6.18 with an additional parameter s_μ^i represents the expected signal events contaminating the muon control sample for a given signal model.

$$L_\gamma = \text{Gaus}(1.0 | \rho_\gamma^Z, \sigma_\gamma^Z) \prod_i \text{Pois}(n_\gamma^i | \rho_\gamma^Z r_\gamma^i b_Z^i) \quad (6.17)$$

$$L_\mu = \text{Gaus}(1.0 | \rho_\mu^{t\bar{t}W}, \sigma_\mu^{t\bar{t}W}) \prod_i \text{Pois}(n_\mu^i | \rho_\mu^{t\bar{t}W} r_\mu^i b_{t\bar{t}W}^i + s_\mu^i) \quad (6.18)$$

In addition to the Poisson product an additional Gaussian has been incorporated to account for the systematic error, in which $\rho_\gamma^Z, \rho_\mu^{t\bar{t}W}$ are the correction factors that account for the systematic uncertainties $\sigma_\gamma^Z, \sigma_\mu^{t\bar{t}W}$ associated with the respective prediction constraints. We assume the uncertainties are fully correlated across the range of bins.

These two electroweak likelihoods add an additional dependance on the N parameters f_Z^i as well as two uncertainty correction factors $\rho_\gamma^Z, \rho_\mu^{t\bar{t}W}$.

6.12.4 Presence of Signal

Where the hypothesis includes presence of signal events the likelihood requires an additional component, representing the effect of systematic uncertainties associated with signal efficiency, σ^{sig} . This is treated with a Gaussian as in

the electroweak cases, and introduces the correction factor ρ^{sig} :

$$L_{signal} = Gaus(1.0 | \rho^{sig}, \sigma^{sig}) \quad (6.19)$$

With the inclusion of this uncertainty correction in the full likelihood the signal contribution s^i in Equation 6.9 can be rewritten in terms of the cross-section x of the model and the measured luminosity l , using the efficiency of the analysis in bin i , ϵ_{had}^i .

$$s^i = f \rho_{sig} x l \epsilon_{had}^i \quad (6.20)$$

This introduces the multiplicative factor f^x to be applied to the cross section. This represents the parameter of interest for which we shall determine an allowed interval. Analogously the signal contamination in the muon control region s_μ^i in Equation ?? is also written using these factors and the muon selection efficiency for signal ϵ_μ^i as described in Section 6.9.4:

$$s_\mu^i = f \rho_{sig} x l \epsilon_\mu^i \quad (6.21)$$

6.12.5 Total Likelihood

The total likelihood is then expressed in Equation 6.22, as a product of the individual likelihood functions described previously.

$$L_{tot} = L_{had} \times L_\gamma \times L_\mu \times L_{signal} \quad (6.22)$$

The parameters of the full likelihood are then the R_{α_T} components: A_{ewk} , A_{qcd} and k_{qcd} , the N factors $\{f_Z^i\}$, the three uncertainty corrections ρ^{sig} , ρ_γ^Z and $\rho_\mu^{t\bar{t}W}$ and the strength of the signal f_x . These number $7 + N$ in total with f_x the primary parameter of interest whilst the other $6 + N$ are regarded as nuisance parameters.

6.13 Testing the SM-only hypothesis

Dropping contributions from possible signal to the likelihood (setting $s^i = s_\mu^i = 0$) allows consideration of the SM background-only hypothesis. Given

the observations in data the likelihood is maximised over all of the parameters with the tools Minuit [65] and RooFit, and the maximum is recorded (L_{max}^{data}). The values of the parameters at this maximum value are known as maximum likelihood estimates (MLEs).

The likelihood function with the MLEs plugged in is then used as a p.d.f for observations, and many pseudo-experiments are generated from it. Starting with the observations in each pseudo-experiment, the likelihood is then re-maximised over all parameters in order to generate a distribution of the valleys of L at maximum, L_{max} . The p-value of the actual observation is found to be 0.56, obtained by examining the quantile of L_{max}^{data} in this distribution.

The results of the fit are shown in Figure 6.10 separately for the three samples, each with the actual yields from data (black) compared to the fit results (blue). The hadronic signal results (top) are shown alongside the predictions from the μ and γ control samples. For the hadronic and muon (middle) samples where signal (when present) would contribute, the distribution of SM with LM6 signal present is shown also for illustration purposes, although this does not enter the fit or affect the results.

All three samples show good agreement between the data and fit results, indicating the measured yields are compatible with the SM-only hypothesis. In Figure 6.11 the R_{α_T} distribution is shown by dividing the hadronic sample data and fit results by the measured bulk yields m^i . The electroweak component is flat as was required for the fit. The QCD component exhibits falling behaviour with MLEs $k = (5.2 \pm 5.6) \times 10^{-3}$ and $A_{qcd} = (1.4 \pm 1.9) \times 10^{-5}$, consistent with the concept of negligible QCD contamination. Although the presence of QCD was specified in the fit, a cross-check setting the QCD component to zero returns a p-value from the fit of 0.41 confirming the approach.

The good agreement between data and the Standard Model indicates a lack of signal, in which case the inclusion of signal in the likelihood is used to interpret the results in the plane of the CMSSM. The method of this is described in the following section.

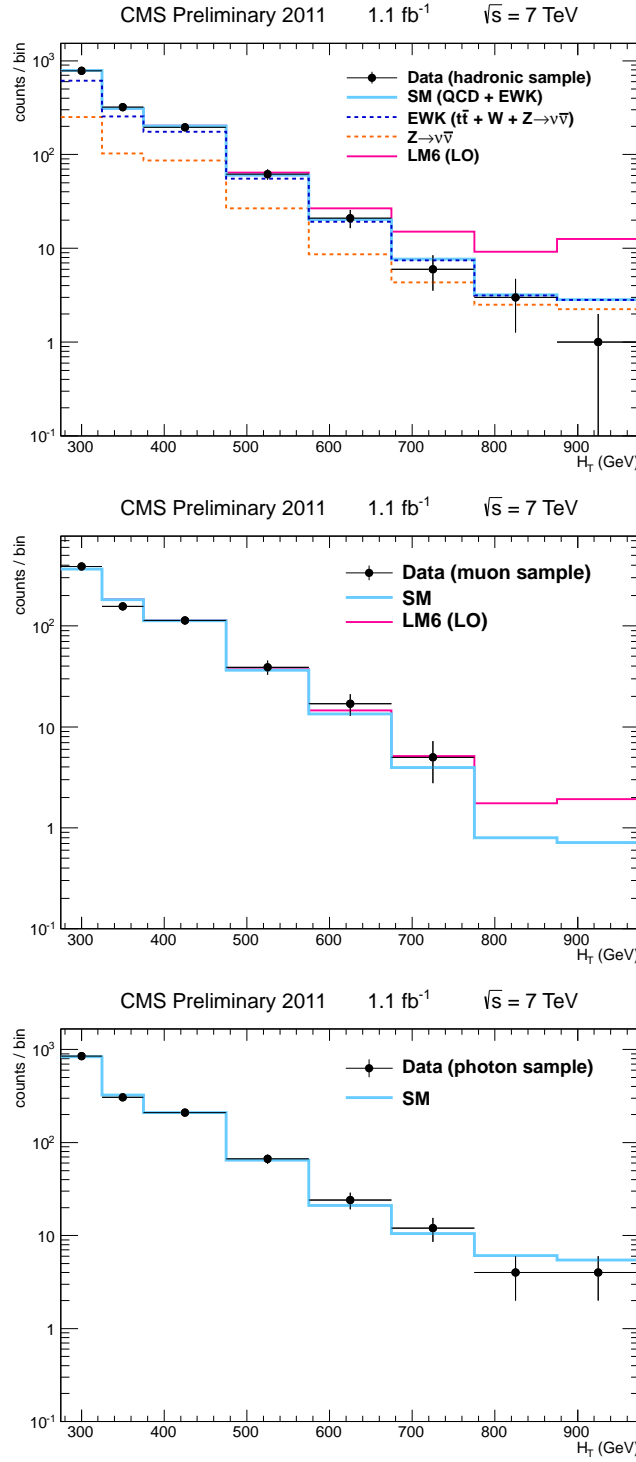


Figure 6.10: SM-only goodness of fit results for events in the hadronic (top), muon (middle) and photon (bottom) samples. Each H_T bin shows data observation (black points) and the outcome of the fit (blue line). For hadronic selection the breakdown of the individual background contributions as predicted by the control samples is shown also. Signal contribution from benchmark point LM6 is shown stacked with SM for illustration (pink line) but has no role in the fit.

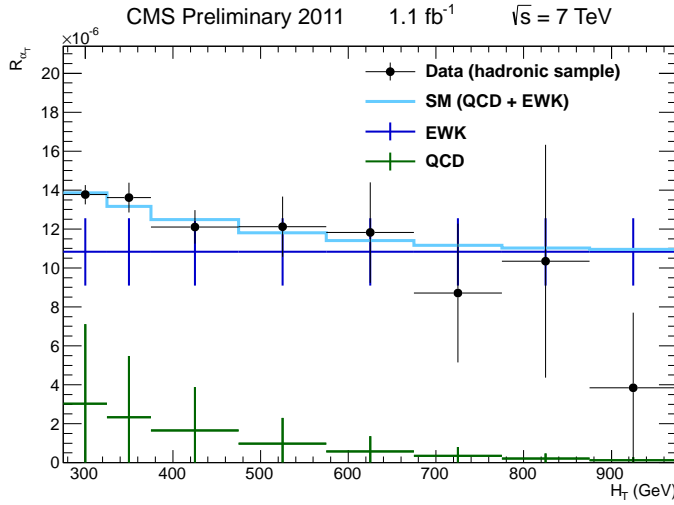


Figure 6.11: R_{α_T} as a function of H_T as observed in data (black points) and the results of the fit (blue) both divided through by the bulk observations. The components of the background are shown also, where the electroweak was fixed as flat during the fit whilst qcd was allowed to fall exponentially.

H_T Bin (GeV)	275–325	325–375	375–475	475–575
W + $t\bar{t}$ background	363.7	152.2	88.9	28.8
Z $\rightarrow \nu\bar{\nu}$ background	251.4	103.1	86.4	26.6
QCD background	172.4	55.1	26.9	5.0
Total Background	787.4^{+32}_{-22}	310.4^{+8}_{-12}	202.1^{+9}_{-9}	60.4
Data	782	321	196	62

H_T Bin (GeV)	575–675	675–775	775–875	875– ∞
W + $t\bar{t}$ background	10.6	3.1	0.6	0.6
Z $\rightarrow \nu\bar{\nu}$ background	8.7	4.3	2.5	2.2
QCD background	1.0	0.2	0.1	0.0
Total Background	20.3	7.7	3.2	2.9
Data	21	6	3	1

Table 6.17: Fit results for 1.1fb^{-1} with data observations. Since the QCD fit parameters are compatible with zero (see text), the listed QCD contributions in this table are also compatible with zero.

6.14 Excluding Signal Models

6.14.1 Constructing a Test Statistic

Using the full likelihood with the signal contribution as detailed previously and maximising gives the likelihood $L(\hat{f}, \hat{\theta})$ where \hat{f} is the MLE of f the parameter

of primary interest, and $\hat{\theta}$ the set of MLEs of all the nuisance parameters. The maximum likelihood for a given f $L(f, \theta_\mu)$ is defined by the conditional set of MLEs for the nuisance parameters, and the ratio between these two is known as the profile likelihood ratio $\lambda(f)$:

$$\lambda(f) = \frac{L(f, \theta_\mu)}{L(\hat{f}, \hat{\theta})} \quad (6.23)$$

The parameter f represents a factor applied to the nominal cross section of a signal model, such that when it values unity no correction is made. In order to set a limit a test statistic is defined q_f .

$$q_f = \begin{cases} -2\log\lambda(f) & \text{when } f > \hat{f} \\ 0 & \text{otherwise} \end{cases} \quad (6.24)$$

6.14.2 The CL_S Method

The CL_S method defines the probability of agreement with the S+B hypothesis relative to the background-only scenario:

$$CL_S = \frac{CL_{S+B}}{CL_B} \quad (6.25)$$

where CL_{S+B} is the probability of the observation agreeing with the signal plus background hypothesis, and CL_B the probability of agreement with the background only hypothesis. This is superior to methods that only require comparison to the signal plus background hypothesis, as

Implementation with our test statistic q_f requires the generation of pseudo-experiments in f in order to generate two distributions of q_f in both the S+B and B cases. The numerical value for $CL_{S+B}(CL_B)$ is 1 minus the quantile of the observed value in the S+B (B) q_f distribution. The value of $CL_S = \alpha'$. The level of confidence of excluding the signal model is then $1-\alpha'$. We choose to exclude at the 95% confidence level, corresponding to an $\alpha' = 0.05$. Thus all signal models for which $CL_S \leq 0.05$ are excluded.

6.14.3 Setting an Exclusion Limit in the CMSSM Plane

In order to interpret the results in the CMSSM model, this method is applied to signal events from many mSUGRA parameter sets in order to set an exclusion limit. We choose to fix three parameters $A_0 = 0$ GeV, $\tan \beta$ and $\text{sign}(\mu) = +$. A signal scan is produced in the plane of $m_0 - m_{1/2}$ with a set of 10k signal events generated at each point. SoftSUSY is used to generate the full mass spectrum of the sparticles, passed to Pythia for generation. After full reconstruction simulation they are reweighed according to the next-to-leading-order (NLO) cross-sections found by Prospino.

The CL_S method detailed above is applied to each point in the Signal Scan and tested against the 0.05 requirement in order to identify the 95% confidence exclusion limit, shown in Figure 6.12. Models beneath the curve are excluded at 95%. The expected limit band is shown centred on the median value with a ± 1 Standard Deviation width, taken from the relevant quantiles of the distribution of CL_S calculated using the full distribution of SM pseudo-experiments.

The points excluded translate within the CMSSM to a bound on the masses of the sparticles as they are governed by the parameters m_0 and $m_{1/2}$. Mean squark masses and equal gluino masses below 1.1 TeV can be excluded for $m_0 < 500$ GeV, and for higher values of m_0 with the gluino mass much lower than the mean squark mass, the gluino mass is excluded below 0.5 GeV.

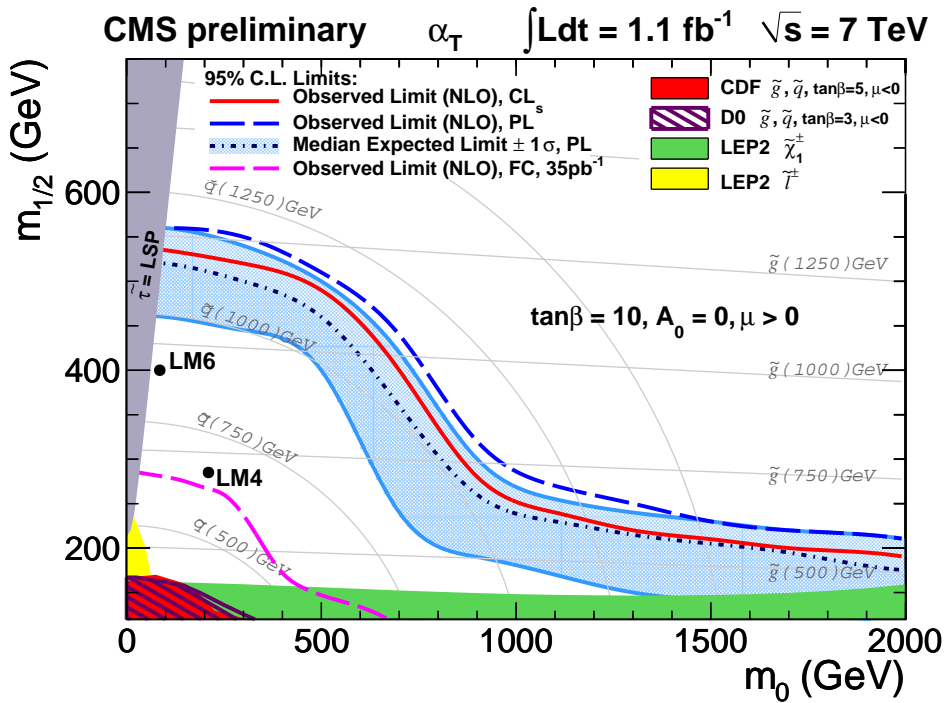


Figure 6.12: Observed and expected 95% CL exclusion contours in the CMSSM ($m_0, m_{1/2}$) plane ($\tan\beta = 10, A_0 = 0, \mu > 0$) using NLO signal cross sections using the Profile Likelihood (PL) method. The expected limit is shown with its 68% CL range. The observed limit using the CL_s method is shown as well.

Chapter 7

Conclusions

Appendix A

HT 1.1fb^{-1} Data

```
/HT/Run2011A-May10ReReco-v1/AOD  
/HT/Run2011A-PromptReco-v4/AOD
```

Photon 1.1fb^{-1} Data

```
/Photon/Run2011A-May10ReReco-v1/AOD  
/Photon/Run2011A-PromptReco-v4/AOD
```

Standard Model Background Monte Carlo

```
/QCD_Pt_*)_TuneZ2_7TeV_pythia6/Spring11-PU_S1_START311_V1G1-v1/AODSIM  
/QCD_TuneD6T_HT-*)_7TeV-madgraph/Spring11-PU_S1_START311_V1G1-v1/AODSIM  
/TTJets_TuneZ2_7TeV-madgraph-tauola/Summer11-PU_S4_START42_V11-v1/AODSIM  
/TToBLNu_TuneZ2_*)-channel_7TeV-madgraph/Spring11-PU_S1_START311_V1G1-v1/AODSIM  
  
/WJetsToLNu_TuneZ2_7TeV-madgraph-tauola/Summer11-PU_S4_START42_V11-v1/AODSIM  
  
/ZinvisibleJets_7TeV-madgraph/Spring11-PU_S1_START311_V1G1-v1/GEN-SIM-RECO  
  
/GJets_TuneD6T_HT-40To100_7TeV-madgraph/Spring11-PU_S1_START311_V1G1-v1/AODSIM
```

SUSY Signal Reference Monte Carlo

```
/LM4_SUSY_sftsh_7TeV-pythia6/Spring11-PU_S1_START311_V1G1-v1/AODSIM  
/LM6_SUSY_sftsh_7TeV-pythia6/Spring11-PU_S1_START311_V1G1-v1/AODSIM
```

Bibliography

- [1] William B Rolnick. “The Fundamnetal Particles and Their Interactions”. Addison-Wesley (1994).
- [2] R. Bouchendira, P. Cladé, S. Guellati-Khélifa, F. Nez & F. Biraben. “New Determination of the Fine Structure Constant and Test of the Quantum Electrodynamics”. *Physical Review Letters*, **106**, 8 (2011) 080801, 1012.3627.
- [3] Antonio Pich. “The Standard model of electroweak interactions”. 0705.4264.
- [4] M. Herrero. “The Standard model”. hep-ph/9812242.
- [5] S. L. Glashow. “Partial Symmetries of Weak Interactions”. *Nucl. Phys.*, **22** (1961) 579–588.
- [6] Jeffrey Goldstone, Abdus Salam & Steven Weinberg. “Broken Symmetries”. *Phys. Rev.*, **127** (1962) 965–970.
- [7] Luis Alvarez-Gaume & John Ellis. “Eyes on a prize particle”. *Nat Phys*, **7**, 1 (2011) 2–3.
- [8] Michael Peskin & Daniel Schroeder. “An Introduction to Quantum Field Theory”. Westview Press (1995).
- [9] Benjamin W. Lee, C. Quigg & H. B. Thacker. “Weak interactions at very high energies: The role of the Higgs-boson mass”. *Phys. Rev. D*, **16** (1977) 1519–1531.
- [10] Manuel Drees. “An Introduction to supersymmetry”. hep-ph/9611409.
- [11] F. Zwicky. “Die Rotverschiebung von extragalaktischen Nebeln”. *Helvetica Physica Acta*, **6** (1933) 110–127.
- [12] E. Komatsu et al. “Five-Year Wilkinson Microwave Anisotropy Probe (WMAP) Observations:Cosmological Interpretation”. *Astrophys. J. Suppl.*, **180** (2009) 330–376, 0803.0547.
- [13] Michael Dine. “Supersymmetry and String Theory”. Cambridge University Press (2007).

- [14] Michael E. Peskin. “Beyond the standard model”. hep-ph/9705479.
- [15] John Terning. “Modern Supersymmetry”. Clarendon Press (2006).
- [16] Stephen P. Martin. “A Supersymmetry primer”. hep-ph/9709356.
- [17] S. Dawson. “SUSY and such”. *NATO Adv. Study Inst. Ser. B Phys.*, **365** (1997) 33–80, hep-ph/9612229.
- [18] Albert de Roeck. “Early physics with ATLAS and CMS”. *Pramana Journal of Physics*.
- [19] A de Roeck, A Ball, M Della Negra, L Foa & A Petrilli. “CMS Physics: Technical Design Report Volume II, Physics Performance”. CERN, Geneva (2006). Revised version submitted on 2006-09-22 17:44:47.
- [20] Oliver Sim Brning, Paul Collier, P Lebrun, Stephen Myers, Ranko Ostojic, John Poole & Paul Proudlock. “LHC Design Report”. CERN, Geneva (2004).
- [21] Thomas Sven Pettersson & P Lefvre. “The Large Hadron Collider: Conceptual Design”. Technical Report CERN-AC-95-05 LHC, CERN, Geneva (1995).
- [22] The CMS Collaboration. “The Compact Muon Solenoid Technical Proposal”. *CERN/LHCC*, **94-38**.
- [23] K et al. Nakamura. “Review of Particle Physics, 2010-2011. Review of Particle Properties”. *J. Phys. G*, **37**, 7A (2010) 075021. The 2010 edition of Review of Particle Physics is published for the Particle Data Group by IOP Publishing as article number 075021 in volume 37 of Journal of Physics G: Nuclear and Particle Physics. This edition should be cited as: K Nakamura et al (Particle Data Group) 2010 *J. Phys. G: Nucl. Part. Phys.* **37** 075021.
- [24] The CMS Collaboration. “The CMS hadron calorimeter project: Technical Design Report”. Technical Design Report CMS. CERN, Geneva (1997).
- [25] Efe Yazgan. “The CMS barrel calorimeter response to particle beams from 2-GeV/c to 350-GeV/c”. *J. Phys. Conf. Ser.*, **160** (2009) 012056.
- [26] The CMS Collaboration. “The CMS muon project: Technical Design Report”. Technical Design Report CMS. CERN, Geneva (1997).
- [27] Sergio Cittolin, Attila Rcz & Paris Sphicas. “CMS trigger and data-acquisition project: Technical Design Report”. Technical Design Report CMS. CERN, Geneva (2002).

- [28] Wolfgang Adam, Boris Mangano, Thomas Speer & Teddy Todorov. “Track Reconstruction in the CMS tracker”. Technical Report CMS-NOTE-2006-041, CERN, Geneva (2006).
- [29] R Frhwirth. “Application of Kalman filtering to track and vertex fitting”. *Nucl. Instrum. Methods Phys. Res., A*, **262**, HEPHY-PUB-503 (1987) 444. 19 p.
- [30] R Frhwirth, Wolfgang Waltenberger & Pascal Vanlaer. “Adaptive Vertex Fitting”. Technical Report CMS-NOTE-2007-008, CERN, Geneva (2007).
- [31] The CMS Collaboration. “Tracking and Primary Vertex Results in First 7 TeV Collisions”. **CMS-PAS-TRK-10-005**.
- [32] Xavier Janssen for the CMS Collaboration. “Underlying event and jet reconstruction in CMS”. **CMS CR-2011/012**.
- [33] Matteo Cacciari, Gavin Salam & Gregory Soyez. “The anti- k_t jet clustering algorithm”. *JHEP*, **0804** (2008) 063.
- [34] V Chetluru, F Pandolfi, P Schieferdecker & M Zelinski. “Jet Reconstruction Performance at CMS”. **CMS AN-2009/067**.
- [35] S. Catani, Yuri L. Dokshitzer, M. H. Seymour & B. R. Webber. “Longitudinally invariant K(t) clustering algorithms for hadron hadron collisions”. *Nucl. Phys.*, **B406** (1993) 187–224.
- [36] G. Corcella, I.G. Knowles, G. Marchesini, S. Moretti, K. Odagiri et al. “HERWIG 6.5 release note”. hep-ph/0210213.
- [37] Torbjorn Sjostrand, Stephen Mrenna & Peter Z. Skands. “PYTHIA 6.4 Physics and Manual”. *JHEP*, **0605** (2006) 026, hep-ph/0603175.
- [38] The Geant4 Collaboration. “Geant4-A Simulation Toolkit”. *Nuclear Instruments and Methods in Physics Research A*, **506** (2003) 250–303.
- [39] The CMS Collaboration. “Jet Energy Corrections determination at 7 TeV”. **CMS-PAS-JME-10-010**.
- [40] S Esen, G Landsberg, M Titov, A DeRoeck, M Spiropolu, M Tytgat, D Puigh, P Wittich, K Terashi, A Gurrola, T Kamon, C. N. Nguyen, A Safonov, J. W. Gary, F Liu, H Nguyen, J Sturdy, R Cavannaugh, R Remington, M Schmitt, B Scurlock, E.A. Albayrak, T Yetkin & M Zielinski. “ \cancel{E}_T Performance in CMS”. **CMS AN-2007/041**.
- [41] Greg Landsberg & Filip Moortgat. “MET Reconstruction, Performance, and Validation”. **CMS AN-2008/089**.

- [42] The CMS Collaboration. “Missing Transverse Energy Performance in Minimum-Bias and Jet Events from Proton-Proton Collisions at $\sqrt{s} = 7$ TeV”. **CMS-PAS-JME-10-004**.
- [43] The CMS Collaboration. “Performance of CMS Muon Reconstruction in Cosmic-Ray Events”. *J. Instrum.*, **5**, arXiv:0911.4994. CMS-CFT-09-014 (2009) T03022 . 47 p.
- [44] The CMS Collaboration. “Performance of muon reconstruction and identification in pp collisions at $\sqrt{s} = 7$ TeV”. **CMS-PAS-MUO-10-004**.
- [45] The CMS Collaboration. “Photon reconstruction and identification at $\sqrt{s} = 7$ TeV”. **CMS-PAS-EGM-10-005**.
- [46] Wolfgang Adam, R Frhwirth, Are Strandlie & T Todor. “Reconstruction of Electrons with the Gaussian-Sum Filter in the CMS Tracker at the LHC”. Technical Report CMS-NOTE-2005-001, CERN, Geneva (2005).
- [47] The CMS Collaboration. “Electron reconstruction and identification at $\sqrt{s} = 7$ TeV”. **CMS-PAS-EGM-10-004**.
- [48] Lisa Randall & David Tucker-Smith. “Dijet Searches for Supersymmetry at the LHC”. *Phys. Rev. Lett.*, **101** (2008) 221803, 0806.1049.
- [49] The CMS Collaboration. “SUSY searches with dijet events”. **CMS PAS SUS-08-005**.
- [50] Henning Flaecher, John Jones, Tanja Rommerskirchen, Benjamin Sinclair & Markus Stoye. “SUSY searches with dijet events”. **CMS AN-2008/071**.
- [51] T Whyntie, O Buchmuller, O Flacher, J Jones, T Rommerskirchen, M Stoye & A Tapper. “Extending the early SUSY search with all-hadronic dijet events to n-jet topologies”. **CMS AN-2008/114**.
- [52] H Flacher, M Stoye, T Rommerskirchen, R Bainbridge, J Marrouche, T Whyntie & T Yetkin. “Search for SUSY with exclusive n-jet events”. **CMS AN-2009/056**.
- [53] R Bainbridge, B Betchart, H Flacher, E Laird, B Mathias, T Rommerskirchen & M Stoye. “Performance of variables used in jets + missing energy searches in 7 TeV data”. **CMS AN-2009/056**.
- [54] O Buchmuller, L Gouskos, Z Hatherell, G Karapostoli, A Sparrow & P Sphicas. “An application of the α_T jet-balancing method to the single-lepton mode SUSY searches”. **CMS AN-2009/188**.

- [55] Vardan Khachatryan et al. “Search for Supersymmetry in pp Collisions at 7 TeV in Events with Jets and Missing Transverse Energy”. *Phys.Lett.*, **B698** (2011) 196–218, 1101.1628.
- [56] The CMS Collaboration. “Absolute Calibration of Luminosity Measurement at CMS: Summer 2011 Update”. **CMS PAS EWK-11-001**.
- [57] The CMS Collaboration. “Calorimeter Jet Quality Criteria for the First CMS Collision Data”. **CMS-PAS-JME-09-008**.
- [58] The CMS Collaboration. “Performance of muon identification in pp collisions at $\sqrt{s} = 7$ TeV”. **CMS-PAS-MUO-10-002**.
- [59] N. Adam et al. “Measurements of Inclusive W and Z Cross Sections in pp Collisions at $\sqrt{s} = 7$ TeV”. **CMS AN 2010/116**.
- [60] The CMS Collaboration. “Isolated Photon Reconstruction and Identification at $\sqrt{s} = 7$ TeV”. **CMS-PAS-EGM-10-006**.
- [61] The CMS Collaboration. “Measurement of the W and Z inclusive production cross sections at $\sqrt{s}=7$ TeV with the CMS experiment at the LHC”. **CMS PAS EWK-10-002**.
- [62] Z. Bern, G. Diana, L.J. Dixon, F. Febres Cordero, S. Hoche et al. “Driving Missing Data at Next-to-Leading Order”. *Phys.Rev.*, **D84** (2011) 114002, 1106.1423.
- [63] The CMS Collaboration. “Performance of Methods for Data-Driven Background Estimation in SUSY Searches”. **CMS PAS SUS-10-001**.
- [64] Johan Alwall, Pavel Demin, Simon de Visscher, Rikkert Frederix, Michel Herquet et al. “MadGraph/MadEvent v4: The New Web Generation”. *JHEP*, **0709** (2007) 028, 0706.2334.
- [65] F. James & M. Roos. “Minuit - a system for function minimization and analysis of the parameter errors and correlations”. *Computer Physics Communications*, **10** (1975) 343–367.